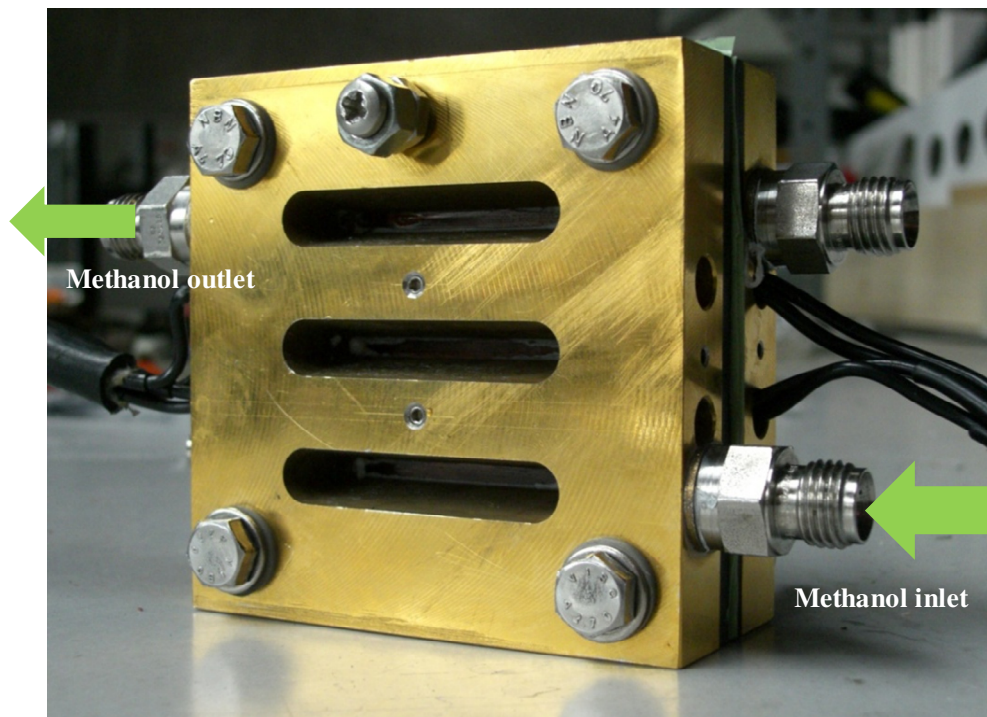

Spatially resolved studies in direct methanol fuel cells

A dissertation submitted to the Institute of Materials Science, Technische Universität Darmstadt, for the degree of **Doctor of Science** Dr. rer. nat. submitted by M.Sc Ditty Dixon, Kerala, India
May 2012-Darmstadt- D 17



TECHNISCHE
UNIVERSITÄT
DARMSTADT

Materialwissenschaft
Erneuerbare Energien



Spatially resolved studies in direct methanol fuel cells

MatNr-1349773

Kerala, India, Ditty Dixon

19.09.1983

Date of submission 25.11.2011

Date of oral exam 9.05.2012

Berichter: Prof. Christina Roth

Mitberichter: Prof. Ralf Riedel

Prüfer (FB 11): Prof. Wolfgang Ensinger

Prüfer (extern): Prof. Peter Claus

Technische Universität Darmstadt

Materialwissenschaft

Erneuerbare Energien

Prof. Christina Roth



Abstract

Diese Doktorarbeit konzentriert sich vor allem auf die dreidimensional aufgelöste Charakterisierung von Direktmethanol-Brennstoffzellen. Zunächst wurden räumlich aufgelöste Analysen am Ende der Lebensdauer von Stapel-Membranelektrodenanordnung mit Hilfe von verschiedenen Techniken, wie zum Beispiel Röntgenbeugung (XRD), Transmissionselektronenmikroskopie (TEM), energiedispersive Röntgenmapping (EDX) und Röntgen-Absorptions-Spektroskopie (XAS) durchgeführt. Der Verbleib des Rutheniums in der Direktmethanol-Brennstoffzelle (DMFC) während der Alterung wurde in diesen Studien sorgfältig analysiert. Es wurde herausgefunden, dass die große, oxidierte Rutheniumfraktion im anodischen Katalysator, einen entscheidende Einfluss bei dem Partikelwachstum und der Rutheniumauflösung hat. Desweiteren wurde Ruthenium auch in Form von Ablagerung, vorzugsweise an den Methanolaustrittsbereichen, in der Nafionmembran gefunden. Ex-situ Studien gingen dreidimensional aufgelöste in-situ XAS-Studien voran. Dafür wurden in-situ Zellen für raum aufgelöste DMFC-Studien entwickelt und optimiert. Der relative OH- und CO-Bedeckungsgrad der Anode und Kathode wurde mit Hilfe von $\Delta\mu$ XANES Techniken, in unterschiedlichen Regionen der DMFC während des Betriebs, bei verschiedenen elektrischen Strömen, in Abhängigkeit vom Sauerstoff-Fluss verfolgt. Zum ersten Mal wurde ein sehr starker „cross-talk“ zwischen Anode und Kathode beobachtet, wobei die Anode bei hohen O_2 -Flussraten die OH-Bedeckung der Kathode bestimmt. Die Studien zur Brennstoffverknappung bei der einzelnen DMFC-Zelle offenbarten ein uneinheitliches Degradierungsmuster mit einer hohen Degradierung am Methanoleinlass und einer geringen Degradierung am Methanolauslass.

Schließlich wurden formspezifische Pt-Nanopartikel, unter Verwendung verschiedener Tenside wie Tetradecyltrimethylammonium Bromid (TTAB) und Polyvinylpyrrolidon (PVP) synthetisiert und auf ihre Leistung in der Brennstoffzelle getestet. Diese formspezifischen Pt-Nanopartikel wurden mittels TEM charakterisiert und die elektrokatalytische Aktivität mittels cyclischer Voltammetrie getestet. Hoch-Potential-Cyclen der formspezifischen Partikel offenbarte eine bevorzugte Degradierung von Pt (100) Flächen gegenüber Pt (110). Die TEM Analyse der cyclischen Proben zeigte in erster Linie formspezifische Partikel mit sehr wenigen kugelförmigen Partikeln. Schließlich zeigten getragene formspezifische Partikel exzellente Kraftstoff-Performance, selbst mit nur geringer Pt-Beladung. Durch Anpassen der Form der

Pt-Nanopartikel kann voraussichtlich die Pt-Kapazität noch gesteigert werden, wodurch die Pt-Bedeckung in der MEA reduziert werden kann. Desweiteren wird eine höhere Haltbarkeit für die formspezifischen Partikel im Vergleich zu kommerziellen Katalysatoren erwartet. Demzufolge kann durch Anpassung der Form der Pt-Nanopartikel eine Kostensenkung und eine erhöhte Haltbarkeit erreicht werden.

Abstract

The thesis mainly focuses on the spatially resolved characterization of a direct methanol fuel cell. Initially spatially resolved analyses were carried out on an end of life (5000 hrs operated) stack membrane electrode assembly (MEA) using various techniques, like X-ray diffraction (XRD), transmission electron microscope (TEM), energy dispersive X-ray (EDX) mapping and X-ray absorption spectroscopy (XAS). The fate of the Ru in the direct methanol fuel cell (DMFC) with ageing is carefully analyzed in these studies. It was found that the large oxidized ruthenium fraction in the anode catalyst plays a significant role in particle growth and ruthenium dissolution. Ru was also found in the form of precipitates in the Nafion membrane preferentially at the methanol outlet regions. *Ex-situ* studies were preceded by *in-situ* spatially resolved XAS studies. For these, *in-situ* cells for spatially resolved DMFC studies are developed and optimized. The relative OH and CO coverages on both the anode and cathode were followed using the $\Delta\mu$ XANES technique at different regions of a DMFC during operation at several current levels in dependence on the oxygen flow. For the first time, a very strong “cross-talk” between the anode and cathode is seen with the anode dictating at high O₂ flow rate the OH coverage on the cathode. The fuel starvation studies on the single DMFC cell revealed a non-uniform degradation pattern with a high degradation at the methanol inlet and low degradation at methanol outlet.

Finally, shape-selected Pt nanoparticles were synthesized using different surfactants like tetradecyltrimethylammonium bromide (TTAB) and polyvinylpyrrolidone (PVP) and tested fuel cell performance. These shape-selected Pt nanoparticles were characterized by TEM and their electrocatalytical activity tested by cyclic voltammetry. High potential cycling of the shape-selected particles revealed a preferential degradation of Pt (100) facets over Pt (110). The TEM analysis of the cycled samples showed predominantly shape-selected particles with very few spherical particles. Finally, supported shape-selected particles showed excellent fuel performance even with low Pt loading. Tuning of the shape of Pt nanoparticles is expected to increase the Pt utilization, i.e. Pt loading can be reduced in the MEA. Further higher durability is expected for the shape-selected particles than the commercial catalyst. Thus by tuning the shape of the Pt nanoparticles, cost reduction and increased durability can be achieved.

Declaration

I hereby declare that I have made this thesis independently and with the stated and permitted aids.

I have not given any doctoral exam so far.

Darmstadt, 25.11.2011

M.Sc. Chem. Ditty Dixon

Contents

Abstract	iv
1 Motivation	1
2 Basic concepts	3
2.1 Introduction to direct methanol fuel cells	3
2.1.1 The membrane electrode assembly (MEA)	4
2.2 Water management in fuel cells.....	6
2.3 Methanol oxidation and significance of Pt/Ru catalyst.....	7
2.3.1 The ligand and bi-functional mechanism in MOR.....	8
2.4 Challenges in DMFC technology	11
2.4.1 Degradation of catalyst and Ru dissolution.....	12
2.4.2 Mitigation strategies for catalyst and support degradation.....	15
2.4.3 Shape selected Pt nanoparticles for better activity and durability.....	16
2.4.4 Methanol cross over.....	17
2.4.5 Methanol cross over and bi-functional operation	19
2.5 Non uniform distribution of current density and spatially resolved <i>in-situ</i> studies	20
3 XAS and <i>in-situ</i> investigation of fuel cells	24
3.1 Theory of XAS.....	24
3.1.1 XAS data processing.....	26
3.1.2 Data analysis of XANES.....	26
3.1.3 Data analysis of EXAFS	29
3.2 <i>In-situ</i> investigation of fuel cell reaction by XAS.....	31
4 Development of an <i>in-situ</i> XAS fuel cell for spatially resolved studies	33
4.1 Experimental	33
4.1.1 Modified fuel cell for spatially resolved XAS studies.....	33
4.1.2 Fabrication of MEA and fuel cell performance test.....	34
4.1.3 <i>In-situ</i> spatially resolved XAS test	34
4.2 Results and discussion.....	35

5	Spatially resolved <i>ex-situ</i> studies on aged DMFC MEA	41
5.1	Experimental.....	41
5.1.1	Fabrication of MEA and fuel cell stack operation.....	41
5.1.2	X-ray diffraction (XRD)	42
5.1.3	Transmission electron microscopy (TEM).....	42
5.1.4	Scanning electron microscopy (SEM) and energy dispersive X-ray (EDX) mapping	43
5.1.5	X-ray absorption spectroscopy (XAS)	43
5.2	Results and discussion.....	43
6	Spatially resolved, in operando XAS studies in a DMFC	61
6.1	Experimental.....	61
6.1.1	$\Delta\mu$ -XANES technique	62
6.1.2	EXAFS analysis.....	63
6.2	Results and discussion	64
6.2.1	High O ₂ flow results (Anode).....	65
6.2.2	High O ₂ flow results (Cathode).....	69
6.2.3	Low O ₂ flow results	70
6.2.4	Fuel starvation results.....	75
7	Shape-selected Pt nanoparticles as fuel cell catalyst	81
7.1	Experimental.....	81
7.1.1	Synthesis of shape-selected nanoparticles using TTAB.....	81
7.1.2	Synthesis of shape-selected nanoparticles using PVP.....	81
7.1.3	Electrochemical studies: Cyclic voltammetry (CV).....	82
7.1.4	MEA fabrication and fuel cell test	82
7.2	Results and discussion.....	82
8	Summary and Outlook	95
8.1	Summary.....	95
8.2	Outlook.....	97
	Bibliography	99
	List of Figures	110
	List of Tables	114

Acknowledgement	115
Curriculum Vitae	117
Publications and Patents	119

Nomenclature

Abbreviations

ATO	Antimony tin oxide
BF	Bi-functional mechanism
CNT	Carbon nano tubes
CV	Cyclic voltammetry
DA	Dissociative adsorption
DFT	Density functional theory
DMFC	Direct methanol fuel cell
DW	Debye Waller factor
EDX	Energy Dispersive X-ray spectroscopy
EDXAS	Energy dispersive X-ray absorption spectroscopy
EOL	End of life
EOR	Ethanol oxidation reaction
ESA	Electrochemically active surface area
EXAFS	Extended X-ray absorption fine structure
FT	Fourier transform
FWHM	Full width half maxima
GDL	Gas diffusion layer
HOMO	Highest occupied molecular orbital
HOR	Hydrogen oxidation reaction
IR	Infra red spectroscopy
LUMO	Lowest unoccupied molecular orbital
MEA	Membrane electrode assembly
MOR	Methanol oxidation reaction
MPL	Micro porous layer
NMR	Nuclear magnetic resonance
OCV	Open circuit voltage
ORR	Oxygen reduction reaction
PCB	Printed circuit board
PEMFC	Polymer electrolyte membrane fuel cell
PIPS	Passivated ion implanted planar silicon
PVDF	Polyvinylidenfluorid
PVP	Polyvinylpyrrolidone
QEXAFS	Quick X-ray absorption spectroscopy
RA	Reductive Adsorption
RD	Reductive desorption
RHE	Reversible hydrogen electrode
RT	Reductive transition

SEM	Scanning electron microscope
SPEEK	Sulfonated-polyetheretherketone
TEM	Transmission electron microscopy
TG	Thermo gravimetry
TTAB	Tetradecyltrimethylammonium bromide
UHV	Ultra high vacuum
XANES	X-ray absorption near edge structure
XAS	X-ray absorption spectroscopy
XPS	X-rax photoelectron spectroscopy
XRD	X-ray diffraction

Symbol index

E^0	Potential vs RHE
η_f	Efficiency
I	Current
I_{tot}	Total current
I	Transmitted intensity
I_0	Incoming intensity
x	Sample thickness
μ	absorption coefficient
E	Energy
$X(k)$	EXAFS function
S_0^2	Amplitude reduction factor
R	Bond distance
σ	Debye Waller factor
N	Coordination number
E_0	Threshold energy
μ_0	background function
λ	Wave length
θ	diffraction angle
M	Moles



1 Motivation

Polymer electrolyte membrane fuel cells (PEMFC) are one of the most promising renewable energy technologies having the potential of creating an electro mobility world. Applications of PEMFC were also realized in stationary and portable devices depending on the power they deliver. The Direct methanol fuel cell (DMFC) is one such candidate which was successfully tested for operating in many portable and stationary applications. Although the power output of the DMFC systems is much lower compared to a direct hydrogen fuel cell, the absence of a complex humidifying system or water management system makes DMFC attractive in household and remote operating systems. Apart from the desired power output, the long term durability of the system is highly demanding for any of the mentioned applications. Current generations of the DMFC are often associated with issues like fuel crossover, Ru crossover, catalyst and support degradation in the form of corrosion, aggregation and particle growth. At present, cost of DMFCs is much higher than the PEMFCs due to higher Pt loading. However, Pt utilization in DMFCs is quite low and in reality only 25-40 % of the total Pt is active in fuel cell reaction [1].

DMFC are often associated with a non uniform distribution of temperature, catalyst, reactant and product (flooding or blocking) which ultimately can lead to local fluctuations in current distribution and an accelerated ageing of the affected area [2] [3]. This situation strongly points towards the need of developing spatially resolved investigation techniques for fuel cells. Many analytical techniques like X-ray diffraction (XRD), transmission electron microscopy (TEM) and X-ray photoelectron spectroscopy (XPS) were successfully used for spatially resolved information. Usually the information from these techniques is limited by the nature of the sample, as measurements usually involve an end of life sample (EOL). X-ray absorption spectroscopy (XAS) is one such technique which can non-destructively probe the structure and chemical environment of the fuel cell catalyst under real fuel cell conditions. Further spatially resolved studies can provide detailed knowledge on how working conditions in real fuel cell affect catalyst. The spatially resolved results are essential for optimizing the operating parameters such as temperature, working voltage, methanol and oxygen flow rate which are crucial factors in determining durability and performance of the DMFCs.

Finally, durability and activity of the fuel cell catalyst greatly depends on the catalyst's shape. For example a Pt (111) facet shows higher activity for CO oxidation or methanol oxidation than Pt (100) or Pt (110) [4]. Similarly, an octahedral Pt-Pd catalyst, predominantly with (111) facets, shows greater stability and activity for the methanol oxidation reaction [5]. Hence, by controlling the shape of the catalyst one can increase the activity and durability of the catalyst. Shape of the nanoparticles can be carefully controlled by the addition of a surfactant which selectively adsorbs to the metal surfaces.

2 Basic concepts

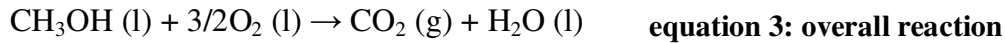
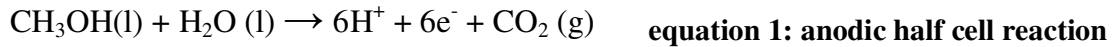
2.1 Introduction to direct methanol fuel cells

Fuel cells can convert chemically stored energy of a substance to electrical energy, a principle first proposed by German scientist Christian Friedrich Schönbein in 1838. Later, fuel cell technology was first demonstrated by Sir William Grove in 1839 and the term “fuel cell” was first used by William White Jacques. Currently, fuel cells are classified according to the operational temperature or the electrolyte which they use. The DMFC belongs to the low temperature fuel cell category, which uses a polymer membrane as the electrolyte [6].

As the name indicates a direct methanol fuel cell is operated by feeding liquid methanol to the system. Methanol in liquid state is highly favorable compared to gaseous hydrogen as the latter always has the hazard of explosion. Further a DMFC can often run without the need of any complex humidifying systems, whereas direct hydrogen fuel cell’s performance always depends on the humidification level of hydrogen and the membrane.

The principle of the DMFC involves the electrocatalytic oxidation of methanol in the anodic compartment and reduction of an oxidant such as O_2 in the cathodic compartment. Both the anodic and cathodic compartments are isolated from each other by a proton conducting membrane which facilitates only the passage of H^+ ions produced during the oxidation of the fuel. The whole electrocatalytic reactions take place in the membrane electrode assembly (MEA), the so called heart of the fuel cell, which is made up of the catalyst, catalyst support, proton conducting membrane and the gas diffusion layer (GDLs). The electrons produced during the oxidation process are forced to flow through an external circuit and finally reach the cathode, where they combine with H^+ and O_2 to form water. Thus the fuel cell is a wonderful example of an interdisciplinary system, which combines scientific knowledge from the field of catalysis, electrochemistry, nanotechnology, polymer science etc.

The different steps during the methanol oxidation (MOR) reaction in a DMFC are represented by equation 1 & 2, and the overall reaction by equation 3.



2.1.1 The membrane electrode assembly (MEA)

The sketch of the membrane electrode assembly is shown in Figure 1.

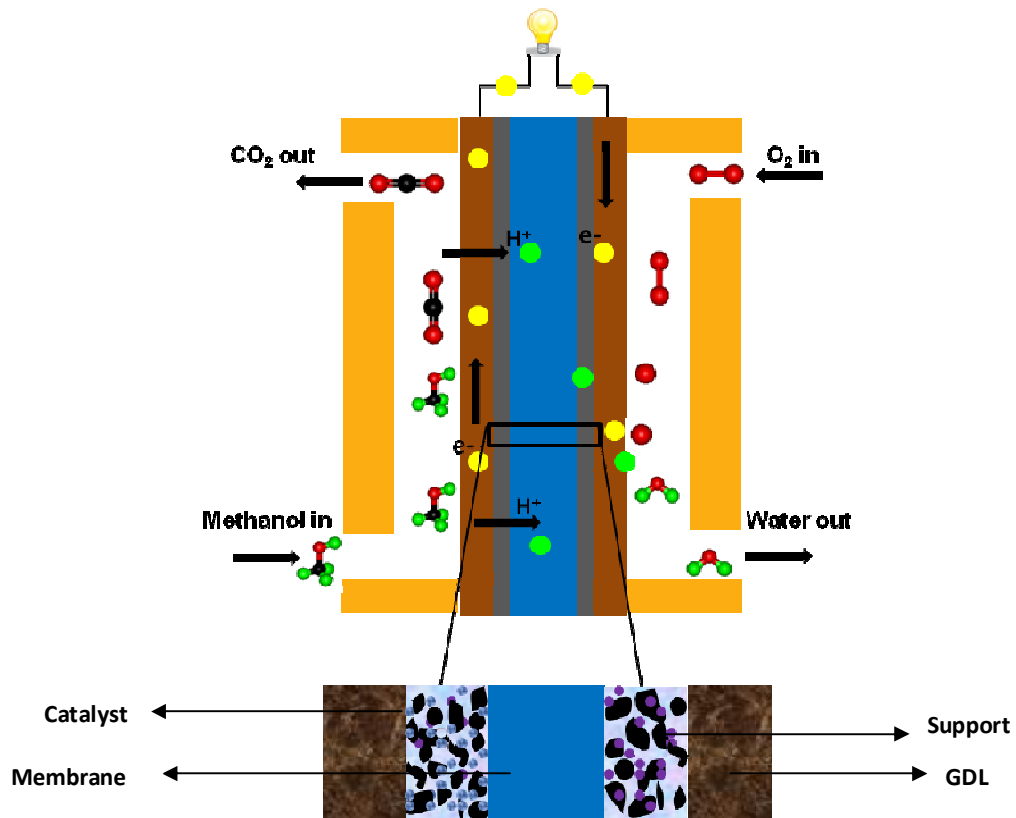


Figure 1: Schematic representation of DMFC, the MEA region is enlarged below

A typical MEA of the DMFC consists of two catalyst layers (electrodes) sandwiched between a polymer electrolyte membrane, usually Nafion. In a standard MEA fabrication process, a viscous ink of the catalyst-support material is prepared by ultrasonic dispersion in a water/isopropanol/nafion mixture. The above prepared ink is either deposited onto a GDL or Nafion membrane depending on the coating technique employed e.g. spraying, screen printing or knife coating. Subsequently the GDL, catalyst layer and the membrane are hot pressed to

obtain the MEA. Different components of the MEA and their properties and functions are summarized in Table 1.

<i>Components</i>	<i>Function</i>	<i>Properties</i>	<i>Material used</i>
Catalyst	Facilitate MOR and Oxygen reduction reaction (ORR)	High surface area, physically and chemically stable in fuel cell conditions	Pt, Pt/Ru, RuSe, PtCo, Pd etc.
Support	Prevents catalyst sintering, facilitates reactant and electron transport	Porous, large surface area, electrically conductive, stable in fuel cell conditions.	High surface area carbon, carbon nanotubes, ATO etc.
Gas diffusion layer	Uniformly distributes the gaseous and liquid reactants, water management, provides electron path to the external circuit.	High electrical conductivity, pores for gas transport.	Teflon treated carbon paper and woven cloth
Membrane	Conducts protons, separates the anode and cathode reactant from mixing	High proton conductivity, non-permeable to the reactants.	Nafion

Table 1: Fuel cell components and functions

It is extremely important to make the right choice of the catalyst for DMFC reaction, as the catalyst's chemical nature [7], particle size [8] and loading can influence fuel cell performance. In the context of MOR the Pt/Ru catalyst has got the most attention, as no other catalyst was found as effective as Pt/Ru. MOR on the Pt/Ru surface will be discussed in detail in section 2.3. For the ORR, Pt alloys (Pt/M; M=Co, V, Cr etc) look attractive due to their high ORR activity compared to pure Pt [9]. However, severe degradation was observed for these systems under long term operation, especially in automotive conditions [10]. Moreover, DMFC's often suffer from methanol crossover where at the cathode crossover methanol competes for Pt sites along with oxygen, ultimately leading to the loss of cell voltage [11]. Therefore, high Pt loadings are usually preferred on the cathode side to compensate for these losses; hence pure Pt catalyst is preferred over an alloy catalyst as cathode in DMFCs. Many works were also

done in the direction of developing methanol tolerant catalyst like e.g. RuSe_x, however they are often associated with low ORR activity and higher degradation [12]. Probably a smart way to tackle the problem of cathodic losses due to methanol crossover could be developing methanol impermeable membranes [13]. Yet another strategy often employed to reduce the methanol crossover is to use a thicker membrane [14]. Methanol crossover will be discussed briefly in section 2.4.4.

Finally, the GDLs in the fuel cells also play a decisive role in determining the performance of a fuel cell by providing good electrical contact with the end plates or function like a current collector. The GDLs are also fabricated in such a way that they distribute the reactant uniformly in the electrode and facilitate efficient water management. It is often seen that to enhance the mass diffusion, an additional micro porous layer (MPL) with pore sizes significantly smaller than that of the GDLs is applied on the GDL. The extent of hydrophobicity of the GDL or the MPL is also a decisive factor for better water management in DMFC. It is observed that a highly hydrophobic GDL in the cathode removes water faster in comparison to less hydrophobic GDL, and maintains uniform current distribution. In contrast it has been found that, the hydrophobicity of the GDL has no major influence on the water management on the anode side [15]. The MEAs are then stacked in series with the help of different accessories like bipolar plates and sealings to form a DMFC stack. The bipolar plates are etched with flow fields with different geometry which distribute the reactants uniformly in the MEA. Bipolar plates also provide mechanical stability and control the thermal management of the stack.

2.2 Water management in fuel cells

One of the key challenges for the development of low-temperature polymer electrolyte membrane fuel cells (PEMFC) is achieving effective water management. Inefficient water management not only decreases the fuel cell's performance but also leads to accelerated degradation of the fuel cell components. It is known that, optimal amount of water is required in the fuel cell for the proton conductivity. This is quite usual for the operation of H₂-PEM fuel cells, as the high gas flow dries out the fuel and ultimately the proton conductivity is lost. In order to avoid this problem, the fuel gas streams are often humidified, which needs an external humidifying setup. However an excess amount of water accumulating in the cell is also an issue as it can block the reactant flow and the fuel cell performance is degraded. This is mostly

an issue at the cathode of the fuel cell, where the product water accumulates and flooding can happen. There are several factors contributing to the water management in the fuel cell for e.g. fuel cell operating temperature, hydrophobicity and porosity of the GDL and MPL, gas flow rates, operating voltage, and flow field design etc.

Fuel cell operating temperature is a key issue for effective water management, as very high temperature can dry out the cell faster whereas sub freezing temperature can lead to the formation of ice in the fuel cell. The ice formation can lead to reduced gas transport and conductivity, moreover expansion in volume and associated stress during the ice formation can damage the electrode structure [16]. So an efficient thermal management is also quite important for an efficient water management. The significance of GDL and MPL wettability was mentioned in the previous section and in general, GDL with high volume of micropores and hydrophobic are found to show excellent water management [17]. Finally geometry of the flow fields also plays a major role in water management. It is often found that serpentine or meander flow field geometry facilitates the removal of water much more efficiently than parallel flow fields, where gas stagnation is often seen [18]. Further the aspect ratio of the channels was also found to influence the efficiency of water removal of serpentine flow fields, especially at high current densities [19].

2.3 Methanol oxidation and significance of Pt/Ru catalyst

The simplified methanol oxidation reaction is represented by equation 3, which involves 6 electrons and breaking of the CH bond and the formation of CO₂. The detailed methanol oxidation process is given in Figure 2.

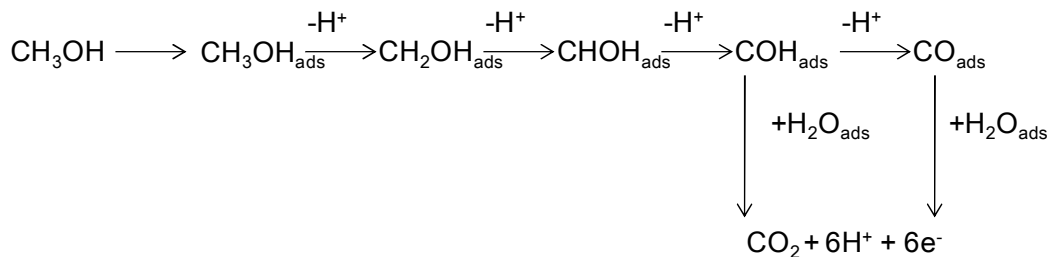


Figure 2: Summary of different steps in MOR

Although the thermodynamic standard potential of the above reaction is close to the equilibrium potential of hydrogen ($E^0 = 0.02 \text{ V}$), the reaction is several orders of magnitude slower than hydrogen oxidation. This is due to poisoning of the catalyst surface by intermediate products (CHO, HCOOH, CO) and several C-H bond cleavages involved, as shown in the reaction sequence [20] [21]. The catalytic activity or the poisoning of the Pt surface is intrinsically attributed to the d-band electronic configuration and the nature of the adsorbate [22]. Thus, state-of-art of the development of methanol oxidation catalyst involves 1) the perturbation of the d band configuration of Pt [23] or 2) the activation of water and oxidation of the adsorbate [24][25]. Both strategies can be usually achieved by the addition of a second metal (Sn, Ru, Ni, Os etc) to the platinum. It is often referred to as a ligand mechanism, if the second metal donates electrons to the Pt and weakens the metal adsorbate bond [26][27] or as a Bi-functional mechanism (BF), if the second metal activates water and oxidizes the adsorbate [24][28]. Ongoing debates exist on the exact mechanism of MOR by Pt/Ru catalysts as evidences supporting both mechanisms have been reported for the same catalyst system [29]. Nevertheless, immense researche until now has well established the Pt/Ru alloy catalyst as the best catalytic system for MOR. Both ligand and bi-functional mechanism of removal of adsorbed CO from Pt/Ru system will be discussed briefly in the sections below.

2.3.1 The ligand and bi-functional mechanism in MOR

CO ligands are known to form metal carbonyls (coordination complexes) with metal with their lower oxidation state. Apart from σ bond between unfilled metal orbital and HOMO of CO a back bonding between the metal filled d orbital and LUMO of the CO takes place. The bonding between the CO and platinum is schematically shown below.

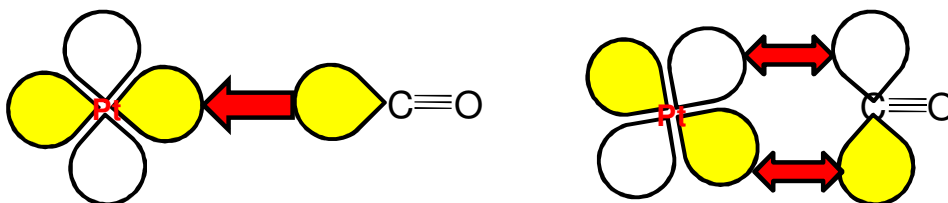
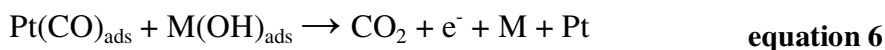
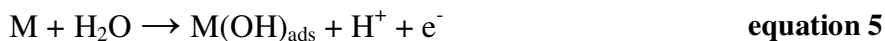


Figure 3: Schematic representation of bonding of CO with Pt

The π back bonding has a dramatic effect on the bond length (strength) of Pt-C. It is often seen that the bond length Pt-C of metal carbonyl is much lower (1.8 Å) than the Pt-C of other organometallic compounds (2.0 Å) [30]. This ultimately results in the weakening of the CO bond, which is supported by different spectroscopic techniques. For example, an *in-situ* IR spectroscopic study on the Pt/methanol system has shown a C-O stretching frequency around 1270 cm⁻¹ for a Pt/CO adsorbed system whereas the theoretical value is about 1370 cm⁻¹. This blue shift in the stretching frequency is due to the weakening of the C-O bond due to back bonding [31]. Thus, any weakening of the Pt-CO as in the case of MOR requires the electronic re-structuring of the Pt d band or activation of the platinum surface with OH.

The most discussed mechanism for MOR is the bi-functional mechanism (BF) developed by Watanabe and Motoo [24]. This mechanism involves synergistic activity of two metals, where Pt adsorbs and decomposes methanol, whereas the second metal Ru or Sn dissociates water to generate OH species, which oxidize the CO adsorbate from the Pt surface. The bifunctional mechanism is represented by the following equations;



Watanabe and Motoo predicted that for the enhanced electrocatalytic activity of Pt the ad-atom M should adsorb the oxygen at more negative potentials than Pt, for e.g. Ru or Sn. Moreover, from equation 6 it may be concluded that bond dissociation energy for Pt-CO and M-OH should be identical (~590 kJmol⁻¹). In fact, the bond dissociation energies for both Ru-OH and Sn-OH fall close to that for Pt-CO thus making them ideal candidates, which can be effectively coupled with Pt for MOR [32]. Electrochemical evidence supporting the BF mechanism was obtained from cyclic voltammetry, where it was found that the addition of Ru to Pt shifted the onset peak for methanol oxidation more negative at least by 200 mV (depending on the amount of Ru added) than for the pure Pt surface [33]. These results were further supported by *in-situ* IR spectroscopic studies by comparing the evolution of the C=O stretching bond for pure Pt and Pt/Ru system, where for the former C=O stretching frequency appeared at higher potential

(0.52 V) and for the latter with a weak signal at lower potential typically around 0.3 V [34] [35] [36]. The weak signal for C=O stretching for the alloy catalyst system was attributed to the higher rate of oxidation of methanol at the surface. Although, numerous similar approaches involving electrochemical spectroscopic studies strongly supported the bi-functional mechanism, an agreement on the optimum amount of Ru in the alloy for the best activity could not be reached until now. This discrepancy might be due to different type of Pt/Ru samples used in these studies and often Ru tends to segregate on the surface and what is predicted as bulk composition may differ. Nevertheless, with chronoamperometric measurements on different Pt/Ru alloy nanoparticles with varying composition of Ru, Rigsby *et al.* predicted 20-30% of Ru in the catalyst as the best composition for MOR [37]. Although these findings supported the BF mechanism of MOR, they did not completely exclude any contribution of the ligand effect associated with alloy nanoparticles. In fact, in 1992 Rodriguez proposed that in a nano alloy system an ad-atom (e.g. Ru) greatly alters the chemical property of the second atom (like Pt) by perturbing its electronic structure [23]. DFT calculations on various Pt/Ru clusters also showed that the addition of Ru disturbs the electronic structure of the Pt [32]. Experimental evidence of a ligand mechanism associated with MOR was provided by XAS measurements done by McBreen and Mukerjee. They correlated the reduction in Pt-Pt bond length associated with Pt/Ru to increased d-band vacancies [38]. Later the electronic effect of Ru on Pt on MOR was further proved by Tong *et al.* using NMR studies [39][40]. They found that addition of Ru to Pt causes a decrease in the density of states of Pt, ultimately reducing the π back donation and weakening the Pt-CO bond. *In-situ* IR electrochemical studies on CO oxidation also provided some evidence of the ligand mechanism, as a higher CO stretching frequency was observed for PtRu (50:50) system in comparison to pure Pt. However, this result is not conclusive, as a similar effect can also occur due to reduced CO lateral interaction [35]. In contrast to CO oxidation, similar studies on MOR did not support any ligand effect except for a bulk Pt/Ru system, in fact the CO stretching frequency associated with PtRu nanoparticles was found to be much lower than that of Pt particles [36]. All the above mentioned studies put forward experimental evidences for supporting both the ligand and bifunctional mechanism, but could not determine the dominant mechanism, until Scott *et al.* using XAS studies correlated both BF and ligand mechanism to particle size and morphology of Pt/Ru system [41]. They concluded that the bifunctional mechanism is dominated by monodispersed small Ru islands in the PtRu system and the ligand effect by the presence of large Ru islands. Such a behavior is attributed to the extent of oxidation of Ru islands, as it is expected that large islands are highly oxidized and thus exerting a higher ligand effect. In contrast, small Ru islands experiencing a reverse ligand effect make them less oxidized and

can activate water at low potential (0.3 V) thus facilitating the bifunctional mechanism. The presence of these oxide fractions in Pt/Ru alloy system was further confirmed by XPS studies. The XPS showed the presence of Ru in its hydrous and anhydrous oxidic form and in fact former is a mixed electron and proton conductor and the latter an insulator [42][43]. Thus, not only the PtRu structures determine the mechanism of methanol oxidation but also play a crucial role in proton conductivity.

2.4 Challenges in DMFC technology

The reduced complexity of the technology, liquid nature of the fuel, cheap and abundant availability of the fuel makes DMFC much more attractive than a PEMFC. Companies like Smart Fuel cell AG, MTI micro, Oorja protonics and Antig produce commercial DMFC for military and stationary application. Apart from these, several electronic companies claimed to have DMFC energy source for their electronic equipments like laptops, mobile and MP3 players (Toshiba Samsung, Motorola etc). What makes DMFC a potential candidate for these applications lies in the fact that they can store a lot of power in a confined space and are capable of supplying small power over a long period of time. However, due to slow kinetics of the MOR and mixed potential due to methanol crossover the performance of the DMFC is much lower than the H₂-PEMFC.

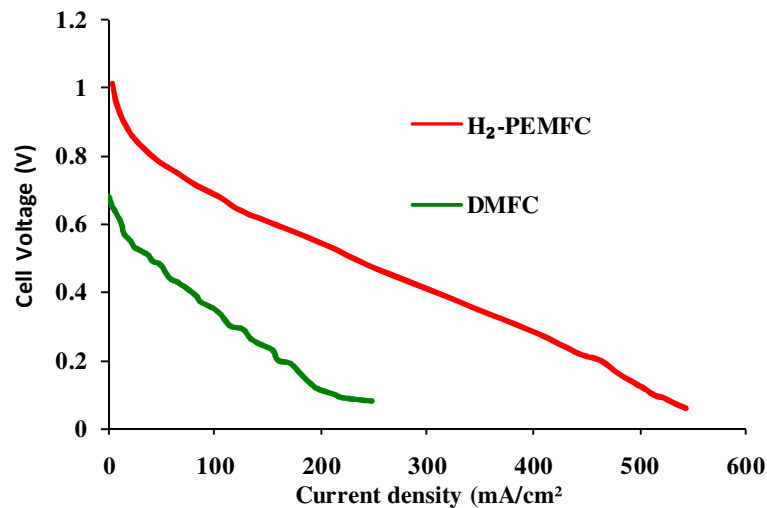


Figure 4: Polarization curve for H₂-PEMFC and a DMFC (it is to be noted that Pt loading of the DMFC is twice that of H₂-PEMFC)

To compare their performance a polarization curve for both DMFC and H₂-PEMFC is shown in Figure 4. DMFC are often encountered with drawbacks like catalyst degradation, Ru dissolution and methanol cross over which prevent its early and extensive commercialization. These drawbacks will be explained in brief in the section below.

2.4.1 Degradation of catalyst and Ru dissolution

Degradation in fuel cell catalysts has got considerable attention as the catalyst activity can have tremendous influence on the fuel cell performance and durability. A relatively high catalytic activity is expected from those systems having a large electrochemically active surface area (ESA), which facilitates the catalytic reaction. Catalyst degradation in the form of particle growth, particle aggregation, and de-alloying can lead to an effective decrease in the ESA, which are in turn correlated to Pt dissolution (or the less noble alloy metal) and re-deposition [44][45]. ESA losses are further aggravated by carbon support corrosion leading to complete degradation of the catalyst structure [46]. Thermodynamically under fuel cell operating conditions (operating voltage 0-0.9 V) Pt is expected to be more stable than C, as carbon can get oxidized at $E^0 = 0.27$ V to CO₂ as shown in equation 7.



Although this reaction is greatly suppressed in normal fuel cell operation due to the slow kinetics (relatively low temperature), in long term operation significant carbon corrosion and subsequent Pt agglomeration is expected [47][48]. In contrast to carbon, oxidation of Pt is expected to take place at higher potentials $E^0 > 0.85$ V as shown in equation 8.



The oxidic phase can undergo dissolution in the presence of water and subsequently get reduced to form Pt precipitates in the membrane or get redeposited on a different Pt surface. Thus, an overall decrease in ESA is expected due to Pt dissolution. Thus Pt dissolution as well as carbon support corrosion should be minimized for achieving long term durability of the fuel cell. The influence of fuel cell operating parameters, like voltage, current, temperature, and humidification level on carbon corrosion and Pt dissolution has been addressed in several reviews. For example it is found that high voltage cycling of the fuel cell as in the case of start

stop cycle can lead to a dramatic decrease in the ESA as during these conditions the fuel cell potential can go as high as $1.5 \text{ V} > E^0$ favoring the formation of more PtO as in equation 8 [49]. Further carbon corrosion as described in equation 7 is also more favorable under these conditions leading to severe degradation of the electrode structure. From equations 7 and 8 it is also clear that water plays a decisive role in both carbon corrosion and Pt dissolution and thus high humidity and flooding can also lead to catalyst degradation [50]. In contrast to the cathode the anode of the fuel cell experiences less harsh conditions due to less dynamic potentials thus the severity of the anode degradation is much less than that of the cathode. Accelerated degradation of the anode catalyst can occur during a cell short circuit or when the cell is forced to operate in a fuel starvation mode. Fuel cell starvation has a detrimental effect on the fuel cell durability as prolonged starvation can lead to high anodic potential which in turn lead to carbon corrosion and catalyst degradation [51][52]. Catalyst and support degradation in fuel cells are schematically shown in Figure 5.

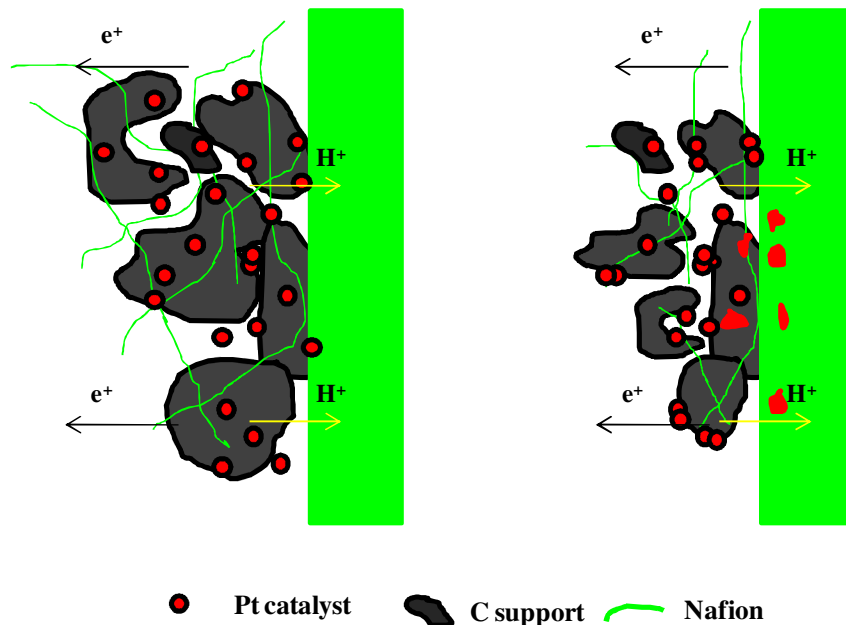


Figure 5: Schematic representation of catalyst and support degradation in fuel cells.

Various degradation processes taking place in a fuel cell are summarized in Table 2.

Degradation of fuel cell components	Fuel cell conditions leading to degradation	Effect
Carbon support	Start-stop cycle, fuel starvation, flooding, higher operating temperature.	Catalyst sintering, low electronic conductivity, fuel crossover.
Catalyst	Start-stop cycle, fuel starvation, flooding, higher operating temperature, poisoning (CO, methanol), adsorption of other metal (Fe, Ru etc).	Loss in activity of the catalyst.
Ionomer membrane	High temperature, low humidity attack by radical (OH^\cdot), substitution of proton by metal ions (Na, K, Ca, Fe, Ru etc), Mechanical stress.	Decreased proton conductivity, fuel crossover.
GDL	Start-stop cycle, fuel starvation, flooding, mechanical stress.	Low electronic conductivity, non-uniform distribution of reactant, inefficient water management.
Bipolar plates	Start-stop cycle, fuel starvation,	Poor electrical contact mechanically destabilizes the stack.

Table 2: Cause and effect of degradation of various components in a fuel cell

All the above mentioned degradation behaviors observed in a PEMFC are equally applicable to a DMFC, but high liquid environment (anode) and relatively high anodic potential (300-400mV compared to hydrogen operated PEMFC) make the anode catalyst and carbon more vulnerable to degradation. Apart from these degradation processes explained before, durability of the DMFC is further reduced by dissolution and crossover of less noble Ru metal present in the anode [49][53]. Ru is known to be thermodynamically less stable than Pt under fuel cell conditions, and thus dynamic behavior often associated with the anode of the DMFC can accelerate its dissolution [54]. Moreover, it is expected that large fractions of oxidic Ru phase

present in the Pt/Ru system are more prone to dissolution than the corresponding alloyed metallic phase. The significance of Ru in MOR was explained in the previous section, and any dissolution of Ru can decrease the MOR activity of the Pt/Ru catalyst system. Once the Ru is leached out from the Pt/Ru alloy phase or from its oxidic phase, it is precipitated in the ionic membrane or migrated to the cathode through the ionic membrane (Ru crossover) [55][56]. Ru migrated to the cathode can block the active sites of Pt thereby reducing its overall ORR activity and degrading the cathode catalyst. In fact, Gancs et al found that already a small amount of Ru on cathode can decrease the ORR of Pt/C by eight fold [57]. Also the precipitation of Ru in the membrane can increase the ionic resistivity and thus may deteriorate the overall fuel cell performance [58]. The exact mechanism of Ru dissolution and the migration path are not yet known, although operating conditions and structure of the Pt/Ru system is often correlated with Ru dissolution.

2.4.2 Mitigation strategies for catalyst and support degradation

Various mitigation strategies have been developed to address the issue of catalyst and support degradation in fuel cells. A lot of research has focused on carbon modification and used graphitized carbons and nanotubes as stable support materials for fuel cell. However, often these support materials exhibit less surface area and their decoration with platinum nanoparticles proves to be more complicated [59] [60]. Various ceramic materials such as TiO_x , SnO_x , WO_x , RuO_2 , SiO_2 , $\text{Sn-Ir}_2\text{O}_3$, (oxides) and B_4C , SiC , WC (carbides) also looked good as fuel cell catalyst support. Some of these support materials such as TiO_x and WO_x are known to act as a co-catalyst thereby increasing the overall activity of the Pt [61] [62]. However these materials are often limited by low electronic conductivity and porosity. Conducting polymers such as, polyaniline, polypyrrole, polythiophene are also promising fuel cell support materials, apart from showing high electronic conductivity they also can provide some proton conductivity and have anti poisoning effect on the catalyst. However, the introduction of these novel support materials also introduces new challenges in the fabrication of the MEA.

Structure modification of Pt itself has shown some enhanced durability. For e.g. polycrystalline nanotubes have shown excellent electrocatalytic activity and stability. More recently Liang *et al.* developed free standing Pt nano wires as fuel cell catalyst which has also shown excellent electrocatalytic activity and stability [63]. Electrochemical stability and activity of these Pt based catalyst systems are correlated to the surface energy of various planes

which the particles are composed of. It is indeed shown by Susut *et al.* that the cubic particles with higher surface energy degrade much faster than octahedral particles with a lower surface energy during methanol oxidation [64]. Thus by tuning the Pt structure one can enhance the durability of the catalyst. In the present work shape-selected particles were synthesized and were successfully tested in a fuel cell. The significance of shape selected particles in fuel cells will be discussed briefly in section 2.4.3. Alloying the pure Pt nanoparticles with different transition metals has also shown increased catalytic activity and durability. For e.g. Dai *et al.* has shown that, using Pt/W alloy catalyst an enhanced mass activity over 4 times was obtained in comparison with conventional Pt catalyst. Moreover catalyst did not show any loss in ECSA even after 36,000 cycles [65]. In the context of Ru dissolution, Liang *et al.* has found that incorporation of gold into the Pt/Ru has effectively reduced the Ru dissolution [66].

2.4.3 Shape selected Pt nanoparticles for better activity and durability

One of the key challenges in fuel cell technology is the high cost of the noble metal catalyst. It is known that in a typical fuel cell only 25-35% of the total Pt available is active [1]. Hence effective utilization of the Pt is one of the solutions to reduce the fuel cell cost. Often carbon supported Pt nanoparticles are characterized by particles with irregular shape, and often large particles and aggregates are also seen. A typical TEM micrograph of the carbon supported Pt nanoparticles is shown in Figure 6.

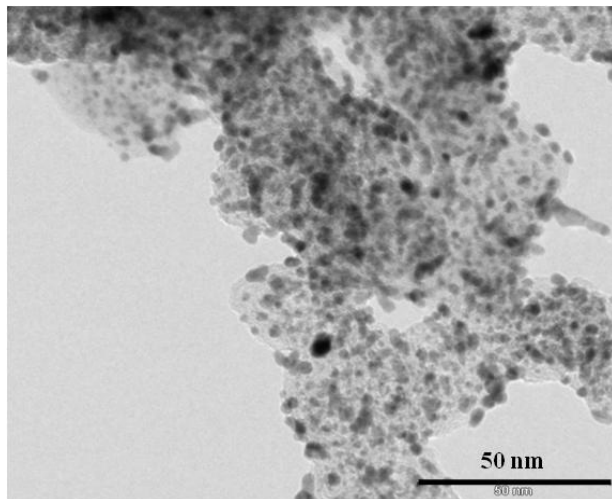


Figure 6: TEM micrograph of commercial carbon supported Pt catalyst

These large particles and aggregates are often inactive in fuel cell as, either they have reduced surface area, or their active sites are blocked. Thus for effective Pt utilization tuning the shape of the Pt nanoparticles is extremely important. Many studies have shown that altering the structure of the catalyst can have profound impact on the catalytic activity. For example Somorjai *et al.* showed that, Pt {111} hexagonal structure is 5 times more active than the cubic {100} for dehydrocyclization of n-Heptane. Further, in electrocatalysis it has been shown that, shape of the nanoparticles plays significant role in determining the overall catalytic activity. This is due to the fact that the extent of interaction of various electrolytes on the Pt surface depends on the shape of the Pt nanoparticles. It was found that, the ORR activity of the Pt single crystal surface in H₂SO₄ electrolyte decreased with Pt (1 1 1) < (1 0 0) < (1 1 0) an effect due to adsorption and the inhibiting effect of bi-sulfate anion. However in shape selected particles, depending on their shape these facets exist in different proportion. For e.g. Pt cubic nanoparticles exclusively consist of (100) facets and tetrahedral with (110). In contrast cuboctahedral particles contain both (100) and (111) facets. Thus by tuning the shape enhanced electrocatalytic activity can be achieved. In fact it has been shown by Sun *et al.* that, ORR activity of the cubic particles are 4 times higher than the polyhedrons or truncated cubes [67]. As mentioned in the previous section, apart from showing enhanced activity, shape selected particles were also found to show much better stability. Thus tuning the shape of the nanoparticles can reduce the fuel cell cost and can increase its durability.

2.4.4 Methanol cross over

Achieving a higher efficiency still remains a challenge in DMFC. The efficiency of the DMFC is greatly limited by the so called methanol crossover, i.e., the methanol fed at the anode is permeating through the membrane and reaches the cathode. Thus, the main consequence of methanol crossover is that a lot of fuel is wasted and now DMFC is operating at a much lower current efficiency given by equation 9,.

$$\eta_f = I/I_{tot}$$

equation 9

where, I is the measured electrical current at any particular cell voltage and I_{tot} is the current calculated from Faraday's law assuming that the whole of the supplied methanol is consumed. The methanol crossover in a DMFC can also lead to a significantly lowered open circuit voltage (0.8-0.6 V) in comparison to the theoretical value of 1.18 V for reversible methanol

oxidation. This is due to the fact that methanol oxidation at the cathode competes with ORR and no spontaneous current is produced above 0.9 V. The methanol crossover thus greatly decreases the Pt surface available for ORR, as the Pt cathode surface is also covered with methanol, which prevents the ORR [68][11]. Further, incomplete oxidation of methanol at the cathode can poison the cathode surface with CO intermediates. To overcome these effects a high loading of Pt at the cathode is preferred in DMFC in comparison to a hydrogen PEM fuel cell making it more expensive [69][70]. It is found that the methanol crossover is further increased by a higher operating temperature and higher methanol concentration [11][71], where the latter is preferred to extract highest energy density associated with the methanol. To minimize the methanol permeation an operating temperature around 50-70 °C and methanol concentration of 1 molar is preferred for DMFC [71].

The thickness of the membrane plays a crucial role in methanol permeation, as thinner membranes are found to be more permeable to methanol, thus Nafion 117 (215µm thick) is preferred over Nafion 115 (150µm) and 112 (60 µm) [14]. Many research groups also developed membranes with superior methanol impermeability compared to Nafion, such as sulfonated-polyetheretherketone (SPEEK), sulfonated-polyphosphazenes, polyarylenes, polyvinylidene fluoride (PVDF) etc [72][73]. Although, most of these membranes showed greater methanol impermeability compared to Nafion 117, very few showed superior fuel cell performance in comparison to Nafion. Notably polymer blends of SPEEK had produced fuel cell performance 1.3 times greater than Nafion 117 [13].

Yet another way to tackle the problem of methanol crossover is employing cathode catalysts which are methanol tolerant or do not activate MOR. Pt alloyed with transition metals (Fe, Cu, Co etc) was found to be higher methanol tolerant compared to pure Pt catalyst but could not eliminate the effect completely due to the presence of Pt in these systems [74]. The use of metal-chalcogenide systems (MoRuX (X-S,Se,Te)) as cathode catalyst was yet another solution for methanol crossover, as these system showed good ORR activity and at the same time were found tolerant to methanol [75][76]. Out of the various metal chalcogenides, RuSe_x proved to be promising, but fuel cell performance was much less (40%) comparable to pure Pt with the same metal loading [12][77]. Thus, methanol crossover in DMFC still remains a challenge and solving this problem can bring a dramatic change in the efficiency of the DMFC.

2.4.5 Methanol cross over and bi-functional operation

Methanol cross over in DMFC can lead to the bi-functional mode of operation in DMFC. During bi-functional operation, the DMFC is split into two parts. The fuel cell region close to methanol outlet and oxygen inlet acts as galvanic region (normal fuel cell operation) and the region close to the methanol inlet and oxygen outlet acts like electrolytic region. The bi-functional mode of operation in DMFC usually takes place in an event of low oxygen flow or under oxygen starvation conditions. During low oxygen flows, there is not enough oxygen to sustain the ORR, especially at the oxygen outlet regions. Instead, in these regions, crossover methanol from anode oxidizes and form CO_2 and H^+ . Now the protons formed from the oxidation of methanol diffuse back to the anode and get reduced to hydrogen gas. The reduction of the proton takes place at the expense of the electron produced in the galvanic regions, especially from the oxygen inlet regions, where it has enough oxygen feed. Thus during bi-functional operation current is consumed as well as produced in DMFC. Schematic representation of the bi-functional operation is shown in Figure 7.

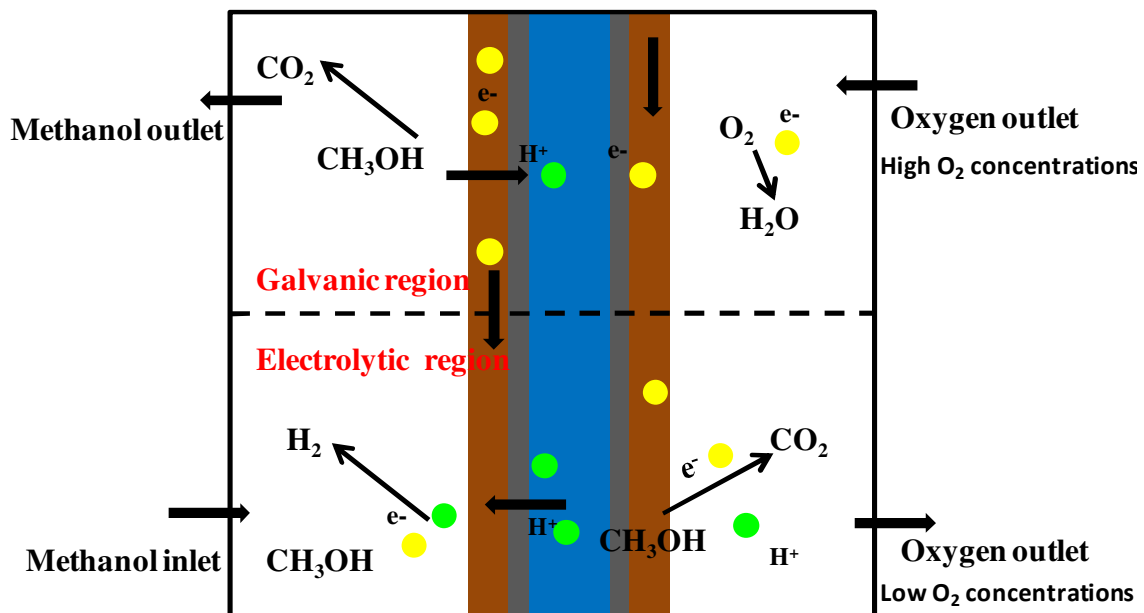


Figure 7: Scheme showing the splitting of DMFC into galvanic region and electrolytic region during bi-functional operation

The bi-functional operation is experimentally shown by combined neutron imaging and spatially resolved current distribution measurements [78]. It was found by Kulikovskiy *et al.*

short time operation of DMFC in bi-functional mode can actually activate the catalyst and thereby increase the fuel cell performance [79].

2.5 Non uniform distribution of current density and spatially resolved *in-situ* studies

Direct methanol fuel cell is often affected by a non uniform distribution of current, which can lead to an overall decrease in the power density and locally increased degradation process. This in-homogeneity may be in turn correlated with other in-homogeneities arising in the fuel cells, which are explained in Table 3.

TYPE OF IN-HOMOGENEITY	REASONS	EFFECTS
Methanol flow [80][81]	Blocking with CO ₂ gas Low flow rates Low methanol concentration Flow field geometry	Methanol starvation accelerates anode degradation (both catalyst and support) Low fuel cell performance
Oxygen flow	Blocking with water Low flow rates	Low fuel cell performance
Temperature [82]	Improper cooling (stack) Poor thermal contact between end plate and MEA due to corrosion.	High temperature Sintering of catalyst Higher methanol permeation Low temperature Low fuel cell performance
Catalyst distribution	Poor coating method Poorly synthesized catalyst	Under utilization of catalyst Localized degradation

Table 3: In-homogeneities in direct methanol fuel cells

For various reasons explained in Table 3, the distribution of current is non uniform across the fuel cell active area, which can adversely affect the fuel cell performance and durability. Further, these in-homogeneities are expected to worsen as in the case of a fuel cell stack or passive fuel cell system where the use of auxiliary units such as methanol pump, external heater, air blower are minimized. The use of these auxiliary units are non desirable as these units need additional power for operation and this power may be taken from the fuel cell itself or by an external power source like batteries which again need to be charged regularly. In

order to evaluate the extent of degradation and performance losses, it is necessary to monitor the different type of in-homogeneity associated with DMFC and this is usually accomplished by spatially resolved analytical techniques. Spatially resolved studies can be carried out on a working fuel cell or by *ex-situ* analyzing different components of the fuel cells (mainly MEA). Various analytical techniques from which we can get spatially resolved information of a DMFC, either *in-situ* or in *ex-situ* conditions are summarized below.

Technique	Information	Advantage/Disadvantage
Electron microscopy techniques (TEM and SEM) [83][84]	Particle size distribution, morphology. Atomic resolution of catalyst structure possible. Qualitative information through EDX and EELS possible	Only <i>ex-situ</i> analysis possible Mostly destructive method
X-ray diffraction [84]	Change in particle size, changes in phase.	Both <i>in-situ</i> and <i>ex-situ</i> possible No information about the amorphous phase (long range order preferred)
X-ray and neutron imaging [85] [78]	Visualization of water, flooding, evolution bubbles etc.	<i>In-situ</i> studies possible Require synchrotron or neutron source No structural information of catalyst
IR and Raman imaging [86]	Distribution of water Distribution of temperature	<i>In-situ</i> studies possible No structural information of catalyst
NMR imaging [87]	Distribution of water, mobility of water across membrane	<i>In-situ</i> studies possible No structural information of catalyst
X-ray photoelectron spectroscopy [88]	Oxidation state of the catalyst	Only <i>ex-situ</i> analysis possible Mostly destructive method
X-ray absorption spectroscopy	Catalyst structure, information of amorphous phase, adsorbate coverage	<i>In-situ</i> and <i>ex-situ</i> studies possible Require synchrotron source
Current distribution measurements	Direct visualization of electrochemically active and inactive regions.	<i>In-situ</i> measurement No structural information of catalyst

Table 4: Different analytical techniques for spatially resolved fuel cell studies

From Table 4 it is clear that the right choice of the analytical technique depends on the kind of information we require and conditions under which the experiments are feasible. Thus, although XPS, TEM give valuable information about oxidation state and structure of the catalyst no *in-situ* information of the catalyst structure is possible, as both these techniques need ultra high vacuum (UHV) conditions. Furthermore sample preparations of these techniques are destructive in nature, so that continuous monitoring of the samples is not possible or in other words structural information of initial (pristine) and end of life (EOL) samples are only possible. In contrast to these techniques neutron and X-ray imaging techniques offer more versatility, as they can monitor the fuel cell under various operating conditions. By these imaging techniques one can visualize the water transport mechanism, evolution of water or bubbles etc and from this information one can optimize the water management and fuel cell components.

Spatially resolved current density measurements are yet another powerful technique by which one can monitor the electrochemically active areas of an operating fuel cell. This is usually achieved by dividing the fuel cell active area into different segments connected to printed circuit board (PCB) with gold plated contacts which record the segment currents. Using a similar set up, Park et al have carried out extensive investigations on the influence of current distribution on various operating parameters like oxygen and methanol flow rate, output current, temperature and flow field geometry. More recently, Schröder *et al.* combined both neutron and current distribution measurements and correlated the GDL wettability to fuel cell performance. In these studies they divided an MEA into two parts (for both anode and cathode), one side with a hydrophilic GDL and another with hydrophobic. During a combined neutron imaging and current distribution measurement of these systems, they visualized poor water management for a hydrophilic GDL by neutron imaging and at the same time they obtained a low power density for the hydrophilic segments.

Although these techniques give sufficient information about the reactant transport and water distribution, they are limited by the fact that they do not provide insight into the catalyst structure and durability. XAS is one technique which is routinely used in the catalysis and electrocatalysis community to probe the structure and chemical environment of the catalyst in action. The big advantage of XAS spectroscopy over other surface techniques like XPS, or microscopic technique like TEM, is the fact that the measurements do not need any ultra high vacuum conditions. This means *in-situ* and operando measurements would be possible using XAS, which gives information about the adsorbate, oxidation state and structure of the catalyst

in real operating conditions. In addition to all these facts, XAS has the further advantage that the measurements can be even carried out on amorphous sample or samples without long range order. This is extremely important to the catalysis and electrocatalysis community as many of the active sites are on amorphous nanoparticles. This is a great advantage over XRD, which needs long range order. The present work involves extensive use of XAS for characterizing the catalyst both *in-situ* and *ex-situ*. Therefore, the theory and data analysis of the XAS need to be described briefly in the next chapter.

3 XAS and *in-situ* investigation of fuel cells

3.1 Theory of XAS

XAS is a special case of interaction of electromagnetic radiation with matter. Assuming that an electromagnetic radiation is hitting matter, and if we place a detector before and after the sample, we will find that there is a loss in intensity after the sample. This loss in intensity is due the absorbance of the radiation by the matter and it follows the Beer-Lambert law of absorption shown in equation 10,

$$I = I_0 e^{-\mu(E)x} \quad \text{equation 10}$$

where I is the transmitted intensity, I_0 is the incoming intensity, x the sample thickness and μ the absorption coefficient of that matter.

If the energy of the electromagnetic radiation (X-ray photons) is slightly higher than the core level binding energy of the matter then a core level electron is ejected to the valence band. If the energy of the X-ray photon is much higher than the core level binding energy, then the electron will be released to the continuum. Once the electron is released to the continuum, it interacts with surrounding atoms. The outgoing electron is now called a photoelectron, which is backscattered by the surrounding atom. The back scattered waves now interact constructively or destructively with the outgoing photo electron giving a complete X-ray absorption spectrum as shown in the Figure 8. Since the core level binding energy is unique to a particular element, XAS also gives element specific information provided that the measurements are carried out at any of the absorption edges (K, L₁, L₂, L₃ etc) of the corresponding atom. XAS measurements are usually carried out at large synchrotron facilities, where tunable and intense radiation sources are often accessible.

The XAS spectra are noticeably characterized by three regions, the edge region, X-ray absorption near edge (XANES) region and the extended X-ray absorption fine structure (EXAFS) region. The step like feature seen in the XAS spectrum is the edge. The step like feature arises due to the fact that at this energy the photoelectron is excited to the continuum.

Depending on the oxidation state and the type of element the edge can have a different line shape with a shoulder or a strong peak at the top of the step. Often the edge position is found to be shifted with different oxidation states of the same element. These characteristic features of the edge thus give information about the oxidation state of the element, thus serving as a complimentary technique to XPS.

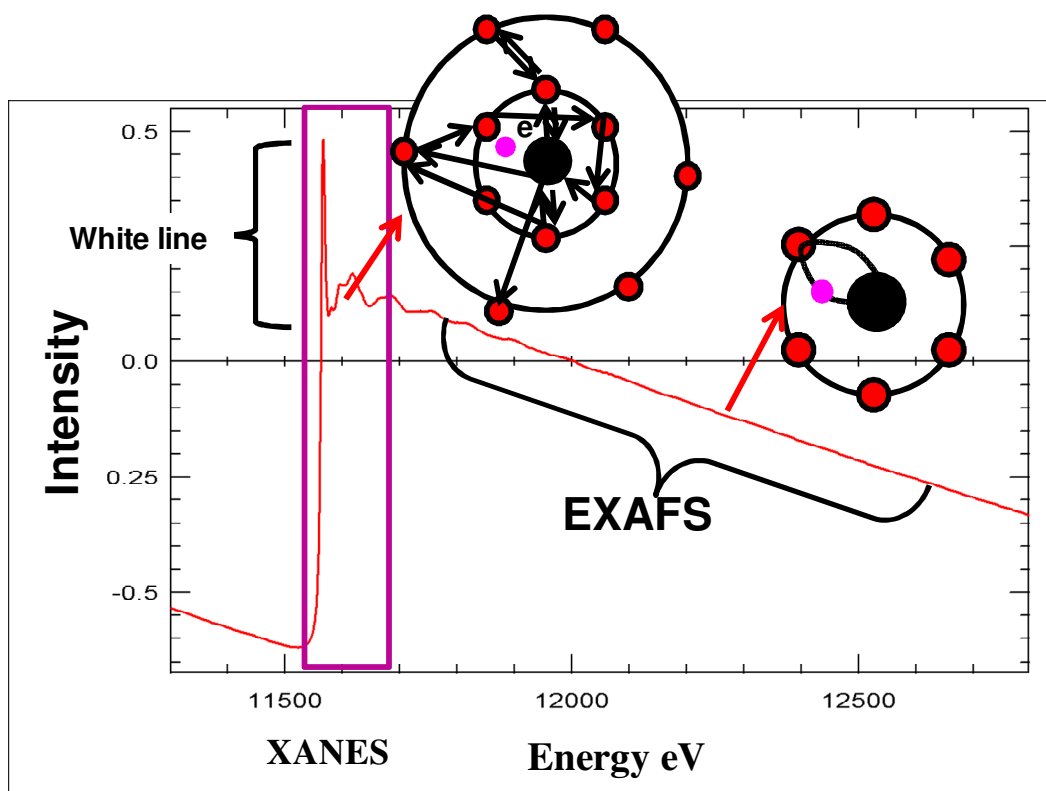


Figure 8: XAS spectrum at Pt L_3 edge describing various interactions of the photoelectron

The whole spectral region in the range -25 to 200 eV with respect to the edge is called X-ray absorption near edge region (XANES). XANES is characterized by the multiple scattering of the photoelectron with the surrounding atom. The energy of the photoelectron is comparatively low in the XANES region which is characterized by the high mean free path and can thus undergo several multiple scattering events. The line shape of the XANES greatly depends on the formal valence of the atom, coordination environment and extent of filling of the excited state. In catalysis, the extent of filling of the excited state is greatly depending on the adsorbate and the ligands which also impose characteristic line shapes to the XANES spectra. Thus, one can get information about the nature and coordination geometry of the adsorbate by analyzing the XANES region. Although rigorous mathematical calculation is required to solve the

XANES region, doing so can give information about the specific adsorbate. XANES region thus gives information which are complimentary to IR and Raman.

The region around 150 to 1000 eV above the absorption edge is called the EXAFS region. This region is characterized by the single scattering event of the photoelectron due to its relatively large kinetic energy. This high energy photo electron will interact with surrounding atoms and will get back scattered as mentioned before. The backscattered wave interacts constructively or destructively with the incoming photoelectron depending on the phase of the backscattered wave. The phase and intensity of the back scattering wave is dependent on the position and number of the surrounding atoms. Therefore analyzing these EXAFS oscillations can give information on the number and distance of the surrounding atoms.

3.1.1 XAS data processing

XAS analysis basically involves solving the Schrödinger equation $E\Psi = H\Psi$, as XAS involves purely quantum mechanical events and thus gives the electronic structure of the absorbing atom. The tedious effort by John Rehr (University of Washington) and co-workers developed a new code 'FEFF' (most recent of these FEFF9) which does the XAS analysis by solving the Dirac-Fock equation. More details concerning FEFF and supporting packages could be found in <http://cars9.uchicago.edu/ifeffit/>. Many software packages with user friendly graphical interfaces are available with inbuilt FEFF code to do the data reduction and analysis part. In the present work, most of the data reduction and analysis part was done using Athena and Artemis software packages [89].

3.1.2 Data analysis of XANES

It has been observed that the line profile of the XANES regions has a strong dependency on the oxidation state of the element as well as on the nature of the adsorbate species on the surface. For instance, hydrogen adsorption on the Pt surface shifts the edge to a higher energy (Pt L₃ and Pt L₂) and also induces an edge peak broadening [90]. The $\Delta\mu$ technique is one such technique, where the magnitude and line shape of μ is evaluated. The $\Delta\mu$ technique is basically a differential technique where XAS of spectrum of interest is subtracted from a reference spectrum and the obtained difference spectrum is matched with theoretical reference spectrum for a modeled or a simulated system. Here, the XAS spectra of interest could be XAS measured in *in-situ* conditions say in different gaseous or liquid atmospheres as in

heterogeneous catalysis or at different electrochemical potentials or electrolyte as in electrocatalysis. In most cases an XAS spectrum measured in a condition, where the catalytic or electrocatalytic active regions are free of adsorbate is chosen as the reference spectrum. For e.g. a Pt electrode at 560 mV was used as reference spectrum for getting information about the type of adsorbate covered at the catalyst surface at another potential. Now the difference spectrum can be represented by equation 11;

$$\Delta\mu = \mu_{(ads)} - \mu_{(ref)} \quad \text{equation 11}$$

where $\mu_{(ads)}$ is an XAS spectrum of interest and $\mu_{(ref)}$ is a reference spectrum in which the system of interest is pristine. These difference spectra are fingerprinted with different simulated spectra. The schematic representation of the data processing for the XANES is shown in Figure 9. The importance of FEFF lies in creating simulated models for $\Delta\mu$ signatures. A structural model, which is closely matching the experimental system, is created using FEFF. Theoretical spectra will be calculated by full multiple scattering calculations using muffin-tin potentials. More details about the calculation can be found in ‘Introduction to XAFS – a practical guide to X-ray absorption fine structure spectroscopy’ by Grant Bunker [91].

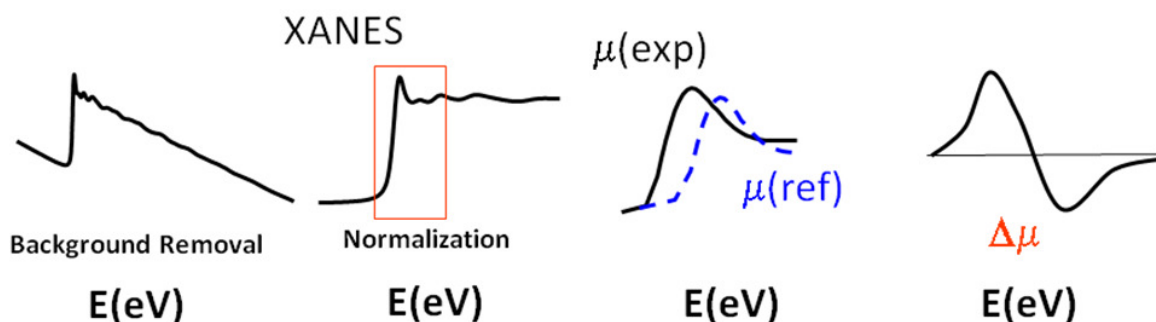


Figure 9: Schematic representation of data processing procedure for XANES analysis

Now a series of new structural models is created from the existing model taking into consideration all the possible structural changes (introducing adsorbate etc), that the system

can have in real experimental conditions. The theoretical spectra for the new systems are also calculated from FEFF, as explained before. Theoretical $\Delta\mu$ signature is calculated from above systems by taking the difference using the simulated clean spectra. Various theoretical $\Delta\mu$ signatures obtained are now compared with the experimental $\Delta\mu$ signature to get information on the nature of bonding, bonding sites, bonding species etc. The pure Janin cluster and adsorbed cluster used for the simulation of the theoretical XANES spectra is shown in Figure 10.

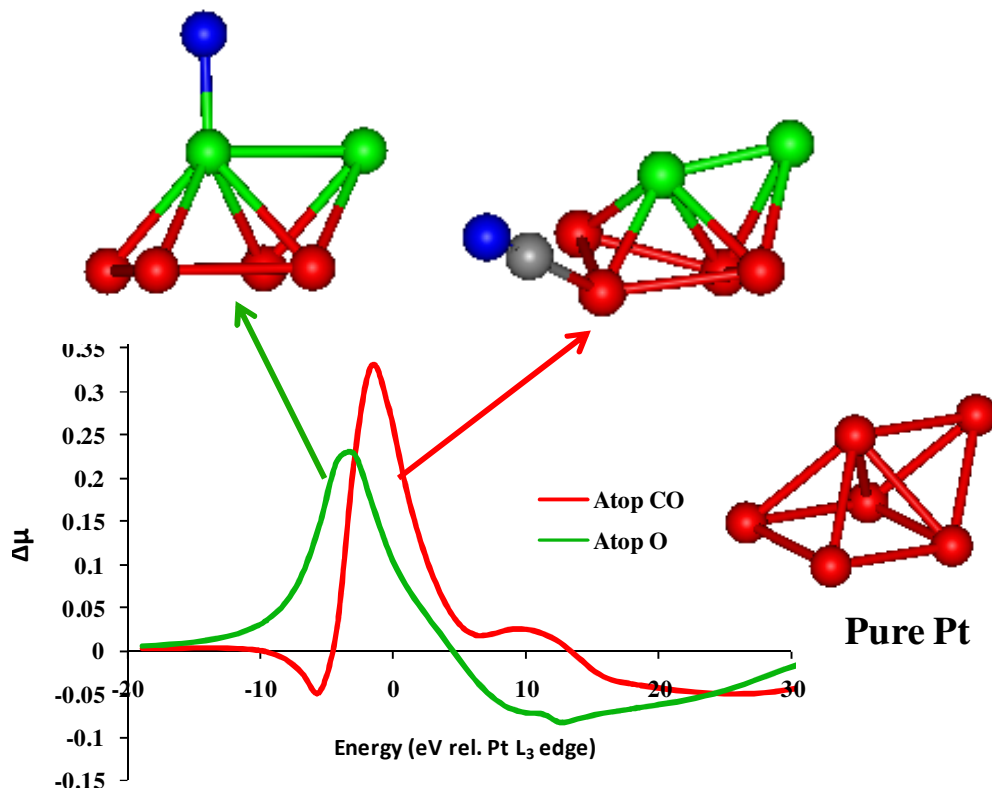


Figure 10: Various Pt, Pt/Ru clusters used for getting theoretical $\Delta\mu$ signature. The graph showing the theoretical $\Delta\mu$ signature of Atop adsorbed CO, and O on Pt/Ru cluster (calculated by FEFF 8)

As can be seen from Figure 9, the processing of the XAS raw data for XANES analysis involves many steps. The raw data is first imported into the Athena software. Then the data are checked for possible energy drift during the acquisition process, which can be due to instability in the monochromator etc. This is done by aligning the reference foil spectra, which were measured simultaneously during each scan.

3.1.3 Data analysis of EXAFS

The analysis of EXAFS data basically involves the solving of the EXAFS equation shown below (equation 12).

$$\chi(k) = \sum_j \frac{N_j S_o^2 f_j(k) e^{-\frac{2R_j}{\lambda(k)}} e^{-2k^2 \sigma_j^2}}{k R_j^2} \text{Sin}[2kR_j + \delta_j(k)] \quad \text{equation 12}$$

The terms R_j (bond distance), σ (Debye Waller factor), N (coordination number), which describe the coordination environment of the absorbing atom are evaluated by a fitting procedure like non-linear regression analysis. The other terms like S_o^2 (amplitude reduction factor) and δ_j (phase shift), which are element specific, are determined by FEFF from an input structural model close to the experimental one. The processing of the EXAFS data involves the extraction of the (χ) function from the XAS spectrum represented by equation 13.

$$\chi(E) = \frac{\mu(E) - \mu_0(E)}{\Delta\mu_0(E)} \quad \text{equation 13}$$

This is accomplished by determining and removing a post-edge background function ($\mu_0(E)$) from the experimental, which represents the adsorption of an isolated atom. The term in the denominator $\Delta\mu_0$ is the edge jump at the threshold energy E_0 . The whole process described

above is usually done in the Athena software. The raw data is imported into the software and pre-edge correction is done. Then the absorption edge is determined by taking the derivative maxima of the spectrum. The whole spectrum is normalized before a post-edge correction is done in the range of 150 to 900 eV to estimate $\mu_0(E)$ and thus extracting $\chi(E)$. $\chi(E)$ is then converted to $\chi(k)$ according to the equation 14.

$$k = \sqrt{\frac{2m(E - E_0)}{\hbar^2}} \quad \text{equation 14}$$

The $\chi(k)$ weighted to $\chi(k^2)$ or $\chi(k^3)$ depending on the Z value of the scattering atom, e.g., heavier scattering atoms like Pt involve a k weighting of 3 and lighter scattering atoms like O need only a k weighting of 2. The weighted $\chi(k)$ is then Fourier transformed into R space according to equation 15.

$$FT(R) = \frac{1}{\sqrt{2\pi}} \int_{k_{\min}}^{k_{\max}} k^n \chi(k) e^{i2kR} dk \quad \text{equation 15}$$

The schematic representation of the data reduction procedure of EXAFS is shown in Figure 11. Finally the reduced data is fitted using a theoretical structural model. Fitting is carried out using the Artemis software either in k or R space.

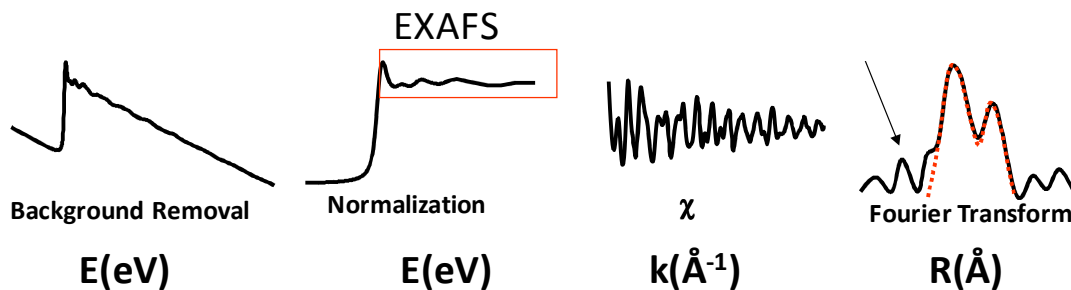


Figure 11: Schematic representation of data processing procedure for EXAFS analysis

3.2 In-situ investigation of fuel cell reaction by XAS

Development of new and modern synchrotron facilities around the world allowed many research groups to access the XAS technique. Nowadays XAS technique is widely used by biologists, chemists and materials scientists to investigate their materials. What makes XAS attractive in comparison to other techniques (TEM, XPS etc) is the fact that, XAS measurements could be done under extreme conditions. For e.g. XAS spectra can be recorded using a diamond anvil cell where the sample is experiencing high temperature and pressure similar to the core of the earth. In electrochemistry and fuel cell research, XAS has been used to investigate the structure of the catalyst in *ex-situ* conditions as well as under various electrochemical conditions. For e.g. detailed structural investigation of Pt/Ru catalyst was done by McBreen and Mukerjee and they first observed the splitting in EXAFS pattern for the alloy catalyst [92]. This is due to the fact that, Ru sit in the fcc lattice of the Pt with a shorter bond length than Pt-Pt, which results in the destructive interference of the photoelectron wave. Later, Hwang *et al.* used XAS to probe the formation mechanism and chemical state of Pt/Ru catalyst [93]. XAS measurements were also successfully carried with electrochemical cells, for e.g. Herron *et al.* tracked the surface oxide formation on Pt/C, under various electrochemical potentials [94]. The first *in-situ* XAS study under real fuel cell operating conditions was reported by Viswanathan *et al.* In this study they tracked the XANES spectra of anode catalyst (Pt/Ru) of a fuel at Pt L₃ and Ru K edge operated using reformed gas (H₂/CO). Later *in-situ* fuel cell XAS measurements were carried out by many research groups, mainly, Roth's, Russel's, and Principi's working group. It is worth to note few of their studies for e.g. Roth *et al.* in their *in-situ* fuel studies determined the OH and CO coverage and adsorbate sites on Pt/Ru catalyst [95]. In contrast, Russel and co-workers determined the mechanism by which Ru and Mo increase the tolerance of the Pt/C [96]. Further they investigated through XAS, the potential dependence segregation and surface alloy formation of Ru modified Pt. Principi *et al.* developed *in-situ* fuel cell which is capable of acquiring both XRD and XAS measurements. The thinned down graphite X-ray window used in their studies enabled them to get low noisy fluorescent data, which is quite crucial for samples with very low Pt loading (0.1mg/cm²) [97].

Recent developments in X-ray optics show the transfer of conventional XAS beamlines to QEXAFS (Quick) beamline and later to energy dispersive XAS (EDXAS). These new beamlines use either Laue-case bent crystal (EDXAS) or oscillating monochromator

(QEXAFS) by which a complete XAS spectrum could be obtained in milli-seconds to sub-pico-seconds. Thus these new techniques enable time resolved investigations in fuel cells, by which dynamic events in fuel cells like, catalyst structuring, poisoning of the catalyst, reaction intermediate could be followed. For e.g. using EDXAS, Burton *et al.* studied the rate of formation of PtO in cathode catalyst under fuel cell conditions [98]. More recently, Melke *et al.* coupling QEXAFS and $\Delta\mu$ XANES techniques, investigated the relative coverage of different adsorbates involved in ethanol oxidation reaction (EOR) such as C species, OH and O in correlation with the potentials. Further, the importance of OH species for the EOR was confirmed by XAS when the magnitudes of the $\Delta\mu$ OH signatures followed the current drawn from the fuel cell [99]. In the present work, for the first time, XAS is used to get spatially resolved information of DMFC catalyst both *ex-situ* as well as in operando conditions.

4 Development of an *in-situ* XAS fuel cell for spatially resolved studies

The success of any *in-situ* XAS study greatly depends on the design of the *in-situ* cell. The cell components are usually fabricated in such a way that it withstands the experimental conditions like high temperature, pressure, oxidizing environment etc. Moreover, the X-rays should pass unhindered through the cell and the experiment's signal to noise ratio should be higher for better data handling. The fuel cell in its conventional form is not ideal for *in-situ* XAS measurements as various components of the fuel cell, like thick metallic current collectors, flow fields etc, attenuate the X-ray intensity. Thus *in-situ* fuel cells are often fabricated by drilling out a small region of the metallic end plate in such a way that the X-rays can pass unhindered. Of course, the criteria for choosing the X-ray window dimension depends on the dimension of the X-ray beam and usually the third generation synchrotron source provide X-ray spot sizes with dimensions around 20x5 mm². The signal to noise ratio can be further improved by thinning down the graphite flow fields, as thick graphite can induce background noise [100] [101]. Spectral quality can be further improved by replacing the graphite with Kapton foil, although this might perturb the uniform thermal and electrical flow.

4.1 Experimental

4.1.1 Modified fuel cell for spatially resolved XAS studies

In the present studies two different fuel cells with graphite and Kapton as X-ray window materials were optimized for *in-situ* spatially resolved XAS studies. In both designs, flow fields with fuel cell active area of 4.2x4.2 cm² with various geometries (serpentine, meander, parallel, interdigitated etc) were laser cut or drilled into graphite. In all the flow field designs the channel depth and width were kept at 1.5 mm and 2 mm, respectively. After drilling the flow fields for the graphite window cell, the overall thickness of the graphite was reduced to 2 mm by polishing. Thus this process makes sure that it leaves only 0.5 mm thick graphite below the channel, which is sufficiently thick to provide mechanical stability and sufficiently thin as an X-ray window. For the Kapton window cell, graphite was removed completely from the channel of the flow field and replaced with thin Kapton foil. In order to fabricate spatially resolved cell the graphite was preferentially removed from methanol inlet, middle and outlet

regions of the anode flow fields and oxygen inlet, middle and outlet of the cathode (area of interest). As a counter flow pattern is preferred for DMFC systems where the methanol is coming from the bottom and oxygen coming from the top, in a complete cell methanol inlet regions lie opposite to the oxygen outlet and methanol outlet to that of oxygen inlet. To allow the X-ray beam to pass unhindered, X-ray windows were also drilled in metallic current collectors designed for the cells. In order to collect the fluorescence signals and to utilize a large beam, the length of the windows were made larger compared to their height. The current collectors were also drilled for accommodating heating elements and temperature sensors.

4.1.2 Fabrication of MEA and fuel cell performance test

The performance of the newly fabricated *in-situ* cells was compared with a standard DMFC cell by measuring polarization curves. It is also to be noted that the standard cell is one cell, which has a design similar to that of the graphite window cell, but the end plates were not drilled for X-ray windows. The polarization curves were recorded in such a way that the three different cells were operated with a single MEA under the same operating conditions. MEA was prepared by a knife coating technique. 60% PtRu (Hi Spec 10.000) and 60% Pt (Hi Spec 9.000) was purchased from Johnson Matthey. An ink with a metal loading of 2 mg/cm² was prepared from the respective catalysts, knife coated onto carbon cloth GDL material and subsequently hot pressed (135 °C for 3 min) onto a Nafion[®] 115 membrane.

The prepared MEA was then assembled in each cell and tested in home-made fuel cell test station with 5 ml/min and 150 ml/min 1 M methanol and oxygen flow respectively. The cell temperature was maintained at 70 °C and 1 M methanol was preheated to 90 °C.

4.1.3 *In-situ* spatially resolved XAS test

All XAS data were recorded at beamline X1, HasyLab in transmission as well as in fluorescence geometry. Si (111) and Si (311) monochromized beam was used to record the Pt *L*₃ and Ru *K* edge spectra, respectively. *In-situ* DMFC measurements were carried out using the newly constructed fuel cells. The fuel cell was fixed at the movable XY sample stage and the different window positions were aligned with the beam. Measurements were carried out in both slow conventional mode as well as in quick XAS (QEXAFS) mode with a beam size of 15 mm x 5 mm. XAS data were then processed by the ATHENA code [14]. The raw spectra were calibrated and subsequently background corrected using the Autobk algorithm reported elsewhere [15]. The background corrected spectra were normalized in the EXAFS range of 150 to 1000 eV.

4.2 Results and discussion

The newly designed *in-situ* cells for spatially resolved XAS studies are shown in Figure 12.

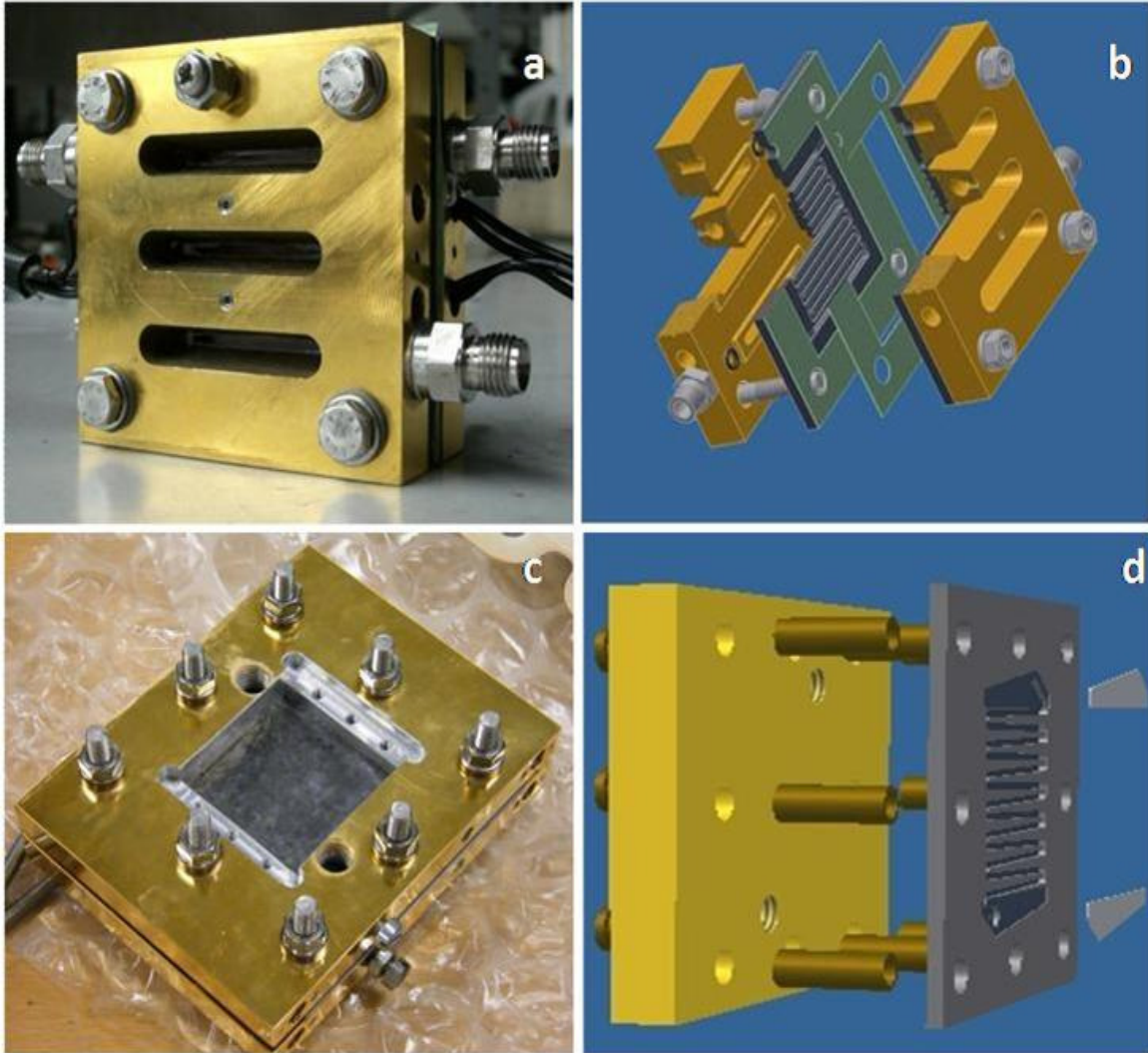


Figure 12: Schematic representation of *in-situ* cells, a) Kapton window cell, b) detailed sketch of the cell a, c) thinned down graphite cell, d) detailed sketch of cell c without X-ray window.

It is important that, the modification of the cell for XAS measurements should not induce fuel cell performance losses. The polarization curve gives a direct correlation of the performance of the various cells which is shown in Figure 13.

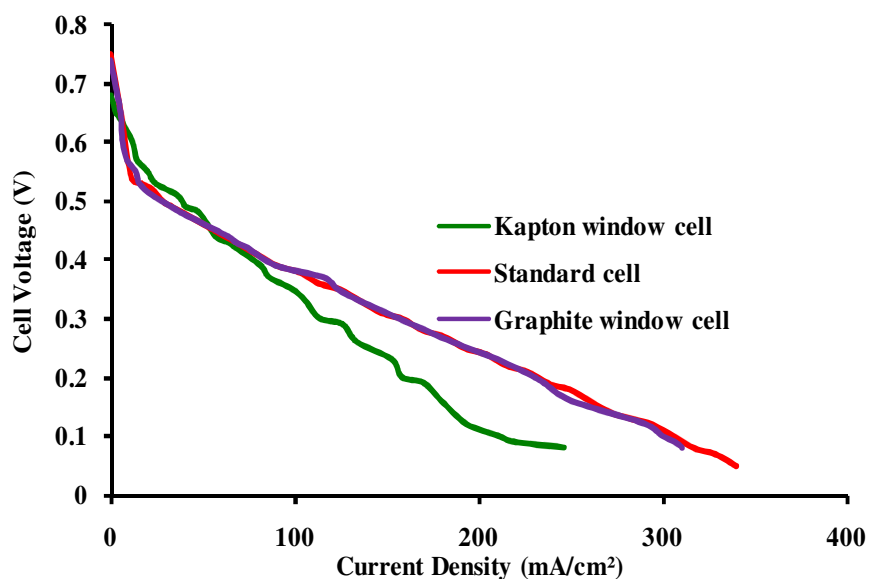


Figure 13: Polarization curves for differently fabricated fuel cells

From the polarization curves it is clear that the performance of the Kapton window cell is slightly inferior to that of the graphite window cell. This difference in the performance might be due to small perturbation in the uniform flow of heat and current caused by the presence of non electrical and thermal conducting Kapton. In contrast, the performance of the graphite window cell and the standard cell is similar, thus it is to be assumed that the small X-ray window drilled has a negligible effect on the fuel cell performance. From these studies it is clear that performance losses occurring from cell modification are negligible and are thus suitable for XAS measurements.

After the successful electrochemical characterization, *in-situ* spatially resolved XAS studies were carried out in these cells. Initial *in-situ* studies which were carried out in slow conventional scan mode (30 min per scan), were predominantly characterized by absorption spikes and the XAS analysis of these data was nearly impossible. These absorption spikes are common features of *in-situ* DMFC studies as the CO₂ bubbles formed during the process perturb the absorption. This issue was solved to a great extent by carrying out the XAS measurements in QEXAFS mode. XAS spectra obtained at the Ru K edge for both slow conventional scan and QEXAFS are plotted in Figure 14. The QEXAFS mode differs from the conventional scan mode by the fact that the monochromator is moved continuously and the whole EXAFS spectra can now be made in 25 to 120 sec. During this short acquisition time it

may be assumed that the probability of the bubble passing across the beam is low. It is also observed that when experiments are carried out in fluorescent geometry the number of spikes formed were much less than those performed in transmission mode. The transmission as well as fluorescent XAS spectra recorded simultaneously for *in-situ* DMFC, is shown in Figure 15.

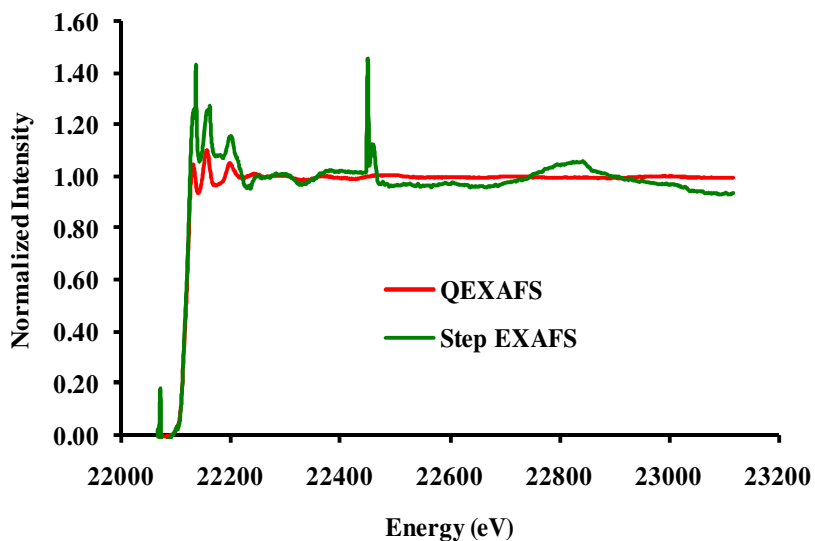


Figure 14: XAS spectra Ru K edge QEXAFS and slow step EXAFS

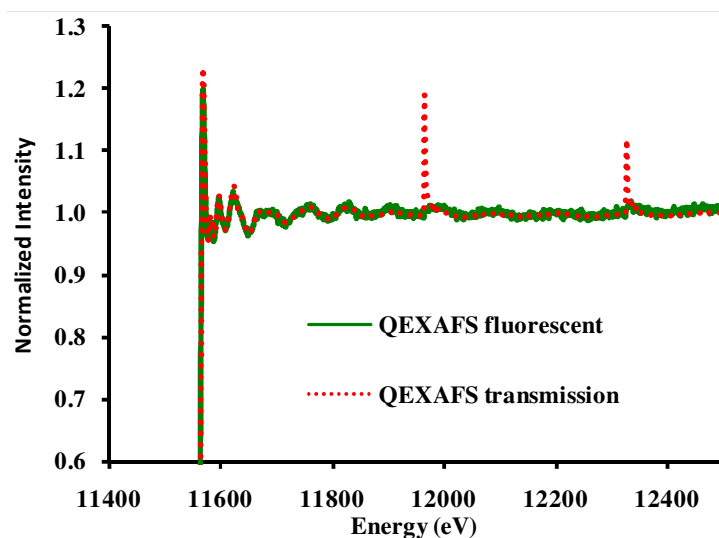


Figure 15: In-situ DMFC XAS spectra at Pt L₃ measured simultaneously in both transmission and fluorescent geometries

The occurrence of absorption spikes can be further reduced by choosing the right flow field design and carrying out the measurement in fluorescent geometry and in the present studies it is observed that using an interdigitated flow field pattern greatly reduced the absorption spike in comparison to a meander or serpentine flow field pattern.

Although, the measurements in QEXAFS fluorescent mode greatly reduced the absorption spikes, the spectral quality was much worse than the conventional slow scan. This is due to the fact that fluorescent mode of measurements is intrinsically associated with large noise (scattering from methanol, window material etc) compared to the transmission mode. Fluorescent mode of measurement is preferred over transmission, as in the latter mode Pt signals from both cathode and anode cannot be distinguished. In contrast by fluorescent mode one can preferentially get the XAS information of that electrode which is facing the fluorescence detector. It can be seen from Figure 16 that, FT of the spectra of the MEA taken in fluorescent mode with anode facing the detector is quite similar to the FT of the transmission XAS data of the MEA where the cathode is removed.

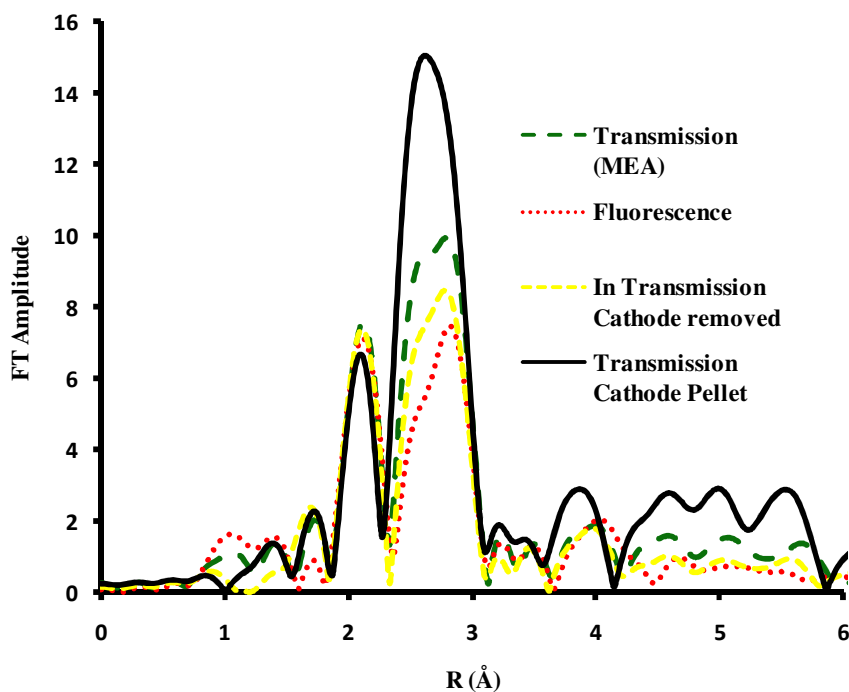


Figure 16: FT Pt L₃ edge of samples measured in various geometries

Fluorescent mode is also preferred under conditions where the element to be probed is present in low concentration. The noise associated with the fluorescence spectra is usually reduced by using energy resolved fluorescence detectors (multi element Si or Ge detectors). But these are completely incompatible with QEXAFS due to their slow response time. Thus, for the present studies, a non-energy resolved PIPS diode was used for the faster acquisition of fluorescence data. To reduce the scattering from the window materials, catalyst support and methanol, proper filters were placed in front of the PIPS diode, for e.g. a 3 mm Zn filter was used for the measurements at Pt L₃ edge and 3 mm Mo filter for the Ru K edge. The Pt L₃ edge fluorescent XAS spectra obtained for the two different cells are plotted in Figure 17.

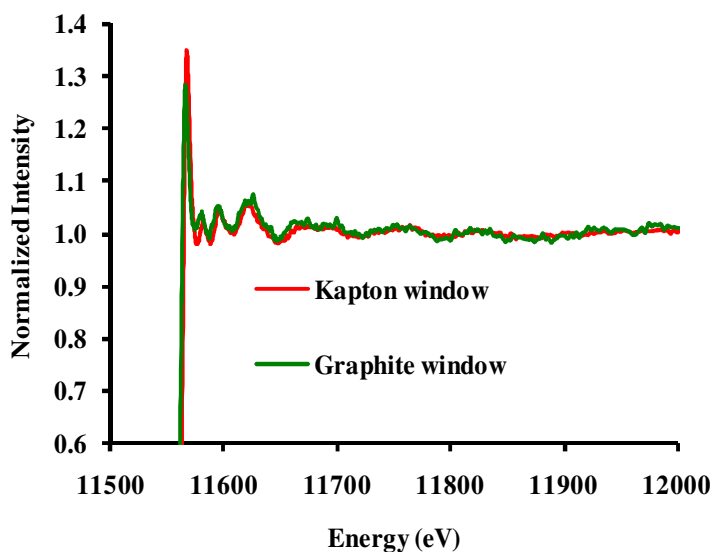


Figure 17: Pt L₃ edge XAS spectra for the two different cells

From Figure 17 it is clear that the graphite window cell has a higher noise level than the Kapton window cell. Although graphite window in the range 4-1.5 mm was successfully tested for conventional slow XAS scan, from the present studies it may be assumed that for QEXAFS DMFC studies even the graphite window with the thickness of 0.5 mm can worsen the quality of the spectra. This may be explained again by the fact that for QEXAFS fluorescence measurements there is a larger scattering noise from methanol and the window material, and the non-energy resolved PIPS diode used in the present studies is not effectively screening this noise. In the literature, low noisy *in-situ* fuel cell XAS spectra were recorded using graphite window as thin as 250 μm , but for spatially resolved studies fabricating such thin graphite flow fields for the entire fuel cell active area can affect the mechanical stability [101]. Thus

although graphite window cells are preferred for their better electrochemical performance, for the acquisition of low noise XAS data Kapton window cells are preferred. So throughout the present studies all the *in-situ* XAS data were recorded using the Kapton window cells.

5 Spatially resolved *ex-situ* studies on aged DMFC MEA

This chapter mainly focuses on the detailed and area-selective investigation of catalyst degradation in a MEA operated in a DMFC. As DMFC stacks represent a true system for practical application, the investigation of stack MEA can give an insight into its durability issues. Various analytical techniques like XRD, TEM, XAS, and EDX were combined to get a more detailed insight into the distribution of Ru in the degraded device.

5.1 Experimental

5.1.1 Fabrication of MEA and fuel cell stack operation

The process of the fabrication of MEA was explained in detail in section 4.1.2. The DMFC stack is constituted of 100 cells with an active area of 320 cm². The fuel cell stack was operated both in a test rig environment and in a DMFC system [11]. There are several differences between the operation in a test rig and a system. The significant point is that in the system there is no possibility for external heating of the stack. This means that the stack is operated at a lower temperature level than in the test rig. The chance of failures in system components and operating conditions is higher than in test rig operation. This mode of DMFC operation is expected in practical application, where the use of auxiliary units is not preferred. In system operation, the anodic water is recycled and the operation media (air and methanol) may be contaminated with impurities, which can accumulate in the stack. Also it is likely that there is methanol depletion during standstill. This can accelerate the corrosion of ruthenium. The stack was subjected to alternating operation and standstill for more than 5000 hours. The load during operation was at a current density in the range of 50-120 mA/cm² and at a temperature range from 40-70 °C, but mainly at 60 °C.

For the spatially resolved studies different regions of the ‘end of life’ (EOL) MEA from the anode side (methanol inlet, outlet and middle) and the cathode (oxygen inlet, outlet and middle) were analyzed using various analytical techniques and compared with a pristine MEA and the as-received catalysts. The MEA regions from where the samples are prepared are shown in Figure 18.

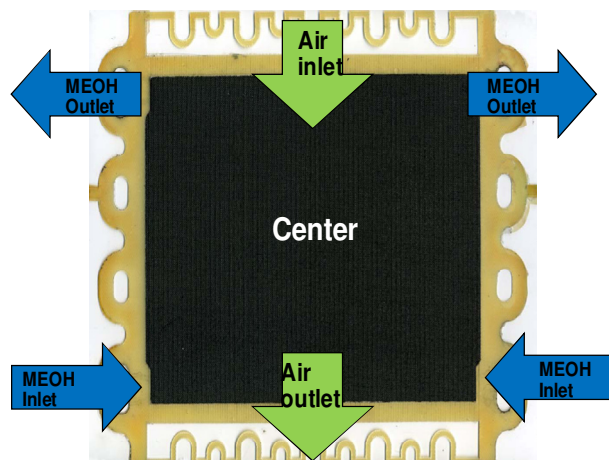


Figure 18: Sketch showing relevant investigated regions in an MEA

5.1.2 X-ray diffraction (XRD)

The X-ray diffraction measurements were predominantly carried out to get information on the crystallite size of the catalyst particles. The X-ray diffraction was mainly performed using a STOE STADI-P diffractometer with germanium monochromized Cu K_{α} radiation in transmission geometry. The pattern observed for every sample was refined using the FULLPROF suit package. The crystallite size was calculated using the Scherrer equation

$$FWHM = \frac{K \times \lambda \times 57.3}{D \times \cos \theta}$$

5.1.3 Transmission electron microscopy (TEM)

To obtain the morphology, particle size and distribution of the catalyst particles, TEM studies were carried out using a Philips CM20 TEM with an acceleration voltage of 200 kV and LaB₆ cathode. The samples for the TEM were prepared by ultra microtomy. For the ultra microtome sample preparation the GDL of the MEA was removed and thin cuts of the MEA were made from different regions using a knife. These thin cuts were embedded in an Araldite 502 resin (SPI Supplies, Inc.). The embedded samples were cured at 60 °C overnight. From the cured samples 200 nm and 70 nm thin cuts were made using a Reichert-Jung ultracut microtome. 70 nm thick samples were preferentially used for TEM analysis.

5.1.4 Scanning electron microscopy (SEM) and energy dispersive X-ray (EDX) mapping

EDX mapping analyses were carried out to get information about the elemental distribution in the MEA. EDX mapping was carried out on 200 nm thick ultra thin cuts of MEA samples using a Zeiss 962 Scanning Electron Microscope equipped with an energy dispersive X-ray detector for elemental analysis and mapping. All measurements were carried out at an accelerating voltage of 20 kV.

5.1.5 X-ray absorption spectroscopy (XAS)

Details of the experimental set up for the XAS studies are given in section 4.1.3. For the XAS data analysis the raw spectra were calibrated and subsequently background corrected using the Autobk algorithm reported elsewhere [15]. The background corrected spectra were normalized in the EXAFS range of 150 to 1000 eV. The EXAFS fitting analysis was done on the processed data using ARTEMIS [13]. At each edge, three different scattering paths were used (Pt-Pt, Pt-Ru, Pt-O and Ru-Pt, Ru-Ru, Ru-O) to fit the data with a model. For the fitting of the Pt/Ru alloy catalysts an fcc Pt structural model was imported from ATOMS, and few of the Pt atoms were randomly replaced with Ru. From the above structural model, FEFF paths were calculated, and the single scattering paths were used for EXAFS analysis. All the fits were done in R space with k^2 weighting. To get a reasonable comparison of the coordination numbers, the Debye-Waller (DW) factor was fixed at 0.005 and the amplitude reduction factor was set to 0.934 for Pt and to 0.916 for Ru, as reported in the literature [16].

5.2 Results and discussion

XRD investigations were carried out on powder samples from the MEA. The XRD patterns obtained for both anode and cathode were characteristic for that of an fcc Pt structure. For the different anode catalysts it was found that fcc Pt reflections were shifted to higher 2θ values strongly supporting an alloyed nature in the crystalline fraction of the catalyst [102]. XRD patterns obtained for various samples of both anode and cathode is shown in Figure 19 and Figure 20 respectively. The absence of any hcp Ru reflections in the pattern gave strong evidence for the absence of crystalline Ru particles [103].

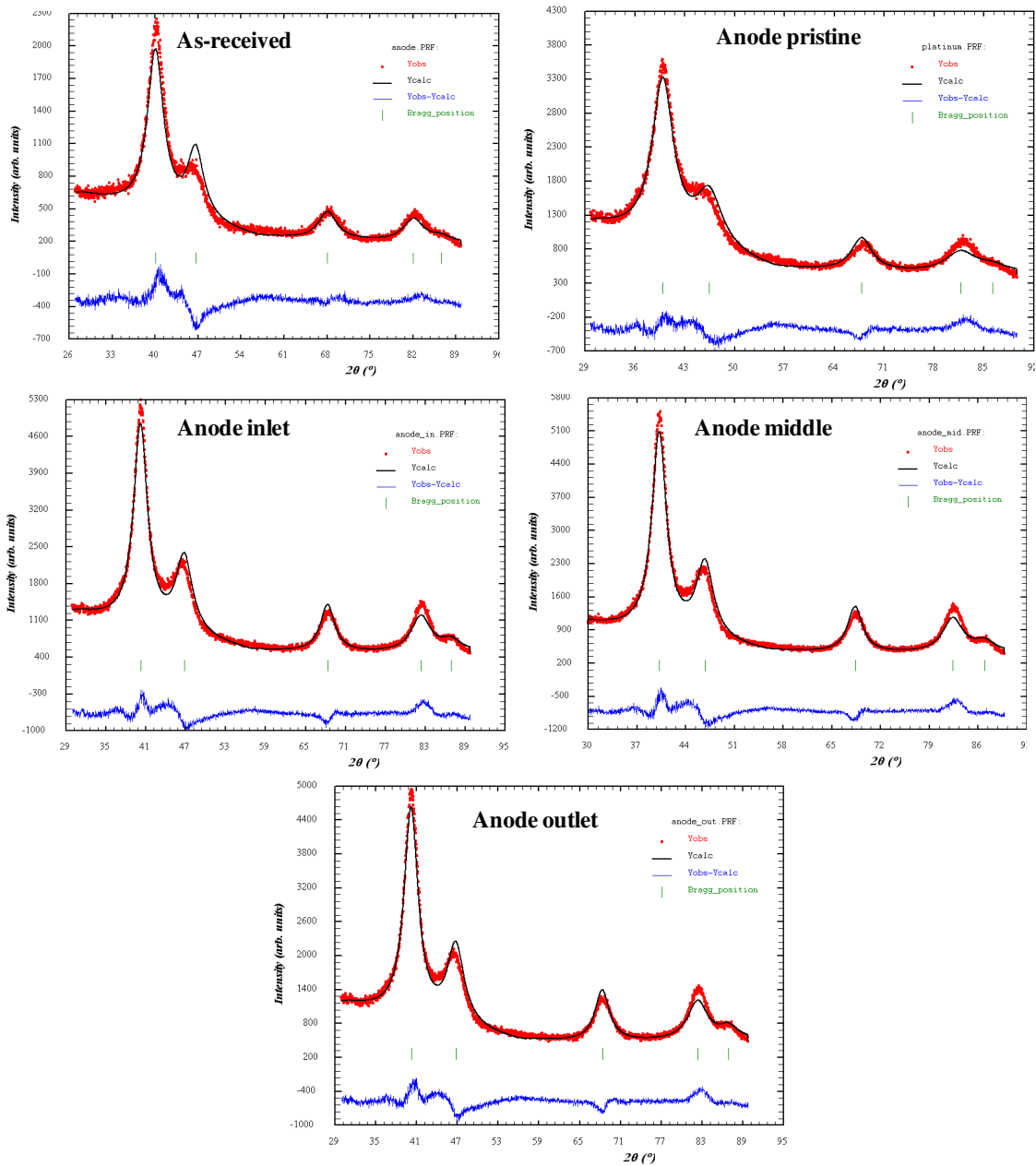


Figure 19: XRD patterns of the anode catalyst: as-received catalyst, pristine MEA, methanol inlet, anode middle, methanol outlet, No Ru reflection observed for different samples

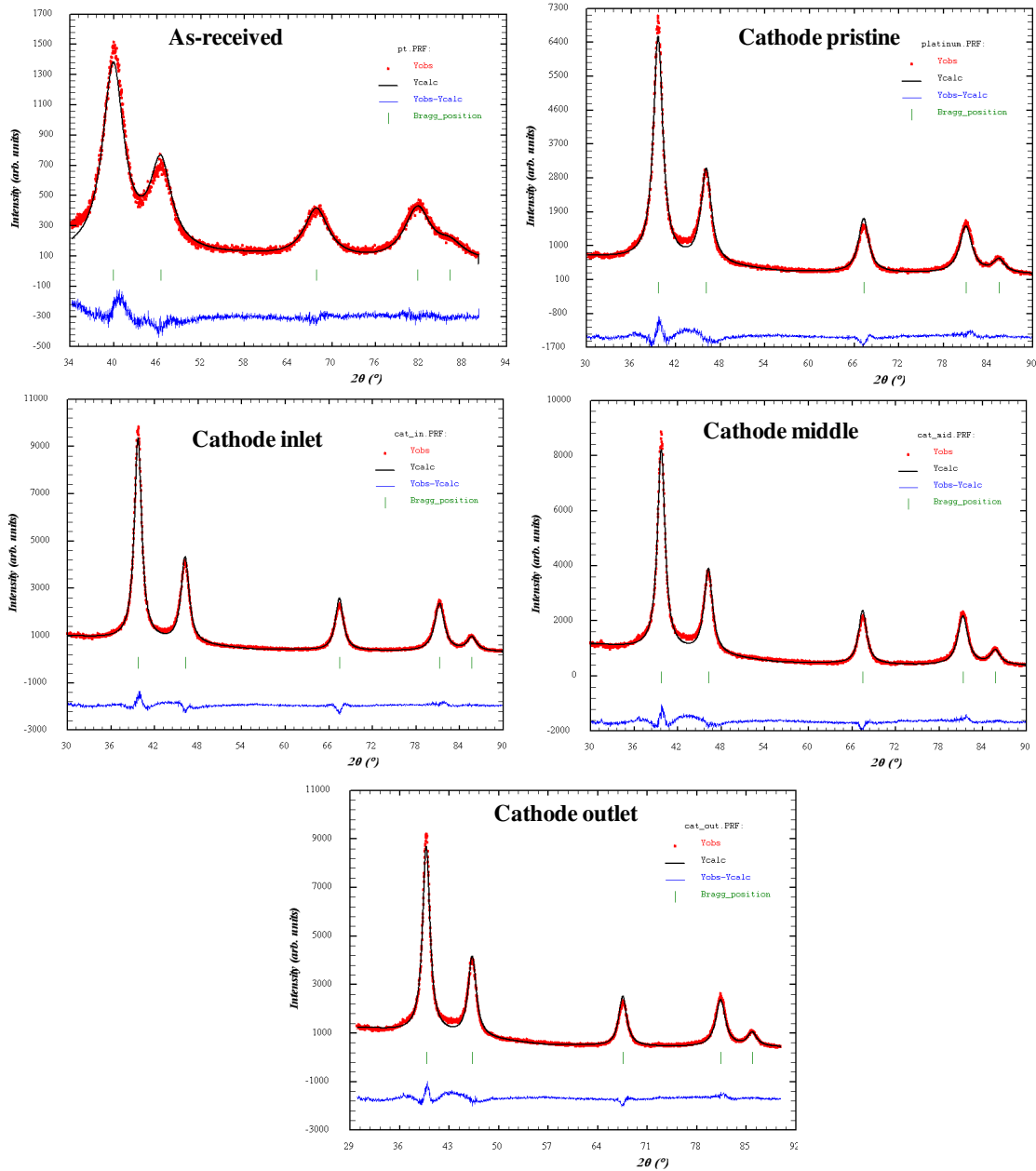


Figure 20: XRD patterns of the cathode catalyst: as-received catalyst, pristine MEA, oxygen inlet, cathode middle, oxygen outlet. Particle size is doubled by the MEA fabrication process, but no differences depending on cathode area were observed after operation.

Crystallite sizes obtained for various samples after Rietveld refinement are summarized in Table 5. It can be seen from Table 5 that the cathode catalyst had undergone particle growth (2 nm to 4 nm) during MEA fabrication, whereas no significant particle growth was observed for the anode. Although particle growth is expected during the sonication phase or in the hot pressing phase of the MEA fabrication, the pronounced particle growth in the cathode during MEA fabrication might be due to the following reason: As it will be discussed during the XAS analysis later, the anode catalyst contains both X-ray amorphous PtO₂ and RuO₂ phase (cannot be observed by XRD). It is proposed that RuO₂ is more difficult to reduce during the sample preparation compared to PtO₂. Further it has also been proposed by Song *et al.*, that the amorphous ruthenium oxide present in the sample may act as a dispersion agent and prevent particle growth at the anode side [104].

	<i>Particle size (nm)</i>	
	Anode	Cathode
As received	1.8	2.0
Pristine MEA	1.6	4.0
Inlet	2.3	5.2
Middle	2.3	5.2
Outlet	2.4	5.0

Table 5: Average particle sizes determined from XRD analysis using Scherrer's equation

It can also be seen from the Table that the aged anode catalyst showed a slight increase in the particle size, but no significant structural differences observed for the different electrode regions. Above all the alloyed nature of the nanoparticles was still pronounced even in the EOL sample. For the cathode catalyst, apart from the particle growth during the sample preparation, the particle size was also found to increase with fuel cell operation, but no significant difference in size was observed for the different regions. Similar to the aged anode the XRD patterns (Figure 20) of the aged cathode catalyst did not show any presence of a crystalline Ru phase caused by Ru dissolution from the anode and cross over to the cathode side. However, cross over Ru might be present in an X-ray amorphous state.

The XRD findings were further supported by the XAS studies and the results for both Ru edge and Pt L₃ edge EXAFS analysis are summarized in Table 6 and Table 7 respectively. Apart from giving information about the coordination number which is also related to particle size [105], EXAFS analysis also gave information about the amorphous Pt and Ru oxidic phase present in the catalyst. Fourier transform of the Ru K edge and Pt L₃ for the commercial anode catalyst powders, fresh MEAs and aged catalyst are shown in Figure 21 and Figure 22 respectively. The broad peaks between 1-2 Å are an indication of oxidation in the catalyst. It can be seen from Table 5 that no significant change in the total coordination number (sum of NPt-Pt, NPt-Ru and NPt-O) was observed for the as-received anode catalyst and the fresh MEA which strongly support XRD findings. The FT of both the Ru and Pt edges (Figure 21 and Figure 22) revealed a splitting in the peaks indicating the existence of a Pt/Ru alloy [106]. It can be assumed that due to the oxidized Ru present in the catalyst the Pt:Ru ratio greatly deviates from the expected 2:1, and now a random alloy is expected with a larger fraction of Pt.

Ru edge	NRu-Pt	rRu-Pt (Å)	E ₀ Ru-Pt (eV)	NRu-Ru	rRu-Ru (Å)	E ₀ Ru-Ru (eV)	NRu-O	rRu-O (Å)	E ₀ Ru-O (eV)
As-received	1.7	2.72	-7.42	1.6	2.66	-2.68	2.2	1.98	-2.80
Pristine MEA	1.7	2.72	-4.72	1.5	2.67	-2.07	2.1	1.98	-2.05
OCV	1.7	2.70	-8.17	2.4	2.65	-6.90	0.8	2.03	3.93
Inlet	2.8	2.72	-5.68	2.5	2.67	-4.54	1.4	1.99	-0.91
Middle	2.8	2.72	-2.49	2.2	2.65	-7.10	1.4	1.97	-0.87
Outlet	2.5	2.72	-5.30	2.2	2.67	-5.90	1.4	1.95	-3.12

Table 6: EXAFS analysis anode catalyst Ru K edge

Pt edge	NPt-Pt	rPt-Pt (Å)	E ₀ Pt-Pt (eV)	NPt-Ru	rPt-Ru (Å)	E ₀ Pt-Ru (eV)	NPt-O	rPt-O (Å)	E ₀ Pt-O (eV)
As-received	3.0	2.72	4.99	1.8	2.72	7.57	1.0	2.00	6.62
Pristine MEA	3.2	2.71	4.61	1.9	2.71	8.80	0.9	1.94	-0.61
Inlet	4.4	2.73	5.04	2.2	2.72	6.58	0.5	1.95	-0.55
Middle	4.4	2.73	4.61	2.2	2.72	7.00	0.5	1.99	2.11
Outlet	4.2	2.73	3.44	2.1	2.72	6.46	0.5	2.00	4.88

Table 7: EXAFS analysis anode catalyst Pt L₃ edge

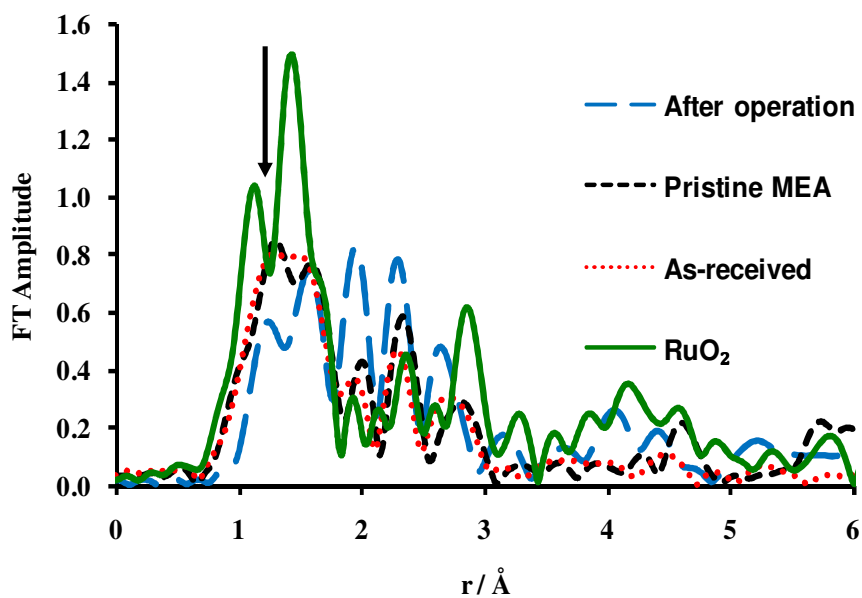


Figure 21: FT Ru K edge taken for the as-received Pt/Ru catalyst, pristine MEA, the catalyst after operation and a hydrous ruthenium oxide standard. Before operation, ruthenium appears to be largely oxidized.

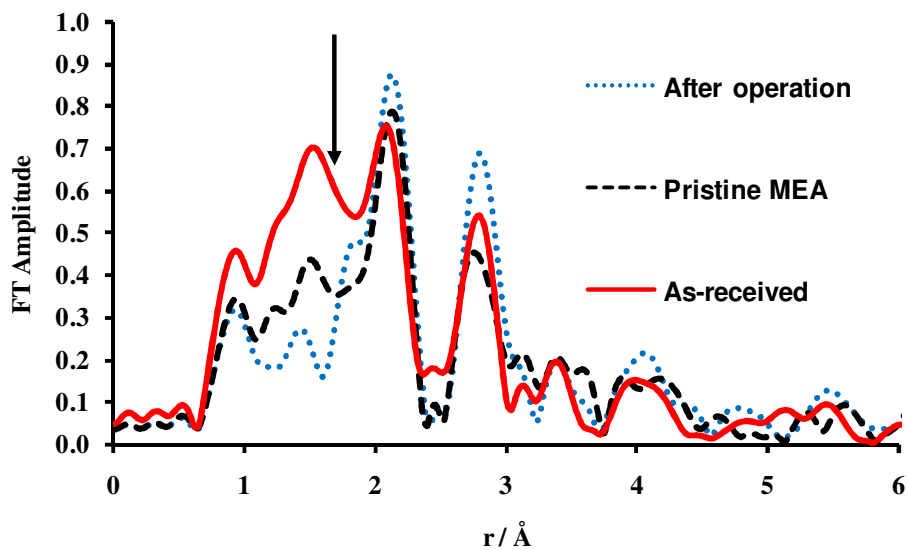


Figure 22: FT Pt L₃ edge taken for the as-received Pt/Ru catalyst, pristine MEA and the catalyst after operation

The EXAFS data may be interpreted based on the existence of 3 different ruthenium phases: Ru in a Pt-Ru alloy, Ru oxide and separate metallic Ru, both X-ray amorphous. It can be seen from the *in-situ* DMFC Ru K edge XAS measurements at open circuit potential (OCV) conditions that a significant amount of the ruthenium oxides becomes reduced ($N_{\text{Ru-O}}=2.2$ to 0.8) and probably forms metallic Ru (corresponding increase in $N_{\text{Ru-Ru}}$ (1.5 to 2.5)).

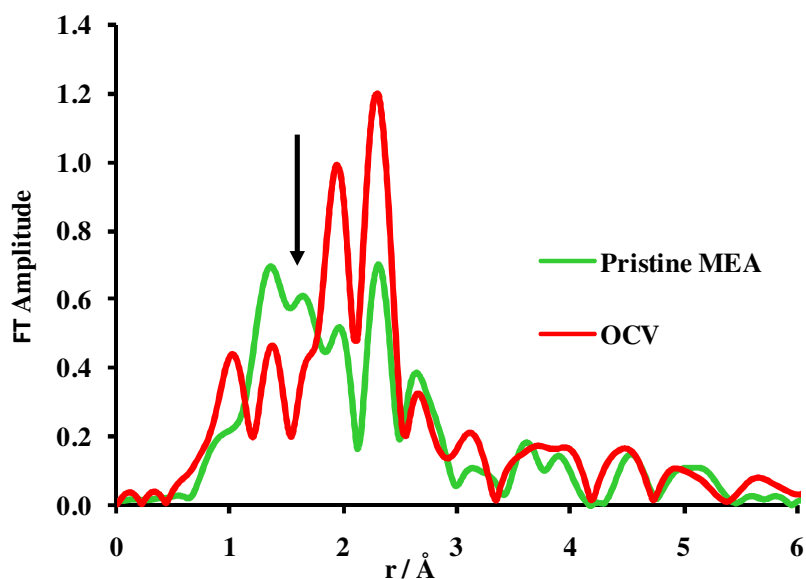


Figure 23: FT Ru K edge spectrum of the pristine MEA compared to the MEA during open circuit voltage (OCV) condition. At OCV, a significant fraction of the Ru oxides gets reduced.

The reduction of $N_{\text{Ru-O}}$ had no significant effect on the $N_{\text{Ru-Pt}}$, which means that the reduced oxide stays unalloyed. FT of the Ru K edge spectrum recorded under OCV condition is shown in Figure 23. It can be seen in the FT that there is an increase in the FT amplitude around 2.5 Å compared to the fresh catalyst. This might be due to reduction of some Ru oxides to metallic Ru which is schematically shown in Figure 24. It can be observed that the alloyed nature of the anode catalyst is maintained during the whole life time of the MEA, even after a significant fraction of metallic Ru was observed at the cathode (below). To account for the Ru observed at the cathode, it could be concluded that Ru is preferentially leached out from unalloyed Ru or the unreduced Ru oxides. The reduction and leaching of the oxide phase can bring alloyed particles together, and an overall increase in the particle size can be observed during operation.

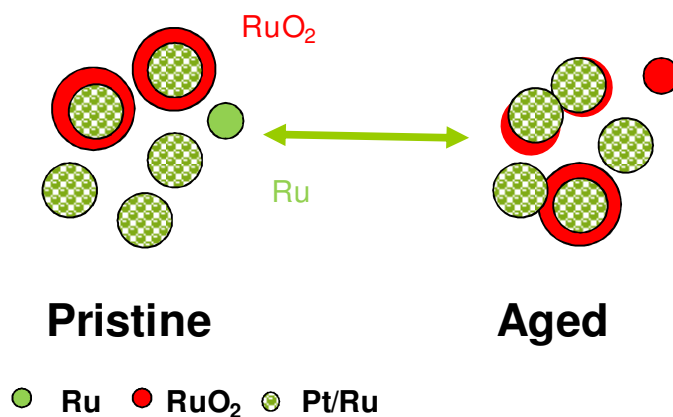


Figure 24: Schematic representation of structural changes in DMFC conditions

FT at the Pt and the Ru edge for the aged anode catalyst from different regions in the fuel cell are shown in Figure 25 and Figure 26 respectively. It can be seen that there is an overall increase in the FT amplitude for the aged catalyst compared to the pristine catalyst, which can also be correlated with particle growth. Further the nature of the ruthenium oxide can be interpreted from the $r_{\text{Ru-O}}$ bond distances (Table 7). XAS investigations by Rose *et al.* give a correlation of the bond distance ($r_{\text{Ru-O}}$) with the hydrous and anhydrous form of ruthenium oxide [107]. The Ru-O bond distance obtained from the EXAFS for the as-received catalyst and the catalyst in OCV condition showed a larger bond distance of $r_{\text{Ru-O}}=2.03 \text{ \AA}$. According to Ross *et al.* larger $r_{\text{Ru-O}}$ bond distances are assigned to hydrous ruthenium oxide which forms at relatively low potentials ($< 0.7 \text{ V}$). In contrast, EXAFS analysis of the aged sample revealed a much smaller $r_{\text{Ru-O}}$ bond distance for the methanol outlet in comparison to the inlet and middle regions. From the studies of Ross *et al.*, this smaller bond distance can be assigned to anhydrous ruthenium oxide, which occurs at relatively higher potentials (above 0.7 V). The preferential formation of anhydrous ruthenium oxide at the methanol outlet may be explained in the context of fuel starvation, which is expected to be severe at the methanol outlet [108]. During the fuel starvation process the electrochemical potential of the starved region can go above 0.9 V and at these high potentials the anhydrous form of ruthenium oxide is expected to be formed. It has been proposed by Rolison *et al.* that anhydrous ruthenium oxide is highly unfavorable for the fuel cell catalysis due to its low electron and proton conductivity [42], and thus methanol outlet regions might degrade and lose their activity faster than other regions.

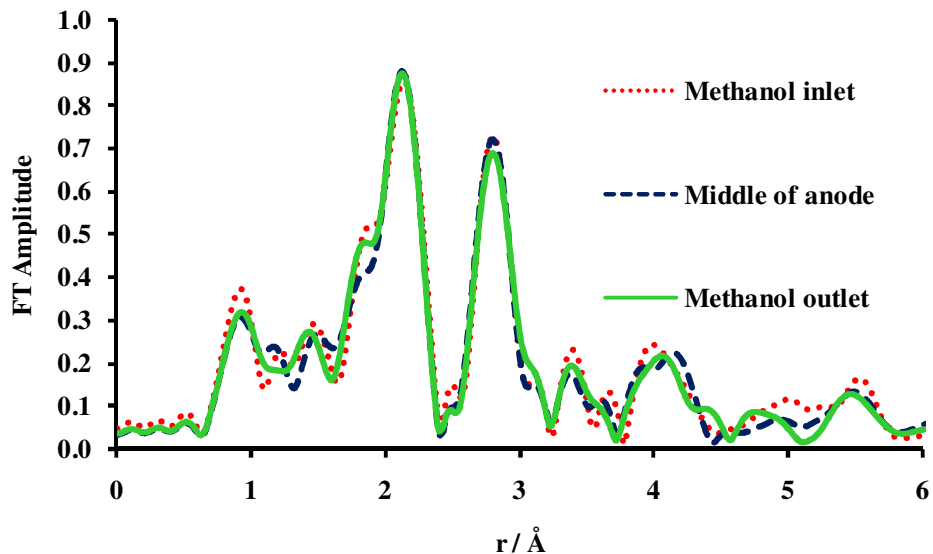


Figure 25: FT Pt L_3 edge of the anode side taken for the methanol inlet, middle and outlet regions.

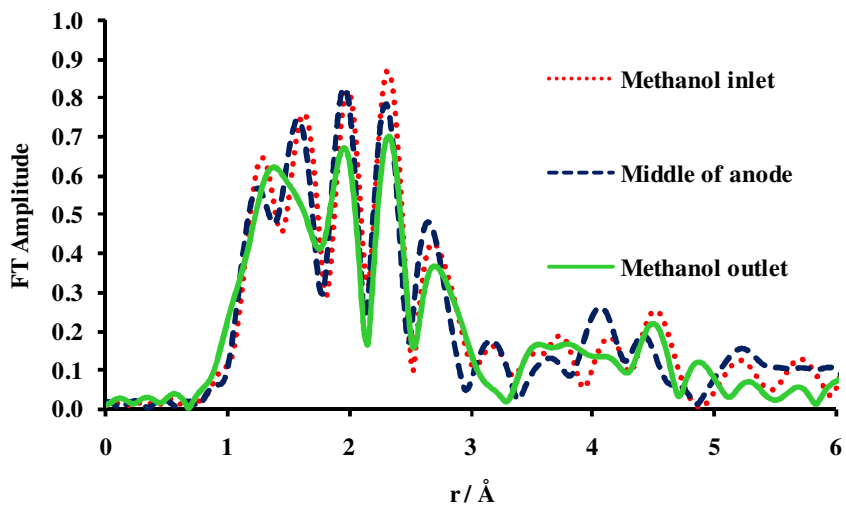


Figure 26: FT Ru K edge of the anode side taken for methanol inlet, middle and outlet regions. While the Pt edge does not show pronounced differences, at the Ru edge the catalyst at the methanol outlet is affected.

The Pt L_3 EXAFS investigation of the cathode catalyst also showed a significant fraction of oxidized Pt. The results of EXAFS analysis of the cathode catalyst are shown in Table 8. In contrast to the anode catalyst, a significant increase in the coordination number was observed during the MEA preparation. The overall increase in the particle size during MEA fabrication was also reflected in the large increase in FT amplitude observed for the fresh MEA which is seen in Figure 27. This finding also shows good agreement with the XRD results. Thus it may be concluded that unlike in the anode catalyst the Pt in the cathode catalyst is highly oxidized due to the absence of Ru and these oxidized fraction gets reduced during the MEA fabrication and leads to particle growth.

Pt edge	N_{Pt-Pt}	r_{Pt-Pt} (Å)	E₀Pt-Pt (eV)	N_{Pt-O}	r_{Pt-O} (Å)	E₀Pt-O (eV)
As-received	3.1	2.74	7.47	1.4	1.98	1.85
Pristine MEA	7.2	2.75	7.62	0.6	1.97	1.46
Inlet	8.1	2.75	5.48			
Middle	8.2	2.76	8.51			
Outlet	8.0	2.74	7.70			

Table 8: Pt L_3 edge EXAFS analysis of cathode catalyst

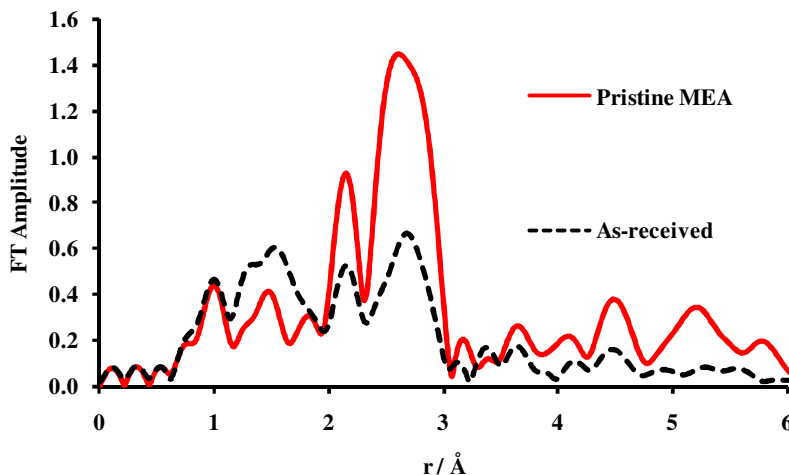


Figure 27: FT Pt L_3 edge of the cathode side- pristine MEA and as-received catalyst

Although an increase in the coordination number was seen with fuel cell operation, no significant difference in the structure or particle size was observed for the different regions. The FT obtained from various samples from different regions of the cathode is shown in Figure 28.

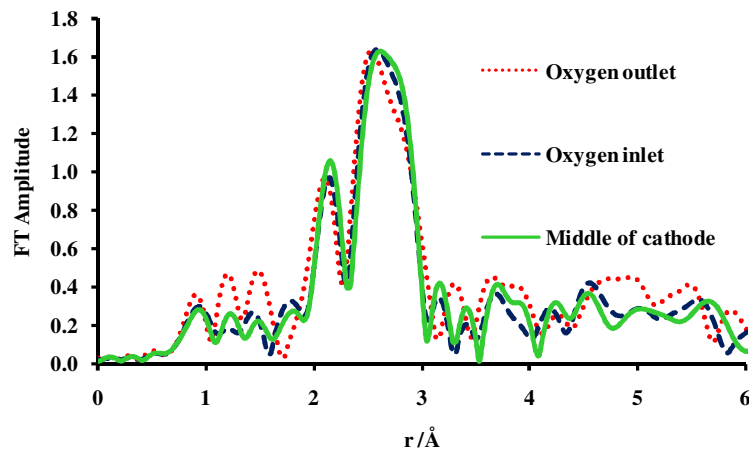


Figure 28: FT Pt L_3 edge of the cathode samples from different regions, i.e. oxygen inlet, middle and outlet. In good agreement with the XRD data, no site-dependent changes were observed.

Ru K edge measurements in fluorescence mode on the cathode catalyst from different regions of the DMFC stack gave XANES spectra identical to that of a ruthenium oxide standard. The XANES spectra of cathode catalyst at Ru K edge is shown in Figure 29. This result strongly supported the idea that cross over ruthenium from the anode gets dispersed everywhere in the cathode and is predominantly oxidized.

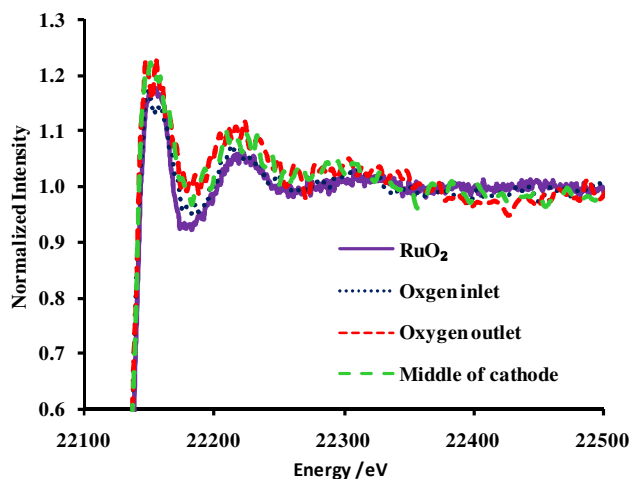


Figure 29: Ru K edge XANES spectra of the cathode catalyst. Near edge characteristics similar to a RuO_2 standard were found all over the cathode side of the MEA.

The Ru oxide has to be amorphous, however, since it was not detected by XRD. The crossover ruthenium can block the Pt sites for ORR and lead to fuel cell performance losses. Since the anode catalyst maintains its alloy nature it may be expected that the Ru crossover mainly take place from the dissolution of the Ru islands or the oxidized fraction in the anode.

In order to obtain more detailed information on the various degradation processes and whereabouts of the ruthenium in the whole electrode, MEA thin cuts from various regions were made and analyzed using TEM. Particle size distributions after ageing were obtained and are summarized in Figure 30.

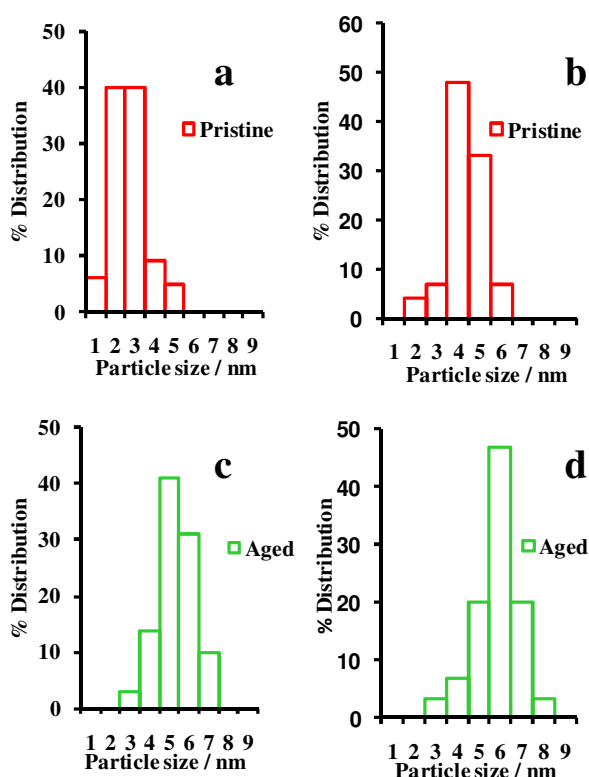


Figure 30: Particle size distribution from thin cut TEM analysis: (a) pristine MEA anode side, (b) pristine MEA cathode side, (c) aged MEA anode side, (d) aged MEA cathode side.

The particle sizes obtained from TEM analysis showed narrow size distributions for the both pristine anode and cathode catalyst. With ageing the distribution became slightly broader and shifted to higher values.

Compared to the XRD data, the average sizes by TEM analysis are slightly larger, since XRD is only sensitive to coherently scattering regions, i.e. crystalline parts. Nevertheless, the crystallite size from XRD was useful for the TEM investigation, as the anode and cathode sides of the MEA were distinguished by particle size and Ru content (EDX). TEM micrographs of the anode side of a pristine MEA showed that Pt/Ru particles predominantly assembled into chain-like structures, and had a distribution of particle sizes with a median value in the range of 2-3 nm. TEM micrographs of the pristine anode and the aged anode are shown in Figure 31. Information regarding the amorphous ruthenium oxide could not be obtained as it cannot be distinguished from the carbon support. The length and number of the chain-like ensembles of nanoparticles was found to increase with ageing, while a broader distribution of particle sizes with the median value shifted to 5 nm was observed.

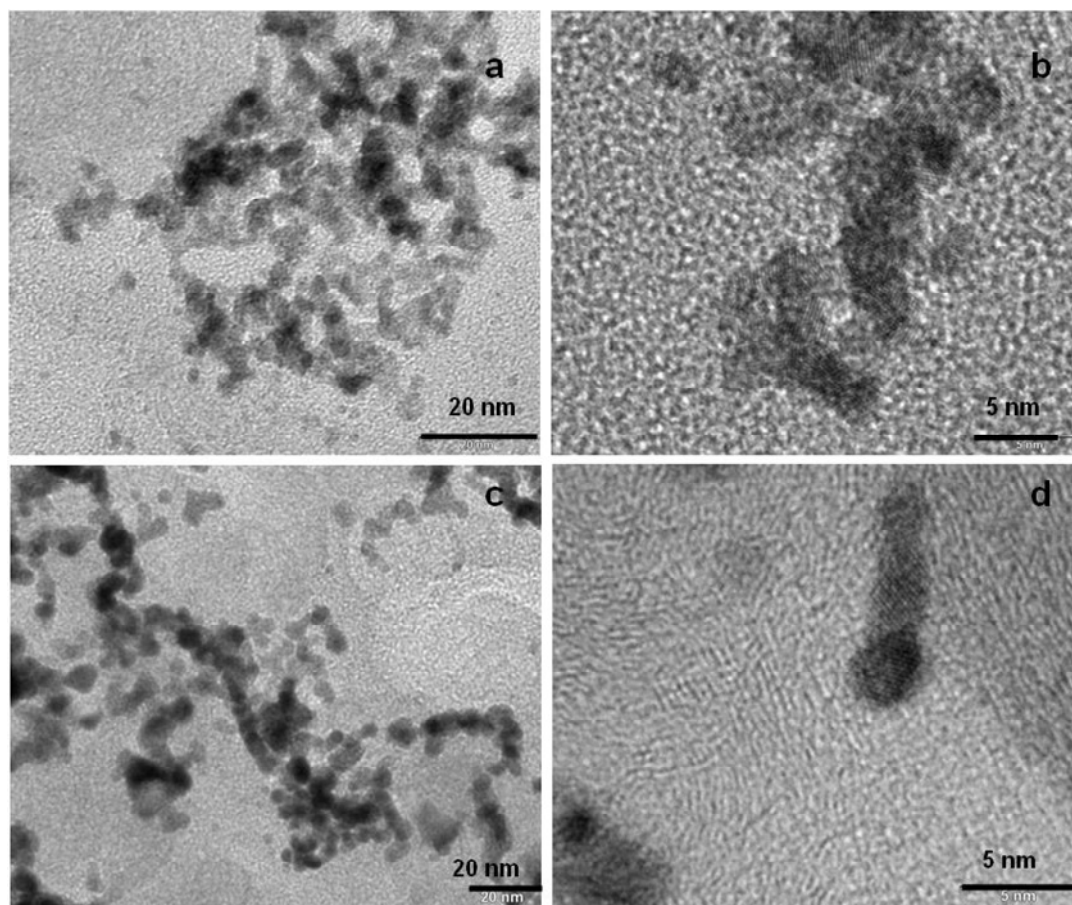


Figure 31: TEM thin cuts investigation of anode catalyst, a) & b) Pristine MEA low and high magnification, c) & d) aged anode low and high magnification. Chain like structure seen after ageing (c)

In contrast to the anode catalyst, TEM investigation of the pristine MEA cathode revealed a good dispersion of the catalyst with an average particle size of 4 to 5 nm. The ageing of the MEA causes these particles to form chains similar to those observed for the anode, and a broader distribution of particle sizes was observed (Figure 30, b and d). TEM micrographs of the pristine cathode and the aged cathode are shown in Figure 32. Severe aggregation was found all over the MEA after ageing, probably due to support corrosion (cathode) and dissolution of ruthenium oxide.

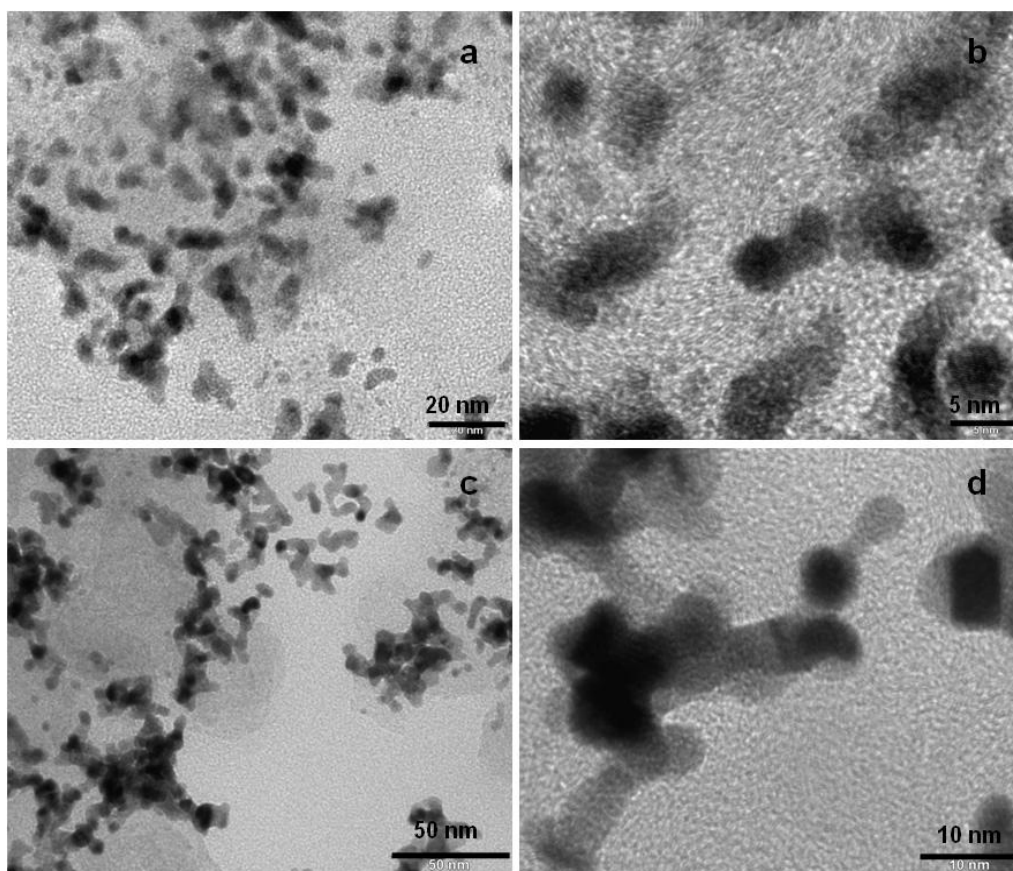


Figure 32: TEM thin cuts investigation of cathode catalyst, a) & b) Pristine MEA low and high magnification, c) & d) aged cathode low and high magnification.

Although particle size distributions from the different regions of the aged MEA looked similar, a more careful TEM investigation on the membrane electrode interface revealed some amorphous precipitation with particles as large as 1 μm , which are shown in Figure 33.

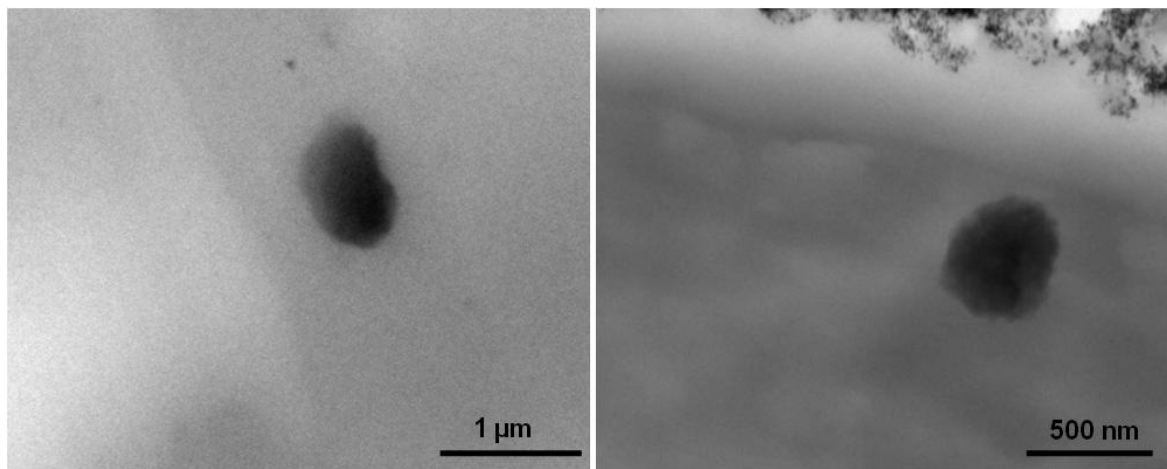


Figure 33: TEM images showing the amorphous precipitate in the Nafion membrane at the methanol outlet region.

These precipitates were only found for those samples from methanol outlet regions. To characterize them TEM EDX analysis was performed, but the high energetic electron beam destroyed the Nafion membrane making the TEM EDX nearly impossible. EDX analysis was repeated again with a similar set of sample, but with SEM, which uses a relatively low energy electron beam. EDX mapping on the whole surface of the MEA also gave an indication of the Pt and its distribution. The SEM and EDX mapping obtained for the anode of the pristine MEA are shown in Figure 34.

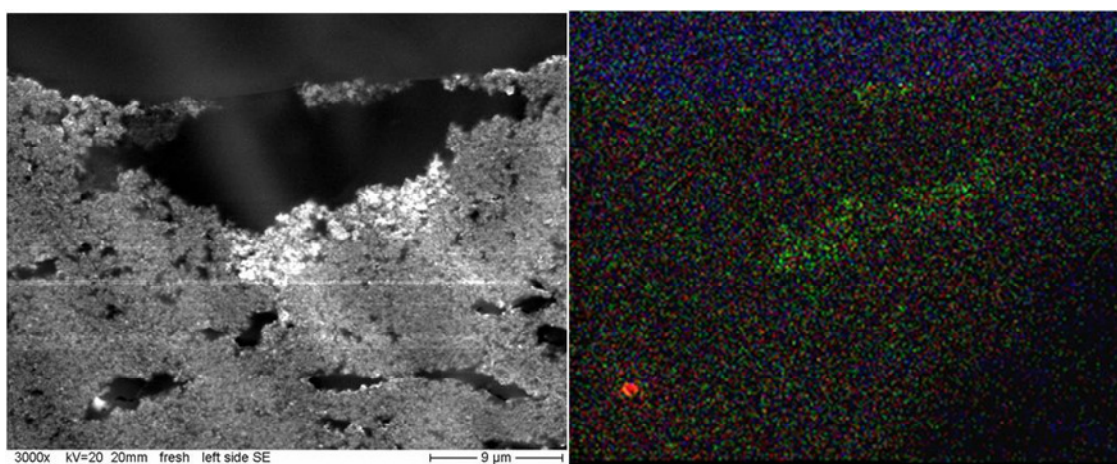


Figure 34: SEM image of anode of the pristine MEA (left), and EDX mapping of the corresponding area

EDX mapping gave an insight into the distribution of Pt and Ru in the electrode, which is represented as green and red color respectively. As it may be seen from the pristine anode both Pt and Ru is distributed uniformly, although large agglomerates of Ru could be seen. These agglomerates might be oxidized Ru, which is expected for the pristine MEA. However, the EDX Pt signals obtained for the anode were much weaker than for the cathode, which might be due to the reduced Pt content. The EDX mapping of the pristine cathode MEA is shown in Figure 35. Apart from the Pt and Ru, carbon support and fluorine in Nafion is also EDX mapped in black and blue color, respectively. The EDX mapping showed good dispersion of Pt for the pristine cathode electrode.

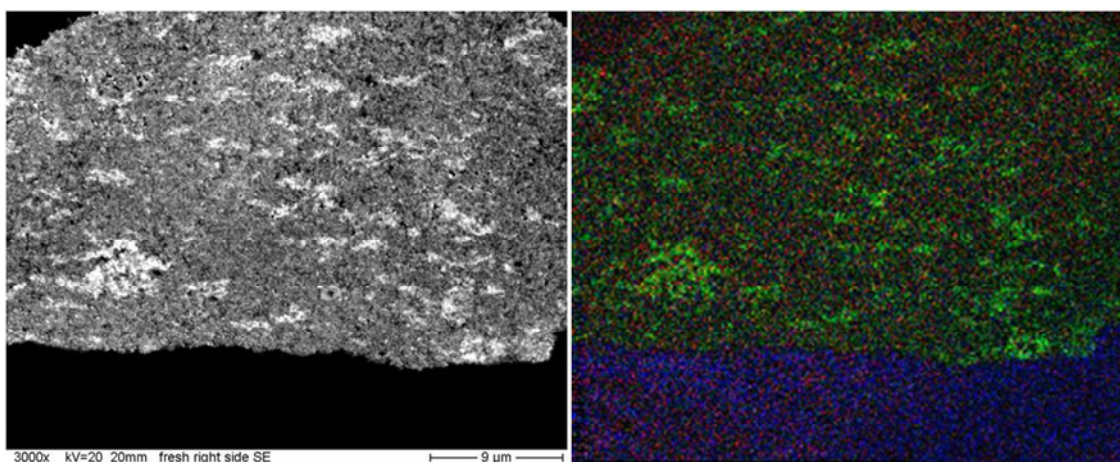


Figure 35: SEM image of cathode of the pristine MEA (left), and EDX mapping of the corresponding area

Analysis of the aged MEA, especially the anode side of the methanol inlet regions, showed the presence of large aggregates of Ru in the membrane. The EDX mapping of the aged anode is shown in Figure 36. This finding is in good agreement with the TEM results, where a similar set of samples also showed precipitates in the membrane. The preferential formation of these precipitates on the methanol outlet may be explained in the context of fuel starvation. It may be assumed that during a DMFC stack operation methanol concentration might decrease from inlet to outlet and thus methanol outlet regions can often encounter methanol starvation. During a fuel starvation event, especially in a fuel cell stack, cell reversal can occur as the fuel starved region takes the current produced from the non-starved region. This may lead to severe anode degradation especially in the form of Ru dissolution, which can get precipitated in the membrane [56].

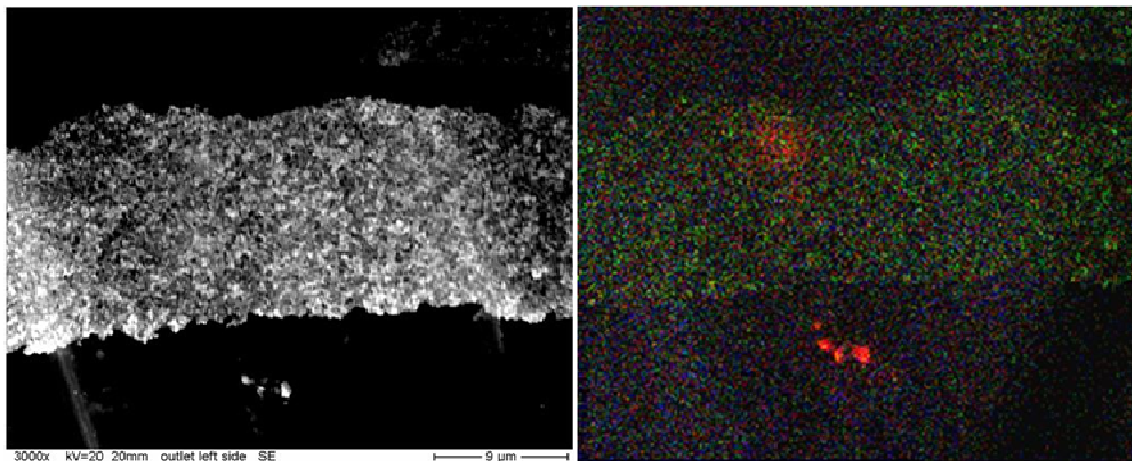


Figure 36: SEM image of anode of the methanol outlet (left), and EDX mapping of the corresponding area

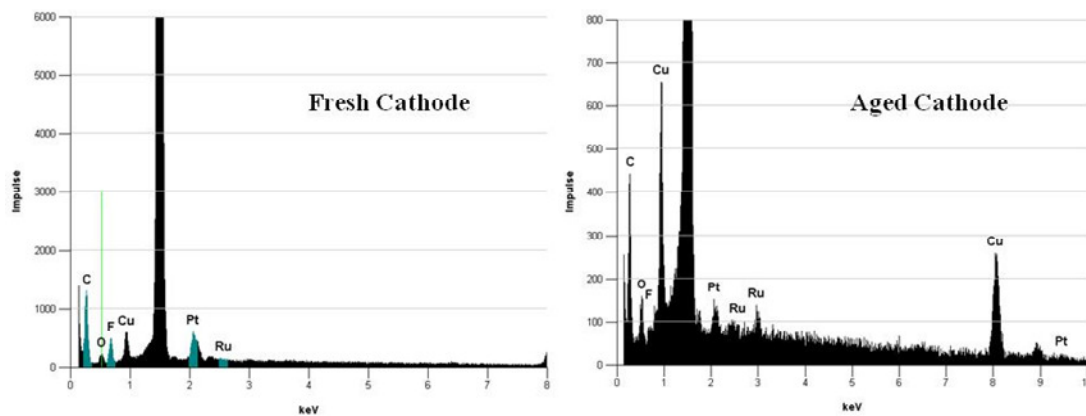


Figure 37: EDX spectra obtained for cathode of the fresh MEA and aged MEA

The EDX spectra on the cathode of the aged MEA showed the presence of Ru strongly supporting Ru cross over. The EDX spectra obtained for the cathode of pristine MEA and aged are shown in Figure 37. EDX mapping also gave evidence of the presence of cross over Ru in the cathode.

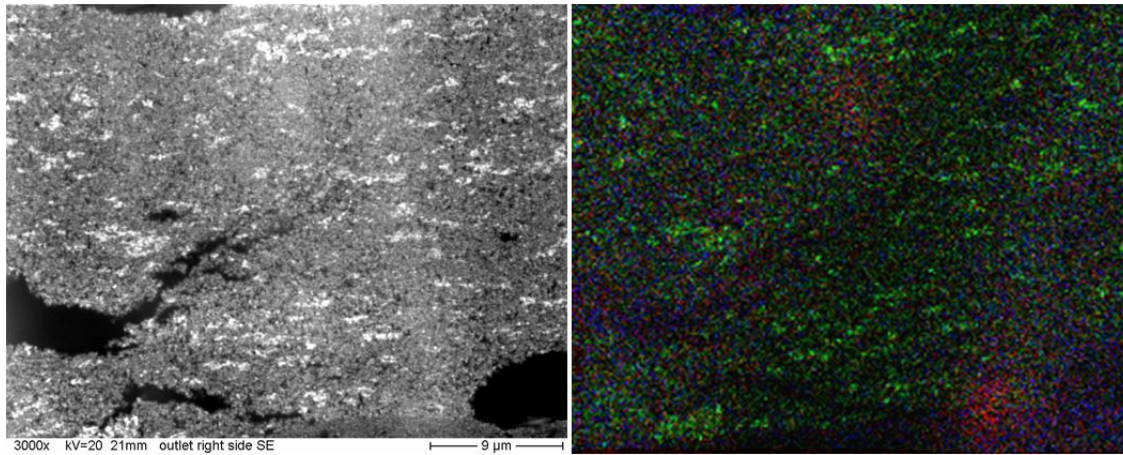


Figure 38: SEM image of cathode of the methanol inlet (left), and EDX mapping of the corresponding area

In conclusion, by combining various analytical techniques like XRD, XAS, and TEM detailed characterization of both fresh and aged MEA has been accomplished. Spatially resolved *ex-situ* studies provided new insight into degradation pattern of a DMFC stack and identified the methanol outlet region as most prone towards degradation.

6 Spatially resolved, in operando XAS studies in a DMFC

In this chapter, XAS is employed to study the spatial distribution of adsorbates in an operating fuel cell under high and low oxygen flow rate. XAS spectra are recorded at different regions of the anode (methanol inlet, middle, and outlet) and cathode (oxygen inlet, middle, and outlet). The adsorbates and their coverage were estimated from the $\Delta\mu$ XANES technique and the obtained results are correlated to the fuel distribution (concentration of methanol, cross over etc.), estimated anode and cathode electrode potential and to the extent of migration of H^+ ions from anode to cathode or vice versa. Finally, spatially resolved XAS measurements were done during methanol starvation and the degradation process was studied with EXAFS.

6.1 Experimental

The MEA preparation and the design of the fuel cell were explained in the previous chapters. The DMFC was operated with a portable commercial test bench from Magnum GmbH, Germany, equipped with mass flow controllers, heating device and electrical load etc. In a typical DMFC single cell operation, 3 ml of 1 M preheated methanol at 90°C was introduced into the anode side from the bottom of the fuel cell. The oxygen supply of the cathode was maintained at a flow rate of 150 ml/min for a high oxygen flow and 20 ml/min for a low oxygen flow. The cell was externally heated to 60°C and maintained at this temperature throughout the measurements. The DMFC was operated in a potentiostatic mode and *in-situ* XAS spectra were recorded at several cell voltages for both modes of experiment (high and low oxygen flow). The DMFC was also operated in fuel starvation mode, where the cell was run in chronopotentiometric mode at 600 mA. The fuel starvation was induced by switching off the methanol flow with the cell working in chronopotentiometric mode. After 15 minutes the methanol flow was resumed and polarization curve was recorded. The above cycle was repeated until the cell was degraded completely. *In-situ* as well as *ex-situ* XAS spectra were recorded at both Pt L_3 edge and Ru K edge during the fuel starvation process and after.

Details of the *in-situ* XAS setup are described in the previous chapters. All the spectra were recorded in QEXAFS fluorescence mode and a non energy resolved PIPS diode was used to collect the fluorescence signals. The *in-situ* cell was placed in between the two ionization chambers (I_0 and I_1) perpendicular to the PIPS diode and at an angle of 45° to the incident beam. The *in-situ* fuel cell set up is shown in Figure 39.

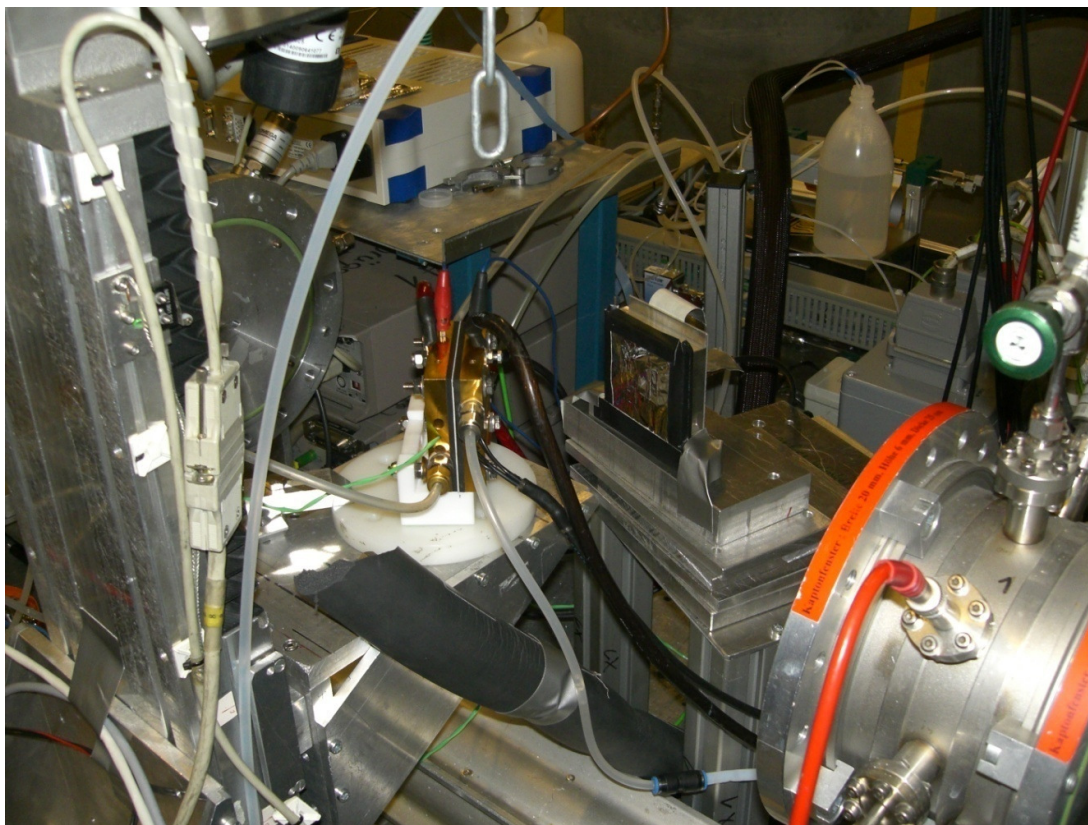


Figure 39: Spatially resolved *in-situ* DMFC XAS set up at beamline X1 HASYLAB

6.1.1 $\Delta\mu$ -XANES technique

The IFEFFIT (Version 1.2.11 IFEFFIT Copyright, Mathew Newville, University of Chicago, <http://cars9.uchicago.edu/ifeffit>) XAS analysis software was used for the $\Delta\mu$ -XANES analysis including the background subtraction (AUTOBK algorithm) and normalization. Since the present studies involve multiple QEXAFS spectra, for the processing of the XANES analysis each set of data (measured at the same potential) was normalized (25 to 150 above the edge). The normalized data set was then aligned with one of the reference foils from the set. This step is essential, as between two successive QEXAFS scans the beam may drift due to a fast

moving monochromator. The aligned data set was then merged. These steps were repeated for all data sets and then various merged data sets obtained were further aligned to one of the reference foils. The alignment is usually carried on the different reference foil spectra, which are simultaneously collected with the sample data (electrode at different potential). The energy correction on the reference foil is then automatically transferred to the sample spectra as well. The $\Delta\mu$ signatures are obtained by subtracting the μ of a selected potential as reference, according to equation 11 (chapter 3).

As explained in the previous section the criteria for choosing the reference potential are to use the one at which the electrode surface is the cleanest and has the least amount of adsorbates on it. In the literature, a potential around 0.54 V RHE (water activation, neither H nor O is present on the surface) in water or in the absence of methanol was chosen as the reference potential. However, in an operating fuel cell the above mentioned condition is difficult to achieve. So in the present study for the anode, XAS spectra taken after fuel cell operation were utilized as reference spectra. For the cathode, spectra taken at the highest current (lowest cell potential) was taken as the reference for the low oxygen measurement. However, under high O₂ flow, potential which gave a “positive” signature was chosen, i.e. that potential which gave a $\Delta\mu$ signature of the representative adsorbate. To identify the different experimental $\Delta\mu$ signatures representing the adsorbates, theoretical $\Delta\mu$ signatures are calculated using the FEFF 8.0 code as explained in section 3.1.2. The M-M bond distances (M=Pt, Ru) used in FEFF 8.0 were 2.75 Å, M-C=1.85 Å, C-O=1.0 Å, O-H=1.0 Å, and M-O=2.0 Å. The theoretical $\Delta\mu$ signatures are usually shifted by 1-5 eV and scaled by a multiplication factor for the ultimate comparison with experimental data. Distinguishing features at a particular energy is often chosen to differentiate different adsorbates which can be present simultaneously on the surface (e.g. CO and OH, CO and H₂O or methanol etc.).

6.1.2 EXAFS analysis

To investigate the structural changes occurring during the fuel starvation process EXAFS analysis was done on the fuel starved sample. EXAFS analysis was done using the IFEFFIT suite. All the data reduction procedures were carried out using the Athena software and FT fitting was carried out with Artemis. EXAFS analysis was carried out at both Pt L₃ edge and Ru K edge simultaneously by keeping the DW factor constant at 0.005 for both edges. The distance $r_{\text{Ru-Pt}}$ and $r_{\text{Pt-Ru}}$ were also constrained for both edges.

6.2 Results and discussion

For a better understanding of the $\Delta\mu$ results it is necessary to differentiate the anodic and cathodic potential of the DMFC from cell voltage. For this, estimated cathodic and anodic potentials in a DMFC cell with respect to the current are plotted in Figure 40. It must be emphasized that these curves are just qualitative. Understanding the cathodic and anodic potential is important, as it greatly helps to understand the adsorbate coverage data. For e.g. the potential at the anode determines when water activation or methanol oxidation to CO occurs, and more specifically, when water activation occurs on or near the Ru islands or away. It may be assumed that, when the current increases, the anode potential increases and a corresponding decrease in the cathode potential is observed. However, these changes also depend greatly on the methanol and O_2 flow rate. Also the plot assumes that the current density is relatively uniform over the area of the electrode, which is a reasonably good assumption at high O_2 flow rate, but not true for low flow rates, as will be discussed later.

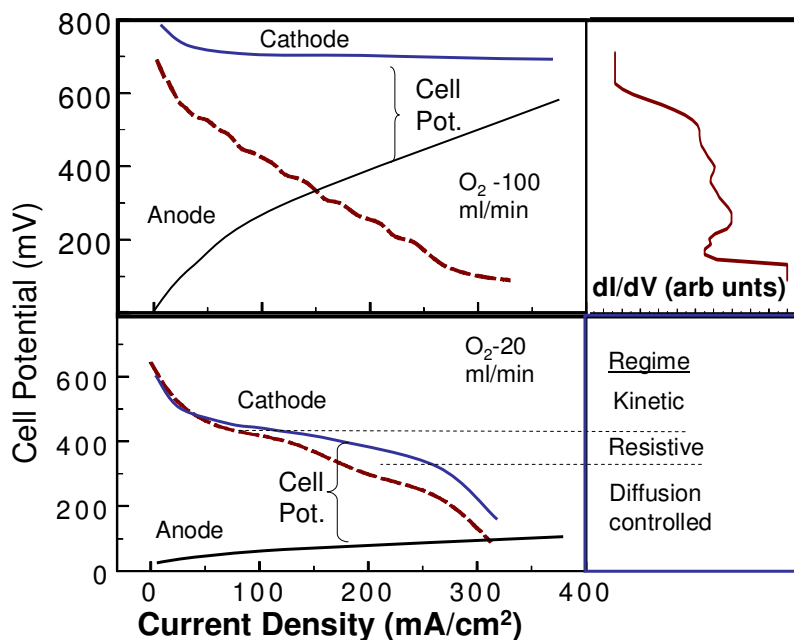


Figure 40: Estimated cathodic and anodic potential for a DMFC at high and low oxygen flow

The extent of increase in the anode potential over the cell voltage range is determined in part by the extent of the cathode potential decrease over the same range. In an H_2 fuel cell the cell potential decreases with current primarily because of the cathode potential drop, since the kinetics of HOR at the anode are so fast. A similar situation may be expected in the case of a

DMFC at low O₂ flow rate, when the different regimes (kinetic, resistive, and diffusion limitations) dominate at the cathode. However, in the DMFC with high O₂ flow rate, it is anticipated that the largest fraction of the potential loss with current occurs at the anode, because now the kinetics of the MOR and resulting CO poisoning, make the process much slower than the ORR.

6.2.1 High O₂ flow results (Anode)

The $\Delta\mu$ analysis results for the methanol inlet region of the anode are plotted in Figure 41. The results are compared with both experimental and theoretical results (FEFF 8) previously published by Scott *et al.* [41]. It must be emphasized that the present data is not resolved as that of Scott *et al.* as the present study was carried out in a real fuel cell which has a higher Pt loading, hence much smaller $\Delta\mu$ magnitudes. Moreover, the resolution of the measurements is limited by the QEXAFS mode of the measurements, which also adds noise in the data. For removing this noise, smoothing has done on this data which broadens out the features.

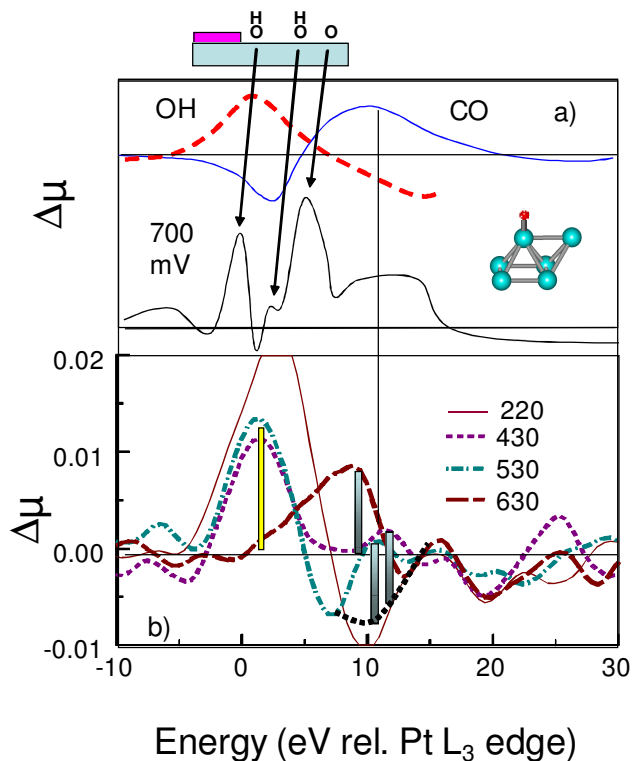


Figure 41: $\Delta\mu$ signature obtained for the methanol inlet region (bottom). Theoretical (red and blue) and experimental $\Delta\mu$ signature from the literature (top)

Notably three different OH signatures (OH near Ru islands, far Ru and at Pt) observed in the study of Scott *et al.* are now merged to one prominent OH signature. CO signature results obtained for the present study are quite comparable to published results, although OH signatures were also present at low anode potential (high cell voltage). The shaded rectangle shows the region chosen for determining the $\Delta\mu$ magnitude. $\Delta\mu$ signatures obtained for various regions of anode and cathode under different cell voltage is shown in Figure 42. The experimental data at 630 mV does not suggest any O(H) feature at 3 eV, so the $|\Delta\mu|_{\text{CO}}$ magnitude is straightforwardly given from the zero axis. However, at 530 and 430 mV, significant O(H) is present, as indicated by the large positive feature at 3 eV, and such O(H) would produce a large negative component in the 4-15 eV region (this is estimated by the black dashed line in Figure 41)

$\Delta\mu$ magnitude plots obtained for the different anode windows as a function of potential are shown in Figure 43. These results are again compared with electrochemical results from Scott *et al.* using Pt₃Ru catalyst [41]. It can be seen in Figure 43 especially for the methanol inlet three distinctive potential regions for the methanol oxidation process emerge. These regions are assigned to different methanol oxidation mechanisms occurring around these potentials, primarily, direct mechanism (D, higher anodic potential), direct ligand (DL intermediate potential) and bi-functional mechanism (BF low potential). These results are in good agreement with Scott *et al.* findings which further emphasize that the estimated potentials are quite reasonable. The CO magnitude at the anode middle and outlet region reflects the effect of methanol concentration, which tends to decrease from inlet to outlet. It can be seen that in the middle region CO is found only in the DL regions, suggesting that the BF mechanism is totally able to keep the additional CO coming on at lower anode potentials from ever forming because of the lower methanol concentration. Further going to the methanol outlet regions no built up of CO is evident suggesting a much lower methanol concentration there. It is interesting to see that OH adsorption at the anode correlates to the CO adsorption ie, CO adsorption decreases where the OH adsorption increases, which is actually expected, although the individual OH contributions coming from that near and distant Ru are not resolved. The OH adsorption occurring at different anode potentials can be correlated to the Ru islands near and far from Pt. It may be expected that OH adsorption at lower cell potentials takes place from Ru islands and at higher potential from near or far Ru islands. This is indicated in the Figure 43 by dashed line for BF mechanism and solid line for DL and D mechanism.

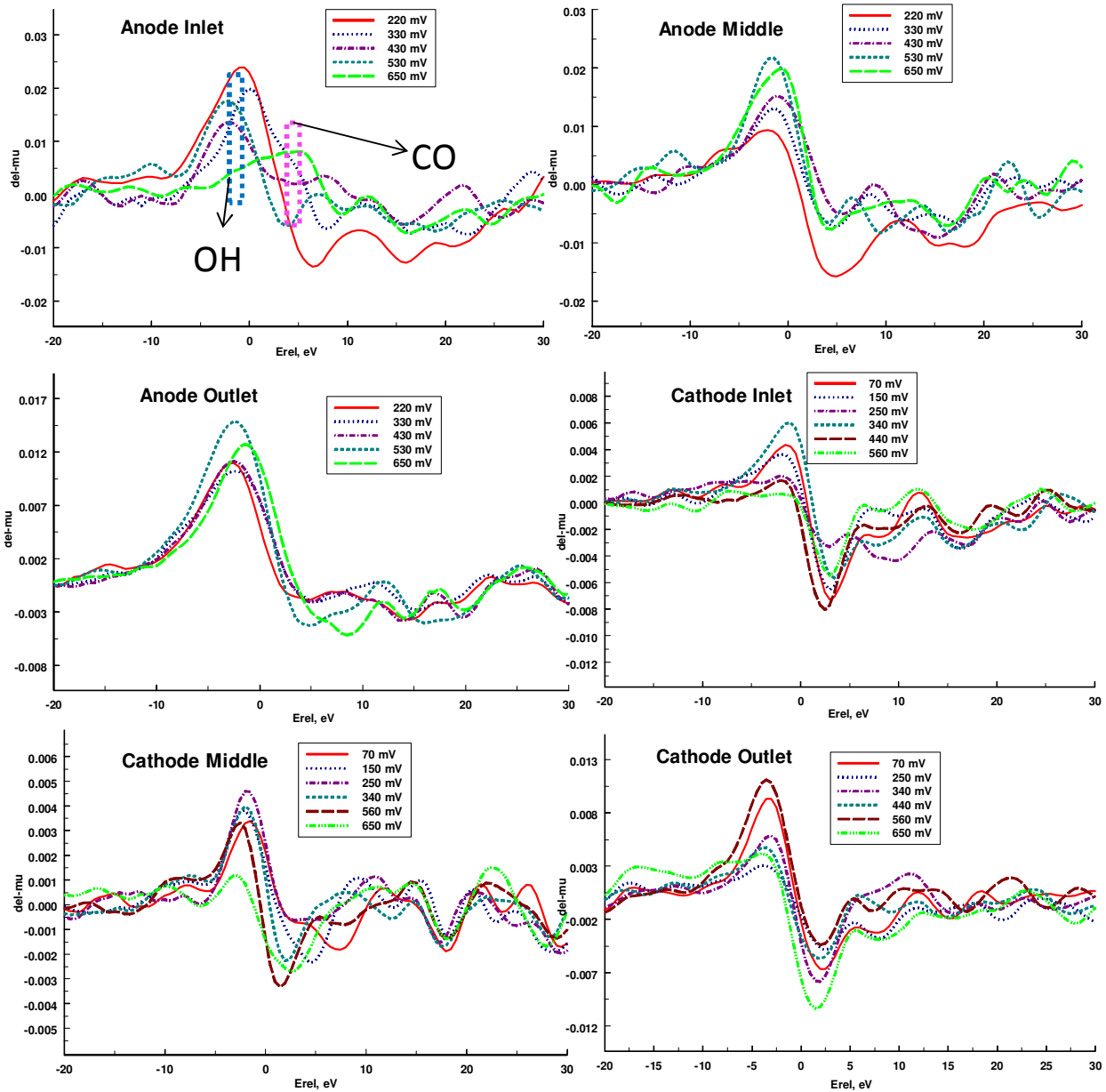


Figure 42: $\Delta\mu$ signatures: different regions of anode and cathode under different cell voltages (not smoothed)

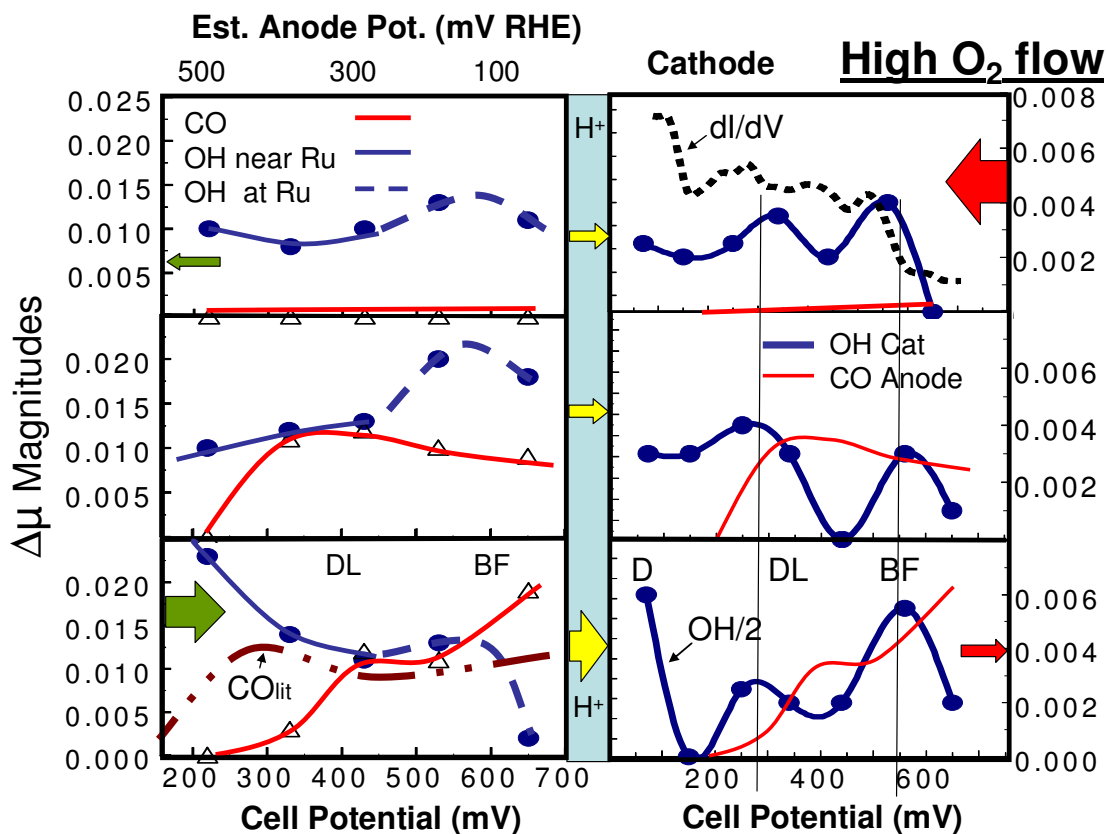


Figure 43: $\Delta\mu$ magnitude for both anode (left) and cathode (right) from different regions plotted against the cell voltage (the estimated cell potential indicated at the top).

6.2.2 High O₂ flow results (Cathode)

The $\Delta\mu$ magnitude obtained for the cathode is plotted on the right side of the Figure 43. These results are discussed in the context of ORR and importance of H⁺ on ORR. The kinetic equations derived from the double-trap kinetic model of Wang *et al.* [109] for the 4-e ORR in acidic media are explained below,



The above reactions can be summarized as below



According to Wang *et al.* the RA mechanism dominates at potentials below 700 mV, thus adsorbed intermediate as well as H⁺ play a significant role in the ORR. The cathode result (Figure 43, right) suggests that the OH coverage on the cathode correlates to the magnitude of the current flow i.e., it increases, as the current flow increases, or as the availability of H⁺ coming across the Nafion membrane increases, because they should be proportional to each other. However, the current (electron) is collected from all points on the fuel cell anode, but the H⁺ comes across the PEM from the anode and should directly be reflected in what goes on at the cathode at the same window or observation point. This is particularly true if we think of the fuel cell as segments connected in parallel as assumed previously by Sauer *et al.* The cathode result (Figure 43, right) suggests a “cross-talk” of H⁺ transfer from anode to cathode. The OH adsorption reflected in the $\Delta\mu$ magnitude shows two maxima, with that at the bottom showing an additional feature at very low cell potential. To show that OH adsorption tracks with the MOR going on at the anode, the CO coverage on the anode is plotted over the cathode results. Careful inspection reveals that the OH coverage on the cathode peaks just as the CO coverage on the anode drops, exactly as one would expect, since the current and H⁺ yield are

able to increase as the CO coverage drops. Thus, the 3 features in the OH coverage on the cathode can be correlated with the 3 different CO oxidation mechanisms identified in the anode; namely the BF, DL, and D mechanisms named for the different sources of OH, which oxidizes the CO. The “cross-talk” of H⁺ transfer is also evident from the magnitudes of the OH cathode coverage. Note that the magnitude of OH coverage on the cathode bottom has been divided by two. Therefore, the largest current occurs at the bottom near the point of the methanol inlet, as would be expected. It is interesting that the magnitude of the OH coverage is similar at the middle and top observation windows, suggesting that the current flow is similar at these two points.

Finally, if the cathode OH coverage is indeed tracking with the H⁺ cross-talk from the anode, the total current, although an integral of the current from each point on the electrodes, should track with the cell potential. To show this, the derivative of the current with potential (dI/dV) is plotted at the top of Figure 43. Again the features in this derivative fall at remarkably similar positions as the maxima in the cathode OH coverages. Note that two maxima in dI/dV fall in the DL region, but this is entirely consistent with the shift in the OH coverage at the top window vs. the middle and bottom windows. Thus the current appears to reflect all maxima in the OH coverage, one D, two DL, and the BF features.

6.2.3 Low O₂ flow results

The $\Delta\mu$ signatures obtained for the lower 20 mL/min O₂ flow rate are shown in Figure 44. Similar to the high oxygen flow, the $\Delta\mu$ magnitude obtained are plotted against the cell voltage or to the estimated potential in Figure 45. In order to understand the change in adsorbate coverages in this case, the expected changing anode and cathode potentials are illustrated as done before in Figure 43. As suggested in the earlier discussion of Figure 43, the cathode potential will now decrease more rapidly with cell potential, and consequently the anode potential increases less. This change is expected to vary with different window positions as different regions now experience different O₂ concentration. As modeled by Sauer et al, it is assumed that the different paths or windows (top, middle, and bottom) of the electrode are connected in parallel, and because of the highly conducting end plates, the potential drop across each path is $V_{\text{int}} = V_{\text{open}} - V_{\text{cell}} = V_c + V_a$, where the potentials are denoted with subscripts (int = internal IR drop, open = open circuit, cell = measured cell, a = anode and c = cathode) and the internal IR drop consists of the sum of that at the anode and cathode. As the oxygen concentration decreases going from the top to the bottom window, the cathode potential will decrease faster with cell potential, because the O₂ diffusion limit is reached at

smaller currents (higher potential). The expected local adsorbate coverage on the anode and cathode at the estimated local potential are shown in Figure 46. The anode and cathode potentials are conveniently drawn linear with respect to cell potential.

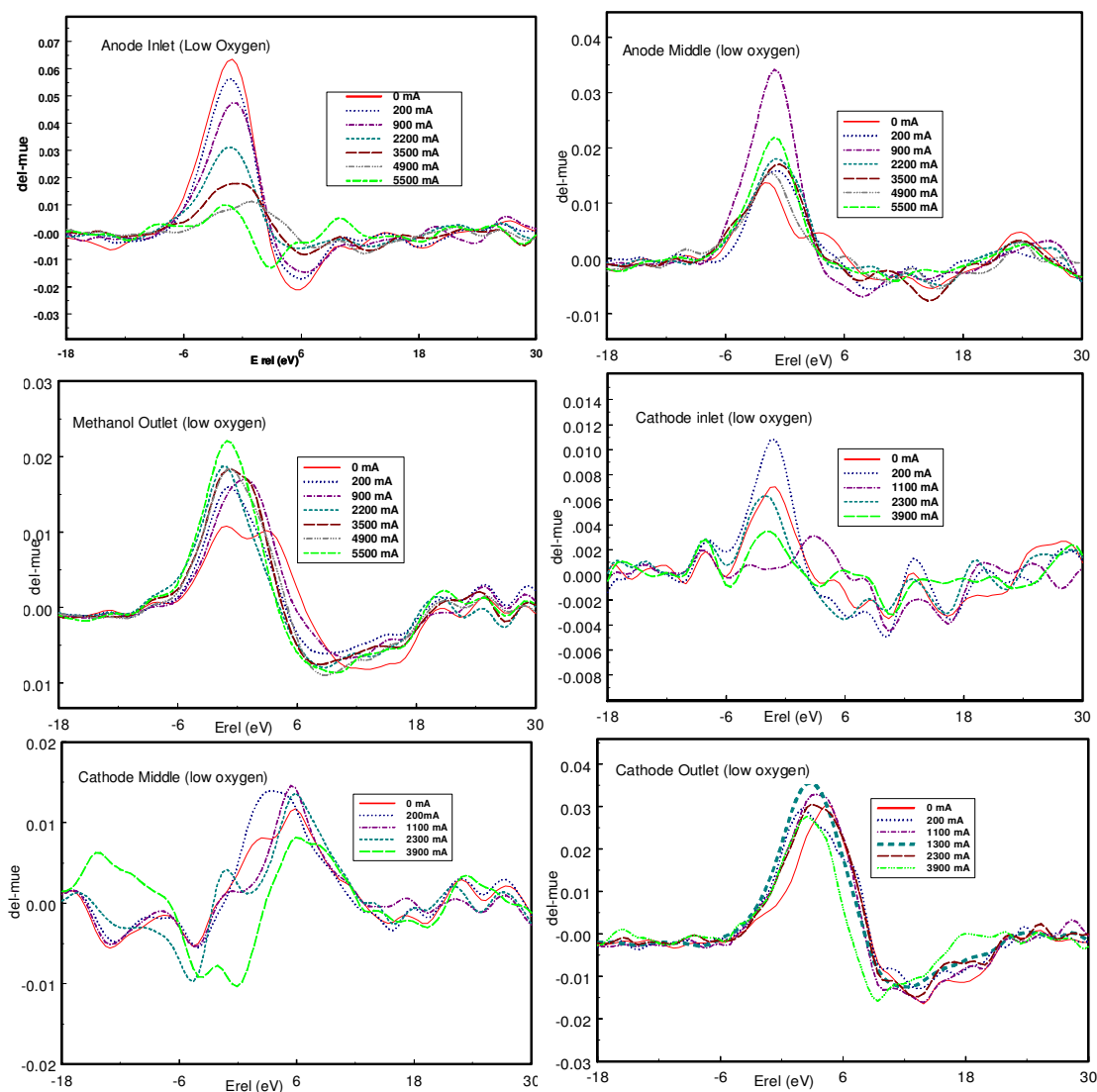


Figure 44: $\Delta\mu$ signatures: different regions of anode and cathode under different cell voltages at low oxygen flow

Of course this is not necessarily true, but Figure 46 is drawn only to emphasize the qualitative change in anode and cathode potentials and the predicted adsorbate coverages with O₂ concentration.

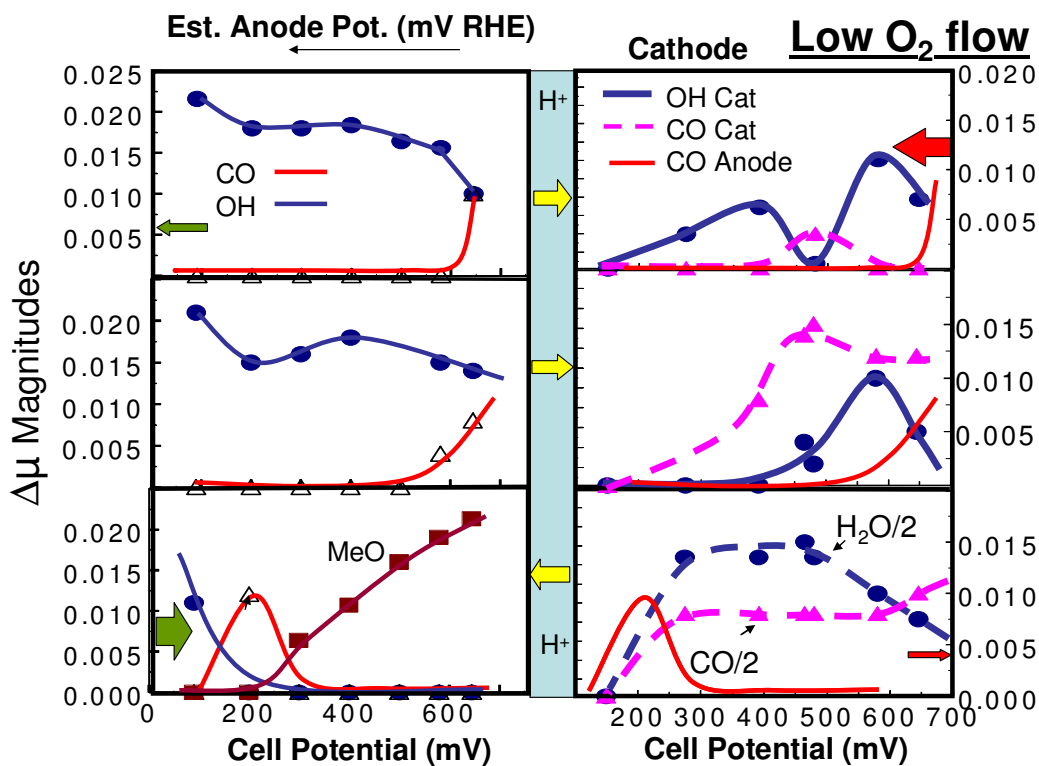


Figure 45: $\Delta\mu$ magnitude obtained for different regions of anode (left) and cathode (right) under low oxygen flow.

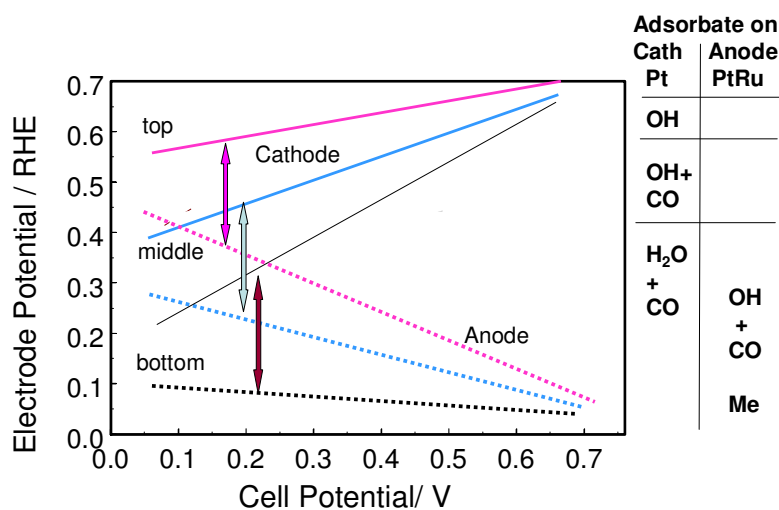


Figure 46: Estimated anode and cathode potential under low oxygen flow

From Figure 46 it may be assumed that at the bottom window, the anode potential never gets much above 0.1 V, but at the top window, it proceeds similar to that at 200 mL/min O₂ flow. The predicted cathode and anode potentials drawn in Figure 40 are some effective average of these 3 “window” local potentials.

If the results at the lower O₂ flow rate are going to be similar to those at the higher flow rate, this should occur at the top window near the O₂ inlet, where the O₂ concentration is the highest and the methanol concentration is probably still reasonable having survived because of O₂ starvation, and hence lower currents near the bottom. Indeed, Figure 45 shows very similar results, showing the CO coverage dropping in the BF region with the OH coverage rising and the OH coverage on the cathode showing the two maxima at similar cell potentials (350 and 600 mV). The fact that these so called BF and DL maxima fall at similar cell potentials found for the high O₂ flow indeed suggest that the cell potential is governed primarily by the anode at the top window. The CO coverage on the anode in the middle and bottom window now reflects an increasing shift to lower cell potential (higher anode potential) for oxidation of the CO, consistent with the expected shift in anode/cathode potential as depicted in Figure 46. Indeed at the bottom window there exist apparent methanol (or other oxidation intermediate) at all cell potentials above 200 mV, suggesting that the anode potential is below or near 100 mV over this entire region. On the cathode, in the middle window, and particularly in the lower window, very different behavior is evident. In both the middle and lower windows (and even a bit in the upper window), significant amounts of CO are found. This arises because methanol cross-over

is occurring, and the low O₂ flow rate does not facilitate the flushing out of this methanol. This allows some of it to be oxidized resulting in CO or C1 (C1: formaldehyde or formic acid) poisoning species on the cathode. Note that this CO coverage appears with increasing cell potential with increasing O₂ starvation, consistent with the faster decrease in cathode potential with cell potential as schematically shown in Figure 46. The OH coverage in the top and middle windows is consistent with the CO coverage on the anode, i.e., the OH coverage increases right when the CO coverage on the anode decreases, consistent with the high O flow results. Very different adsorbate coverages are seen in the O₂ starved region at the bottom window; with the adsorbate coverage large at the cell potentials when the methanol is on the anode. It is suspected that the OH coverage may in fact be H₂O coverage, because the $\Delta\mu$ signature is the same for H₂O and OH. Previously it has been seen, adsorbed H₂O at potentials just below those when OH becomes visible [110]; thus the identification of H₂O and CO at this cathode potential in Figure 46. It would also be a bit unexpected to see large amounts of OH and CO because they should react to form CO₂, thus H₂O is assigned preferentially at the O₂ outlet on the cathode. Finally, it may be also assumed that large amounts of water may build up in this region pushed down by gravity from the regions (oxygen inlet and middle) and not flushed out of the cathode because of the low O₂ flow. Quite striking is the small coverage of all adsorbates at low cell potential on the cathode. The reference utilized to obtain the $\Delta\mu$ curves at the anode was in all cases the μ at 200 mV (highest current), so this by definition gives a zero coverage.

These results for low O₂ flow dramatically reveal how the cathode is dictating in part what occurs on the anode, i.e. the cross-talk is occurring in the reverse direction as observed before, as the cathode is now dictating the anode potential. The lack of a “sink” for the protons coming across from the anode, does not allow oxidation of the methanol until at lower cell potential. Clearly the DMFC at the bottom window is operating “bifunctionally”; i.e. in the normal galvanic mode with protons going from the anode to the cathode at low cell potential and higher current, but electrolytically at higher cell potential and lower current, with methanol being oxidized at the anode, and protons in this region proceeding in the opposite direction to produce H₂ at the anode. This bifunctionality has been seen previously by Sauer *et al.* [2][111], from measurements of the local current, but this is the first measurement of the adsorbates existing on the Pt anode and cathode in this electrolytic mode during operation. Kulikovskiy *et al.* [79] have found that after bifunctional operation of the DMFC with reduced O₂ feed, the DMFC actually performs better when the O₂ flow rate is restored again. They show that both the anode and cathode are improved in the regions where the DMFC operated electrolytically,

and suggest that the Pt cathode is cleaned by oxide removal, and the electrochemically active surface area (ECAS) of the anode is increased, brought about by the H₂ evolution during electrolytic operation. This Pt cathode cleaning may explain the surprisingly large $\Delta\mu$ magnitudes in this bottom region, $\Delta\mu_{\text{H}_2\text{O}} + \Delta\mu_{\text{CO}} \sim 0.04$ compared with about 0.02 in the top and middle regions, a factor of 2 larger. It cannot confirm, however, whether this increased $\Delta\mu$ total arises from simply higher adsorbate coverage in this bottom region, or an increased Pt surface area due to oxide removal during electrolytic operation.

6.2.4 Fuel starvation results

The polarization curve obtained during the fuel starvation process is shown in Figure 47. Fuel starvation can typically take place in those areas of the fuel cell stack, where methanol concentration is sufficiently low. Since a DMFC stack operates in a constant current mode, fuel starvation can induce cell reversal by taking the current from non-starved cells. However, such a situation rarely happens in a single cell, as the reaction is endothermic, or in other words, an external energy source is required to induce the cell reversal.

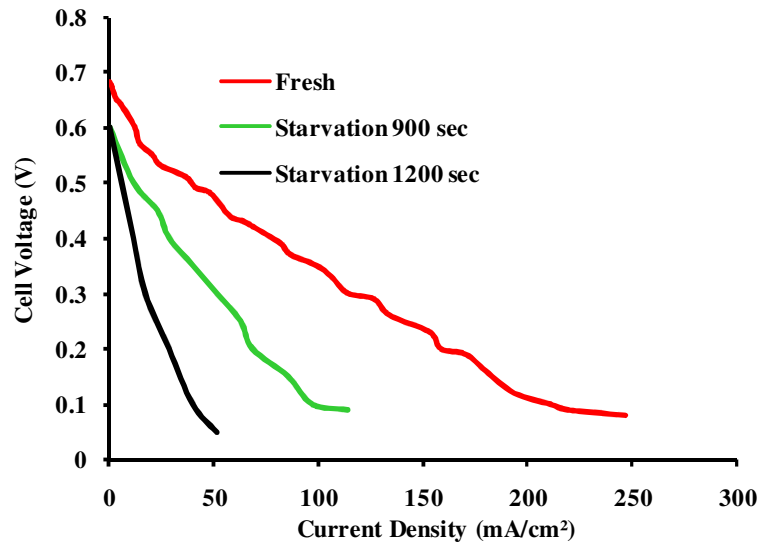


Figure 47: Polarization obtained during the fuel starvation studies

In the present study, fuel starvation is induced by a potentiostat operating in chronopotentiometric mode. Switching off the methanol is followed by a steady increase in the electrode potential and after holding for 900 sec, the cell voltage almost climbed to 1.5 V. A third fuel starvation cycle induced a complete degradation of the DMFC, so that the fuel cell delivered zero current. XANES spectra recorded during the fuel starvation process reveal a progressive oxidation of Ru and Pt, which is shown in Figure 48 and Figure 49.

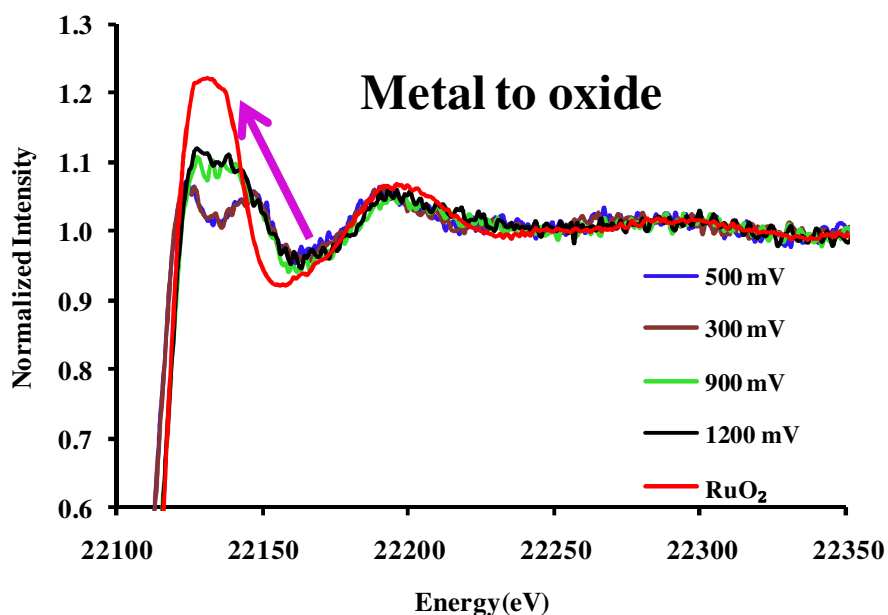


Figure 48: Ru K edge XANES spectra during fuel starvation studies

It can be seen from the Figure 48 that XANES spectra at 900 mV and 1200 mV are identical to the RuO₂ spectrum, while those at low potential resemble metallic Ru. Thus, cell potentials above 0.7 V can start degrading the fuel cell catalyst, as under these conditions Ru present in the Pt/Ru catalyst starts getting oxidized. Spatially resolved starvation studies at the Pt edge revealed the oxidation of the Pt catalyst, as the starved samples showed a higher white line intensity compared to the catalyst, which was aged under normal operation conditions. The EXAFS analysis of fuel starved at Pt L₃ edge in Table 9.

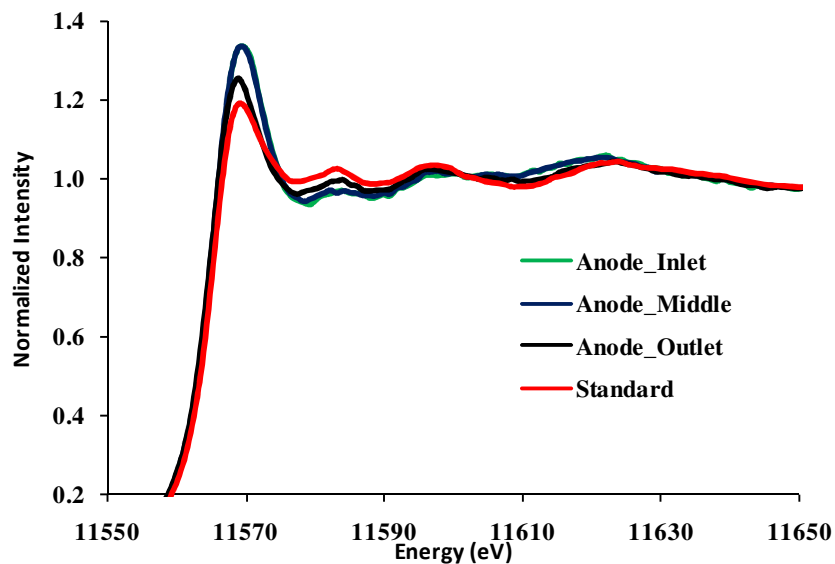


Figure 49: Pt L₃ edge XANES spectra from the different regions of the fuel cell after fuel starvation

	Inlet	middle	outlet
rPt-Pt (Å)	2.73	2.74	2.73
NPt-Pt	3.6	3.8	4.0
E ₀ Pt-Pt (eV)	5.95	5.95	5.04
rPt-Ru (Å)	2.72	2.73	2.72
NPt-Ru	1.0	1.1	1.2
E ₀ Pt-Ru (eV)	6.86	8.68	9.23
rPt-O (Å)	1.94	1.94	1.93
NPt-O	1.2	1.1	0.6
E ₀ Pt-O (eV)	-1.00	-1.64	-2.95

Table 9: Pt L₃ edge analysis of fuel starved anode samples

However, it is interesting to note that the extent of oxidation of the catalyst is not uniform across the different regions of the fuel cell, as it can be seen from Figure 49. The anode outlet region has a much lower white line intensity than the other two regions, or in other words, at the methanol outlet regions the catalyst is least oxidized. EXAFS analysis of the Pt L₃ edge also reveals a higher coordination number $N_{\text{Pt-O}}$ for the methanol inlet regions. Similar results are also obtained for the Ru K edge study, which is shown in Figure 50.

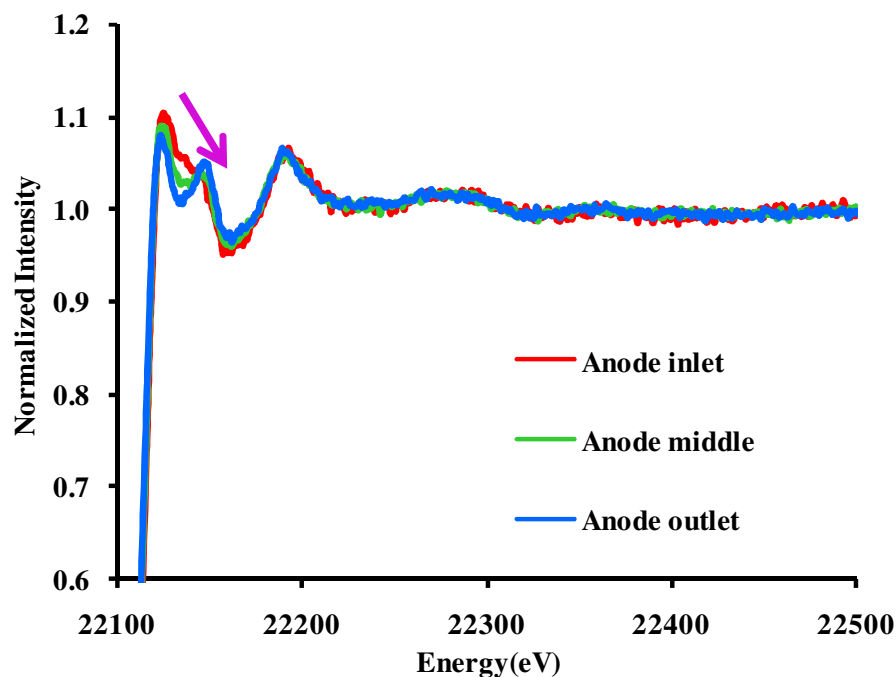


Figure 50: Ru K edge XANES spectra from different regions after fuel starvation

It can be seen from the Figure 50 that the XANES features of the anode outlet resembles the metallic Ru features and both anode middle and inlet are similar to that of the RuO₂. Further information on the extent of oxidation of the catalyst is obtained from the EXAFS analysis, which also reveals a higher coordination number ($N_{\text{Ru-O}}$) for both inlet and middle. The EXAFS analysis obtained after the fuel starvation process is summarized in Table 10. More information on the nature of the oxide species formed during the fuel starvation is obtained from the bond distance $r_{\text{Ru-O}}$. It can be seen that the bond distance $r_{\text{Ru-O}}$ for the catalyst during the fuel starvation process is much smaller than the one after the fuel starvation process. Thus, it may be assumed that at high potentials during the starvation process, Ru predominantly

exists in its anhydrous oxide form, which is subsequently changed to the hydrous form during resumed methanol flow. Again this finding is in good agreement with Ross *et al.* [107].

	$N_{\text{Ru-Pt}}$	$r_{\text{Ru-Pt}}(\text{\AA})$	$N_{\text{Ru-Ru}}$	$r_{\text{Ru-Ru}}(\text{\AA})$	$N_{\text{Ru-O}}$	$r_{\text{Ru-O}}(\text{\AA})$
Inlet	1.9	2.72	1.5	2.66	2.0	2.05
Middle	2.3	2.72	1.4	2.69	1.8	2.05
Outlet	2.7	2.72	1.9	2.69	1.5	2.05
Starvation	0.9	2.70	0.9	2.65	2.5	1.95

Table 10: EXAFS analysis Ru K edge, samples from different regions after fuel starvation and for comparison, EXAFS analysis of a sample during the starvation process is also shown.

The in-homogeneity in the degradation observed for the fuel starvation can be correlated to the amount of methanol available to provide the necessary current. It has already been seen in the previous section that, the methanol concentration decreases from the inlet to the outlet during fuel cell operation. The extent of decrease in the methanol concentration depends on the methanol flow rate, amount of current drawn and the geometry of the flow fields. Once the methanol flow is stopped, the necessary current is provided by the remaining methanol in the cell, which may already have a methanol gradient from inlet to outlet. Also the remaining methanol in the cell tends to accumulate more at the methanol inlet, which is at the bottom of the cell due to gravity. Thus the onset of the degradation might take place at the methanol outlet area, where it has a relatively low amount of methanol. With time the methanol outlet may dry out faster compared to the other areas, and hence no electrochemical reaction would be feasible and the degradation process completely stops. However, still a constant current is taken from the cell, but now from a smaller area. In order to compensate the loss from the inactive area, a high activity of the catalyst is expected from the inlet regions, which might be still having residual methanol and water. This high activity may lead to an intense degradation of the above region. Once the cell experiences a complete depletion of methanol, additional current is drawn from water hydrolysis or from the electrochemical oxidation of carbon support. Thus, the methanol inlet regions are degraded to a greater extent than the other regions.

The above mode of degradation does not necessarily occur in a DMFC stack, since complete drying of the stack rarely happens. However, events like low methanol flow, poor thermal management leading to overheating of stack, or poor water management can lead to excess

drying cells and ultimately can lead to the degradation of electrode. Thus it is necessary to maintain good thermal and water management and always sufficient amount of methanol should be fed in the fuel cell stack.

7 Shape-selected Pt nanoparticles as fuel cell catalyst

In this chapter studies of shape-selected Pt nanoparticles are presented. These were synthesized using different stabilizing agents such as tetradecyltrimethylammonium bromide (TTAB) and polyvinylpyrrolidone (PVP). The shape-selected particles were then characterized using TEM and their electrochemical activity tested using cyclic voltammetry. Finally, various shape-selected particles were supported on Vulcan carbon and carbon nanotubes (CNT), and tested in H₂ PEM fuel cell.

7.1 Experimental

7.1.1 Synthesis of shape-selected nanoparticles using TTAB

Shape-selected Pt nanoparticles stabilized by TTAB were synthesized by using a method described by Lee *et al.* [5]. In the present work, 600 mg of TTAB was dissolved in 15 ml de-ionized water. To the above solution 9 mg K₂PtCl₄ dissolved in 5ml of de-ionized water was added drop wise. The addition of K₂PtCl₄ solution to TTAB yielded a sparingly soluble orange precipitate. The above mixture was kept in a water bath at 60°C, until the solution became clear. To the above solution 22 mg NaBH₄ dissolved in 5ml of water was added. The H₂ gas evolved during the reaction was collected using a balloon. The whole solution was kept undisturbed at 60°C for 5 hrs. The initial orange color of the solution turned to light brown and then to dark brown, indicating the completion of the reaction. Large aggregates from the system were removed by centrifuging the solution at 6000 rpm for 30 min. Finally, the smaller shape-selected nanoparticles were separated by centrifuging at 15000 rpm for 15 min. Particles were re-dispersed and re-centrifuged to remove excess of surfactant. The above synthesis was also carried out in the presence of two support materials, Vulcan carbon and CNT. The CNT or the Vulcan carbon is dispersed uniformly with the TTAB-K₂PtCl₄ complex, before the reduction step with NaBH₄ is performed. Supported shape-selected nanoparticles were also made by impregnating the shape-selected nanoparticles on Vulcan carbon.

7.1.2 Synthesis of shape-selected nanoparticles using PVP

A modified polyol route as described by Lin *et al.* was used to synthesize PVP supported shape-selected nanoparticles [112]. In a typical synthesis 138 mg of NaNO₃ and 111 mg of

PVP was dissolved in 100 ml of ethylene glycol. 160 mg of CNT is now ultrasound dispersed in the above solution. The dispersion was kept in an oil bath at around 160 °C for about 5 min. To the above dispersion 130 mg of H₂PtCl₆ 6H₂O in 5 ml ethylene glycol is added and kept undisturbed for an hour. Finally the dispersion is washed (Acetone) and filtered to get supported shape-selected nanoparticles. The nanoparticles synthesized by different routes were characterized by TEM (details in section 5.1.3).

7.1.3 Electrochemical studies: Cyclic voltammetry (CV)

All the CV measurements were carried out using a Gamry potentiostat. Shape-selected nanoparticles were drop-casted into a glassy carbon working electrode and dried. The working electrode is dipped into 0.5 M H₂SO₄, which acts as a supporting electrolyte. The CV measurements were performed at a scan rate of 25 mV/sec in the potential range of -0.3 V to 1.25 V, using a Pt foil counter electrode and Ag/AgCl reference electrode.

7.1.4 MEA fabrication and fuel cell test

The MEA was fabricated using a modified air brush technique developed by Wilson *et al.* [113]. In the present study catalyst powder was made into a viscous ink by ultrasound dispersing of the catalyst powder with isopropanol-water mixture in 1.5 ml Nafion solution. The amount of isopropanol-water mixture can vary depending on the support material. However, the amount of Nafion solution was always kept constant for all the MEA fabricated. The amount of catalyst powder was taken in such a way that the MEA has an overall loading of 1.2 mg/cm² of Pt (except for the impregnated shape-selected Pt). The ink prepared was then sprayed onto a Nafion 117 membrane using an air brush pistol. For all the fabricated MEA, one of the electrodes was always made of commercial Pt catalyst from JM (20% Pt on Carbon). The fabricated MEA was operated in a H₂-PEM fuel cell with the shape-selected catalyst tested for both anode and cathode activity. The PEM fuel cell was operated at 70°C with the anode compartment supplied with humidified H₂ gas at a flow rate of 150 ml/min. The cathode feed was constituted of non humidified O₂ gas at a flow rate of 75 ml/min. Polarization curves were recorded and compared with that of a standard MEA to evaluate the activity of the synthesized catalyst.

7.2 Results and discussion

The synthesized samples are analyzed with TEM which revealed various shapes depending on the reaction conditions especially for the particles synthesized with TTAB. TEM images obtained for various samples synthesized using TTAB are shown in Figure 51.

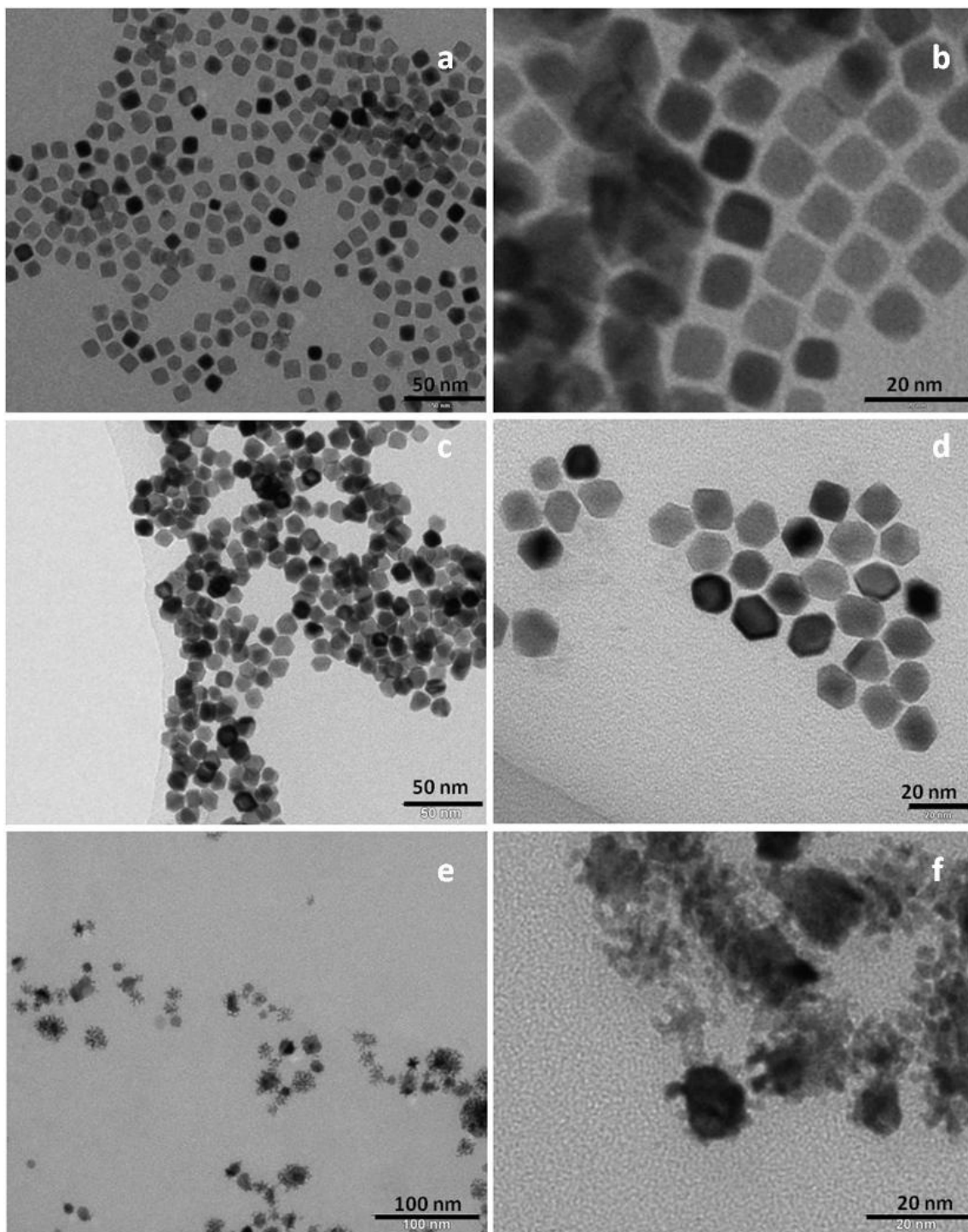


Figure 51: TEM images of shape-selected particles, a) & b) showing predominantly cubic particles (high pH), c) & d) showing particles with cubooctahedral shape, e) & f) showing porous particles (low H₂ gas).

From the TEM images it is clear that the present synthesis yielded shape-selected particles and the particles formed are in the size range of 10-15 nm with a mean particle size around 12.5 nm. The particle size distribution from the images c & d is shown in Figure 52.

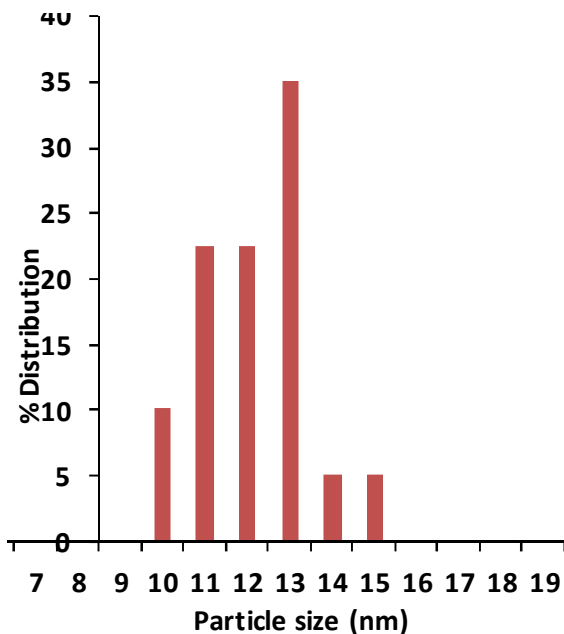


Figure 52: Particle size distribution from TEM

It was found that addition of NaOH to the reactant solution increased the formation of cubic particles (high pH 10-11), but a 100% shape distribution could not be achieved (Figure 51 a & b). Further increasing the pH (above 12) of the solution yielded so called porous particles, but a more close look revealed that they are ultimately forming cubic or octahedral particles. Thus by using the TTAB route, shape-selected particles were successfully synthesized.

Although in the present work detailed structural investigation has not been performed on these samples, from various literature results, one can correlate various shapes obtained here to preferential growth of different Pt facets [5][4][114][115]. For e.g. Gullon *et al.* assigned preferential exposure of (100) facets for cubic shape particles and both (100) and (111) for cuboctahedral particles [4]. Further various shape-selected particles can be characterized electrochemically by their characteristic hydrogen adsorption-desorption peaks in a cyclic voltammogram. This dependency is clearly shown by Gullon *et al.* by studying different shape-selected nanoparticles. In their study, they assigned the desorption peak around 0.12 V

vs. reversible hydrogen electrode (RHE) to Pt (110) facets, (100) facet to the peak observed around 0.27 V vs. RHE, and further peaks at higher potential 0.5V vs. RHE to (111) facets. The cyclic voltammetry studies done on the unsupported shape-selected nanoparticles synthesized in the present study also showed hydrogen desorption peaks characteristic to different facets, predominantly Pt (110) and Pt (100). The cyclic-voltammogram obtained for shape-selected particles and the commercial catalyst is plotted in Figure 53.

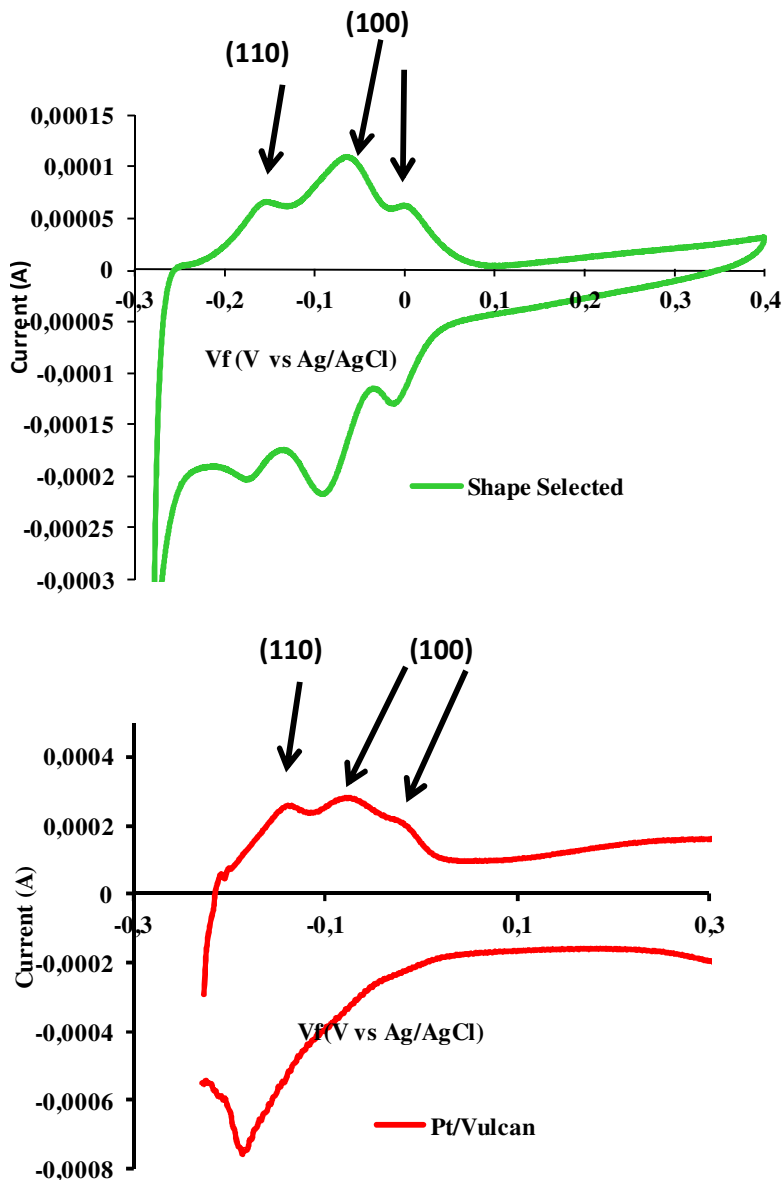


Figure 53: Cyclic-voltammogram, (top) shape-selected particle, (bottom) Pt/Vulcan

The arrows indicate the hydrogen desorption regions for different facets. However, sharp features characteristic to single crystal surfaces are absent for the sample indicating possible adsorption of surfactant on the surface. If it is assumed that the CV obtained for the Pt/C commercial catalyst (red) is representing polycrystalline Pt electrode, then these features will be present to a different extent of the shape-selected Pt particles. This was again clearly shown by Gullon *et al.* for various shape-selected particles, for e.g. in the CV curve for (100) preferentially oriented particles (cubic shape), the intensity of the (100) peak is much higher than the others. It can be seen in Figure 53 (top) that the CV curve obtained for shape-selected particles is characterized by a high amplitude peak around -0.07 V vs. Ag/AgCl, which can be assigned to preferentially oriented Pt (100) surface. Thus it may be concluded that the above sample has a slightly higher ratio of Pt (100) preferentially oriented particles over (110). On repeated high potential cycling it was observed that the amplitude of the peak corresponding to the Pt (100) decreased dramatically, whereas only little change was observed for the Pt (110). The above result is shown in Figure 54. Hence it may be concluded that the Pt (100) surface degrades faster than Pt (110).

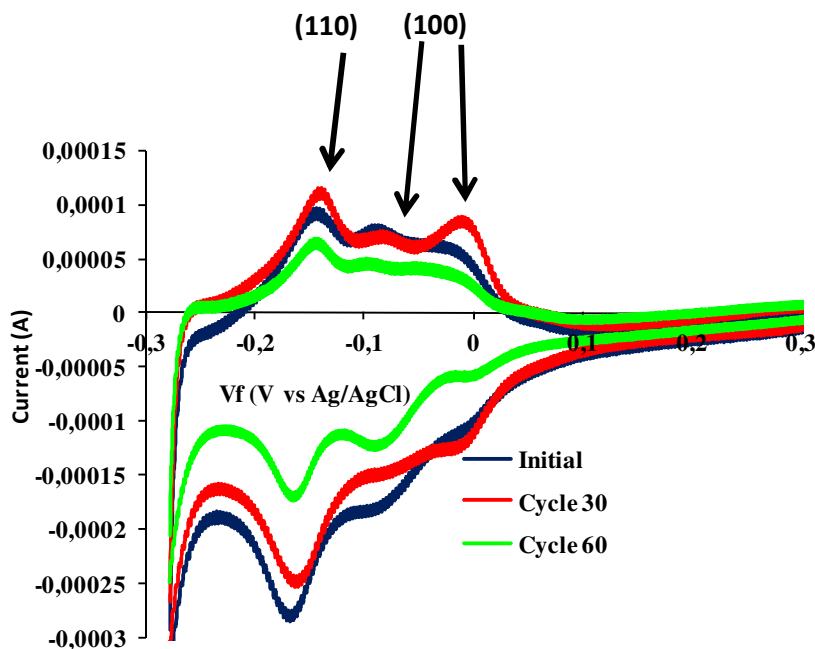


Figure 54: Cyclic-voltammogram of shape-selected particles at different cycles

In order to get more information about the structural changes due to electrochemical cycling TEM investigation was done on electrochemically cycled samples and is shown in Figure 55. However, TEM images of the electrochemically cycled sample still showed a large number of shape-selected particles, mostly aggregated. Careful investigation also showed the presence of a few spherical particles.

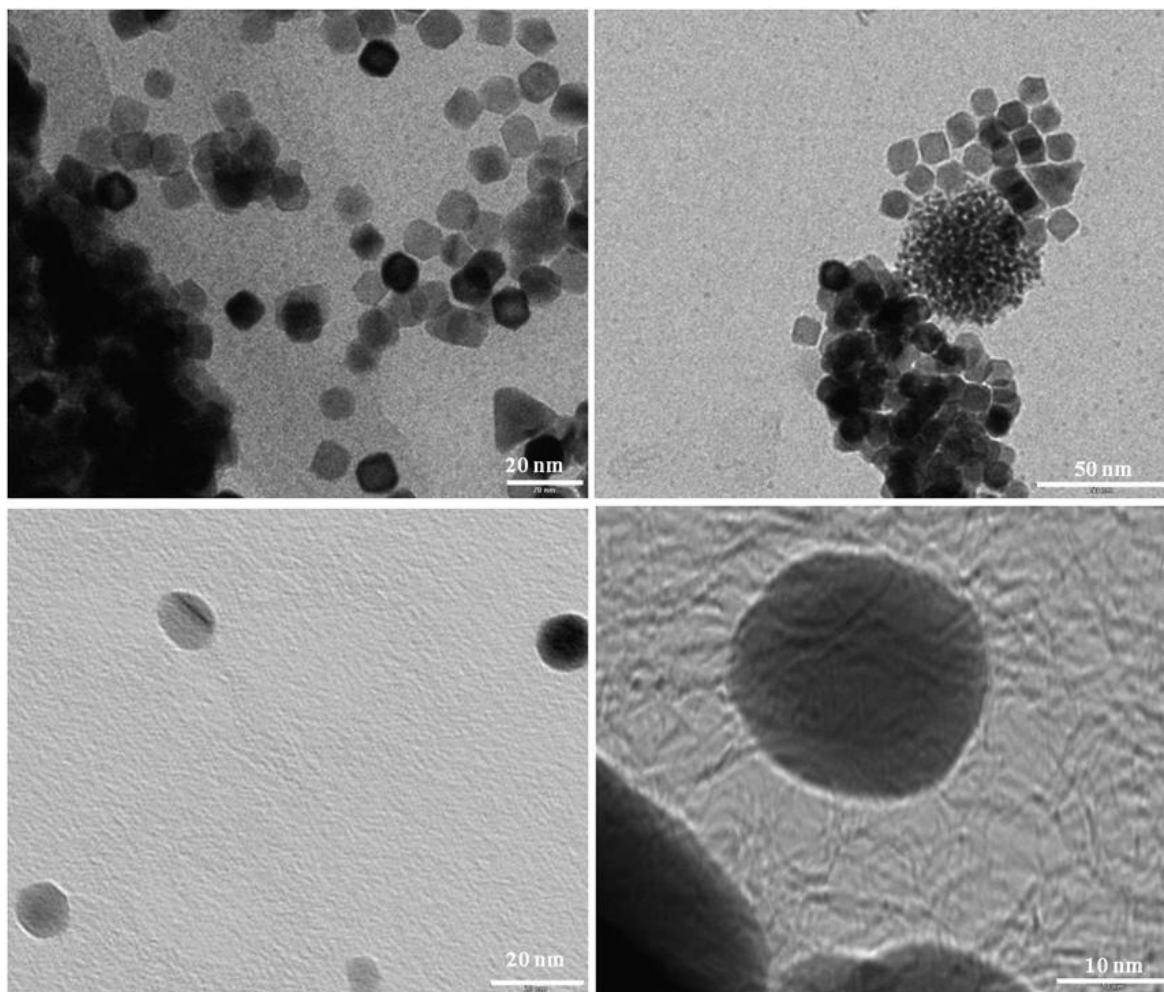


Figure 55: TEM micrograph of the shape-selected particles after electrochemical cycling

TEM investigation also revealed particle growth with some of the particles growing up to 20 nm. It may be concluded that the shape-selected particles after electrochemical cycling may be now constituted mainly of particles with (110) and (111) facets, but any definite conclusion could be only made after detailed structural investigation. Also in the present sample, no shape discrimination was done as it contained both cubic and octahedral particles. Hence, it is not yet clear, which of the particles degrade faster.

From the electrochemical studies it is clear that the unsupported shape-selected particles show electrocatalytic activity. However, for real fuel cell operation supported catalysts are preferred over a non supported catalyst. Therefore, the shape-selected synthesis was carried out in the presence of carbon and carbon nanotubes. However, the presence of any support material in the reaction mixture leads to the formation of large numbers of irregular particles. The TEM images obtained for the sample, synthesized using TTAB and Vulcan carbon as support material is shown in Figure 56.

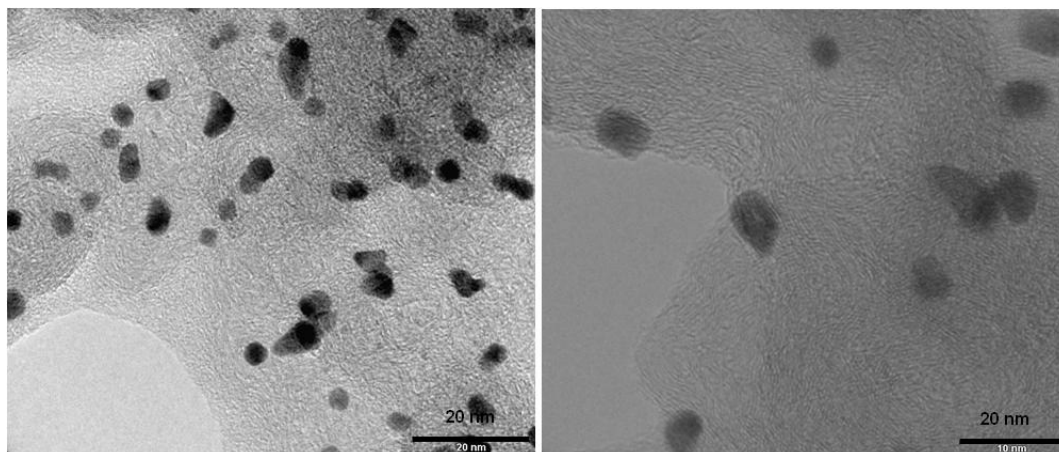


Figure 56: TEM micrograph of Pt particles synthesized in the presence of TTAB and Vulcan carbon

The irregular shape of the particles may be due to the fact that the Vulcan carbon surface may contain a large number of different functional groups and depending on the group it may attach weakly or strongly to the Pt surface. Consequently the nucleation may not proceed in the same way as it happened in the absence of support materials and lead to the formation of irregular particles.

The above reaction was further modified using CNTs as support materials, which yielded much more shape-selected particles than in the presence of Vulcan carbon. The CNT supported shape-selected Pt nanoparticles were also prepared using PVP in presence of NaNO_2 .

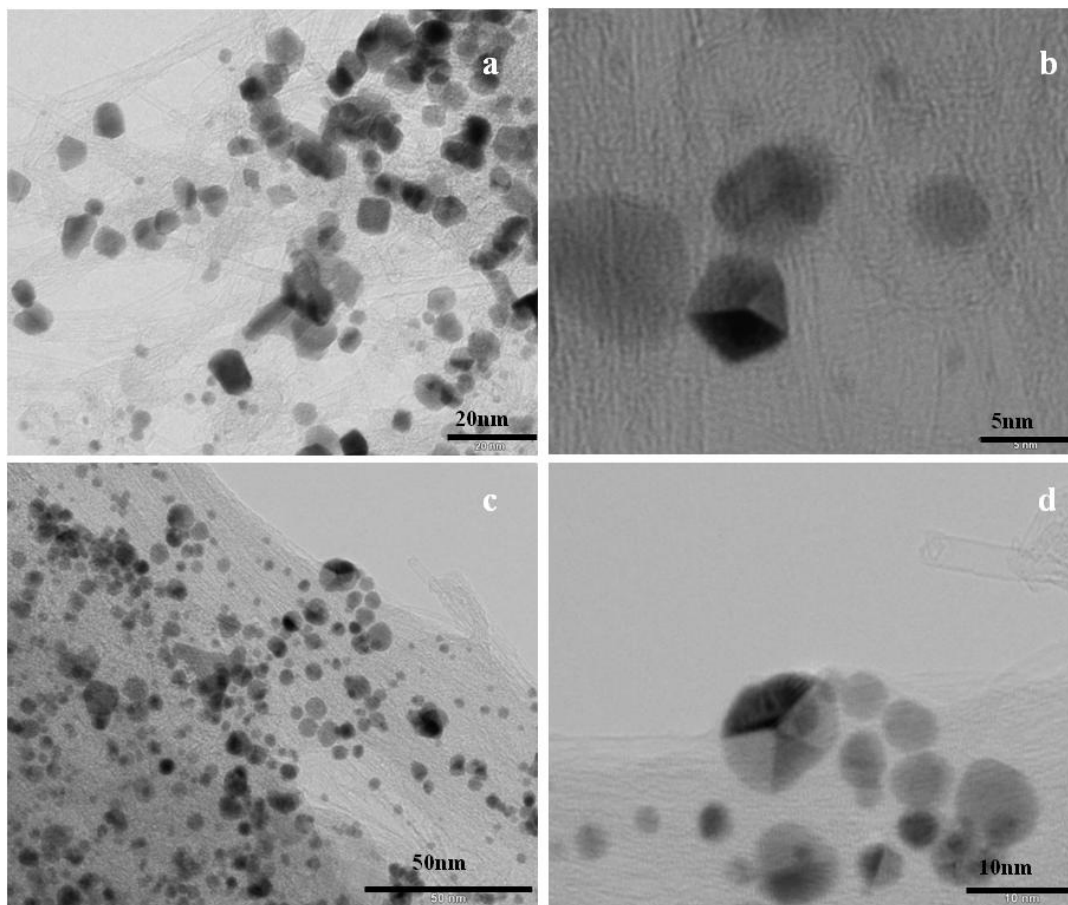


Figure 57: TEM micrograph of Pt particles synthesized a), and b) in the presence of TTAB and CNT, c) and d) in the presence of PVP and CNT

The TEM image of the particles supported onto CNTs are shown in Figure 57. From the TEM images (Figure 57 a & b) it is clear that TTAB synthesis using CNTs support produces more shape-selected particles than the PVP synthesis (Figure 57 c & d). In both syntheses large and irregular particles were seen, therefore it may be concluded that monodispersed shape-selected particles could not be synthesized in the presence of any support material.

Finally, unsupported shape-selected particles were ultrasound dispersed along with Vulcan carbon to obtain impregnated shape-selected particles. The TEM image of the impregnated particles is shown in Figure 58. Although, with the above mentioned method almost exclusively shape-selected particles are produced, it is hard to achieve the desired Pt loading, as a large fraction of particles (basically large particles) are removed by centrifugation. In order to obtain the information on Pt loading in the impregnated catalyst, thermal analyses were carried out.

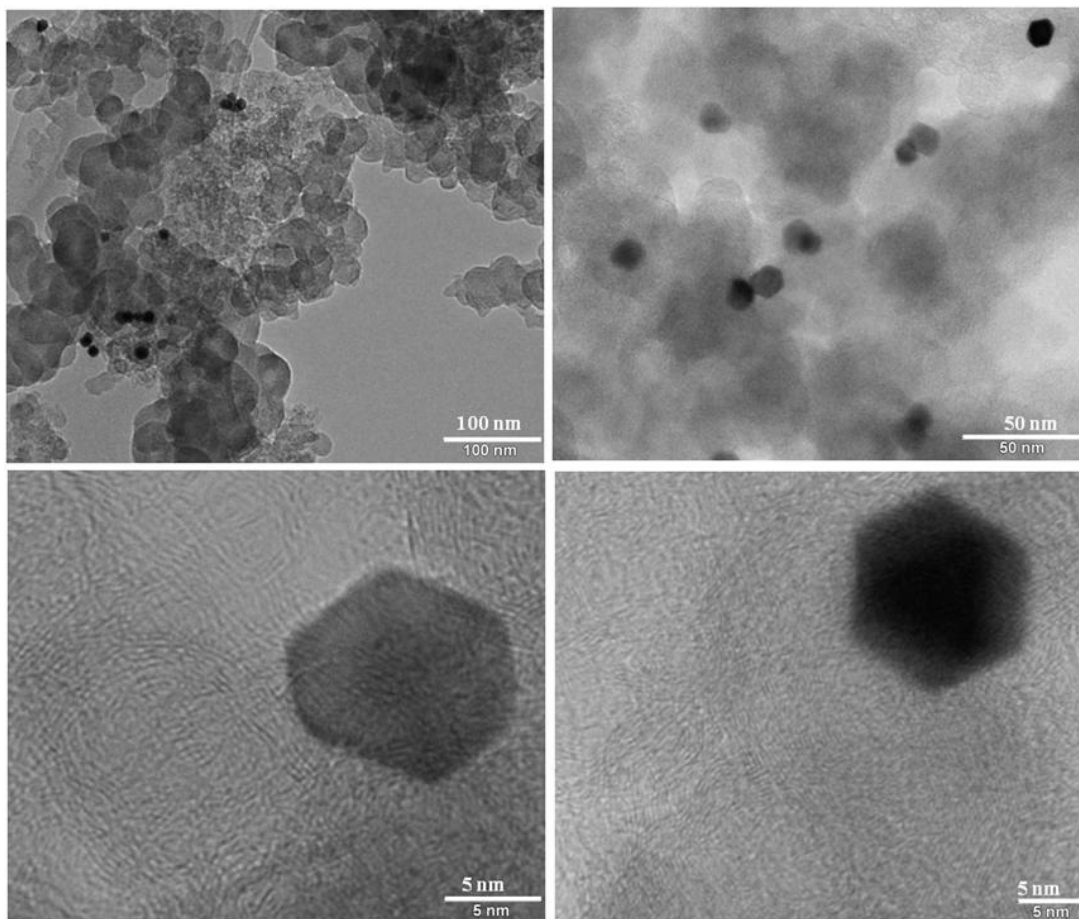


Figure 58: TEM micrograph of the impregnated shape selected catalyst; high and low magnification image

The TGA studies were carried out in synthetic air atmosphere and the sample was heated to 1000°C. The TG curve obtained for the shape-selected catalyst is shown in Figure 59. The carbon present in the sample was completely burnt in the temperature region of 450 to 600°C and overall platinum loading of 3.5 % was calculated from the residual mass. Using the above catalyst MEA was fabricated and the calculated metal loading in the above MEA was less than 0.21 mg/cm² which is five times lower than that for the commercial catalyst.

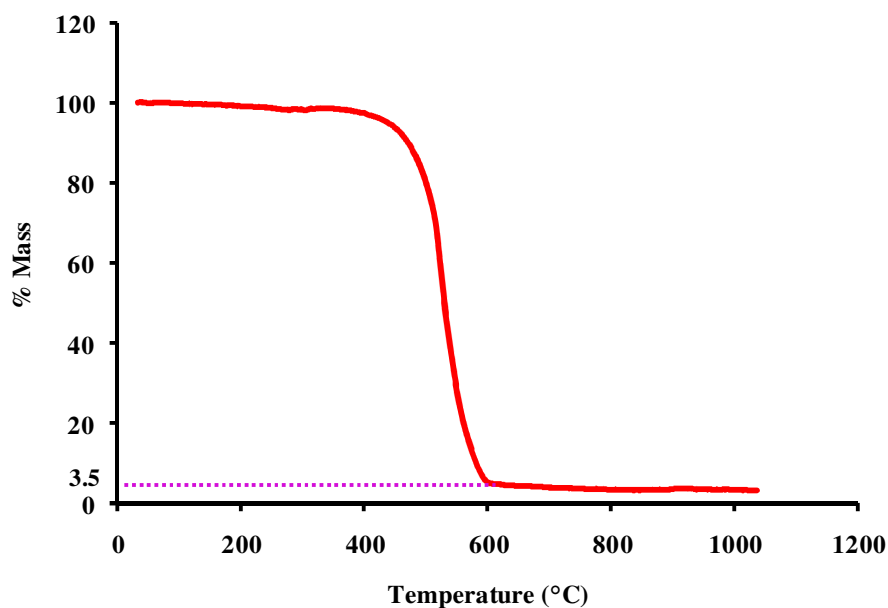


Figure 59: TG curve obtained for the shape selected catalyst

Finally, MEAs fabricated from various supported shape-selected particles were tested in a H₂ PEM fuel cell and their performances are compared with a standard MEA using commercial catalyst from JM. Polarization curves and power density curves obtained for the various synthesized catalyst, while performing as anodes are plotted in Figure 60.

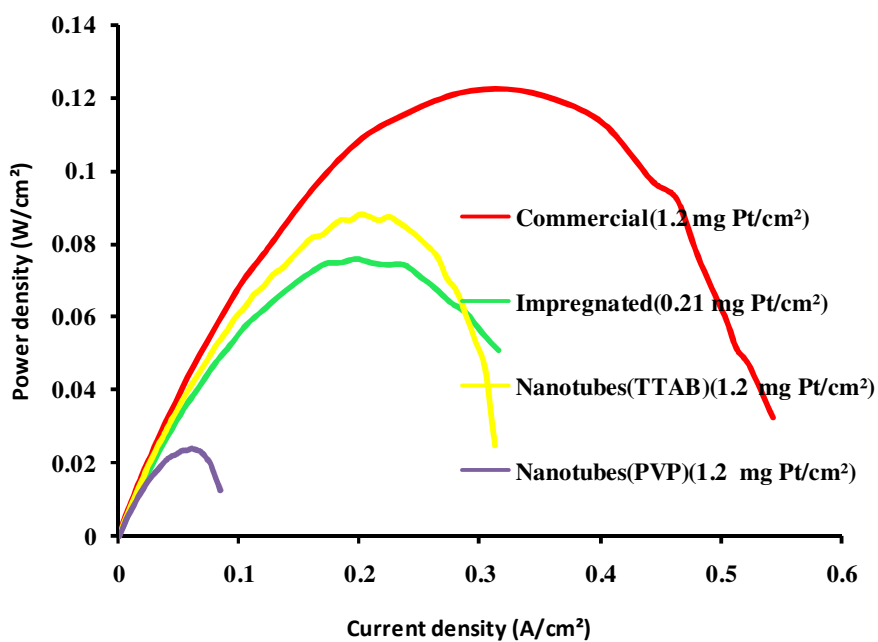
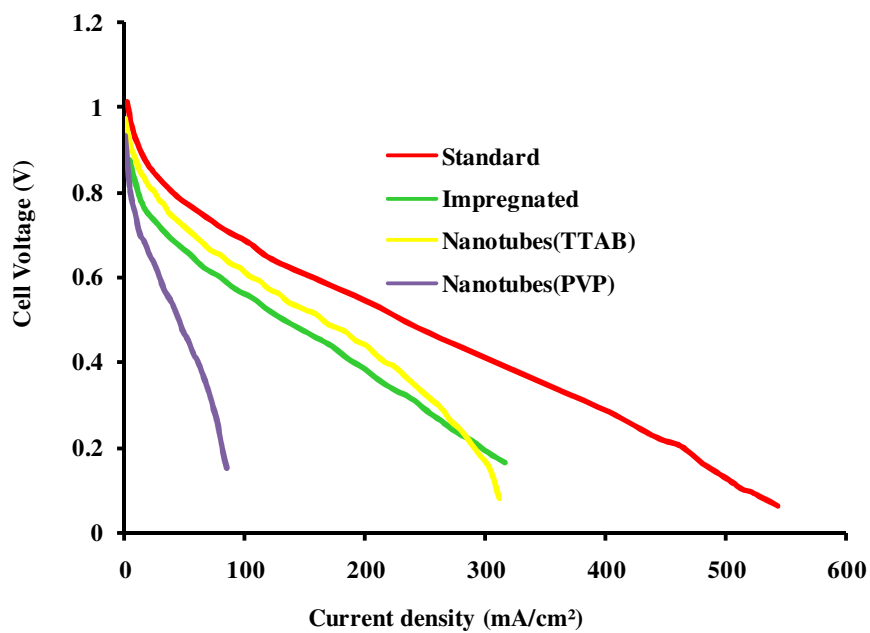


Figure 60: (Top) polarization curve obtained for different samples, (bottom) power density curve

From the polarization curves obtained from different samples, the MEA with the commercial catalyst showed the best performance and the catalyst synthesized using PVP showed the least. However, it has to be mentioned that the shape-selected impregnated catalyst has a much lower Pt loading (5 times) compared to the commercial catalyst. Thus in terms of effective utilization of the Pt catalyst, the shape-selected impregnated catalyst outperforms the commercial catalyst. By tuning the shape of the catalyst one can effectively utilize the Pt and thereby reduce the metal loading, ultimately lowering the cost. Further the impregnated shape-selected particles showed similar fuel cell performance when they were either used as cathode or anode catalyst. This is quite crucial, since the ORR in fuel cells is a relatively slow process compared to HOR, hence it is preferred to have a highly active catalyst at the cathode. It is worth mentioning that in contrast to the impregnated catalyst, the nanotubes supported shape-selected catalyst when it was used as cathode catalyst showed a lower fuel cell performance than when it was used as anode (not shown). The polarization curves obtained when the shape-selected particles were used as anode and cathode are plotted in Figure 61.

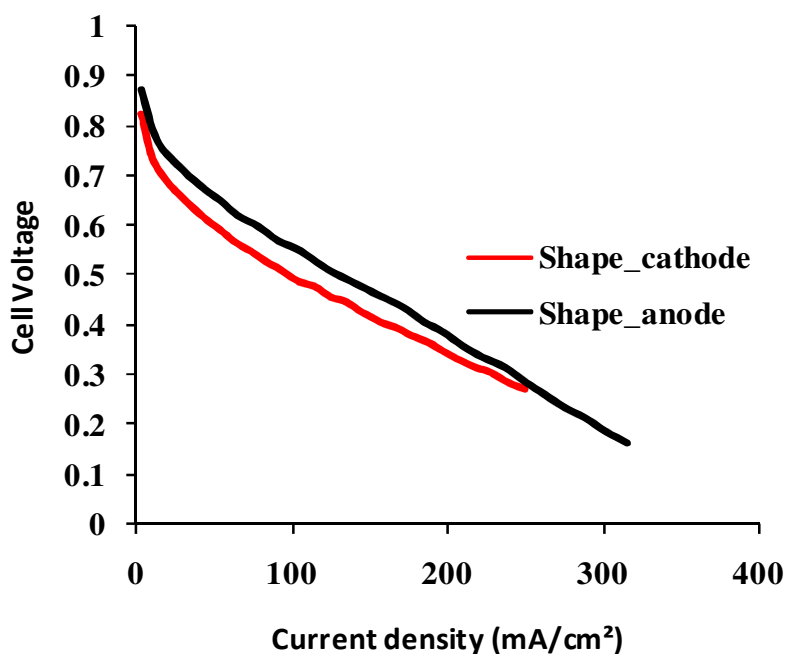


Figure 61: Polarization curves obtained for the shape selected catalyst when used as cathode (red) and anode (black). (Same MEA was used for both experiment, gas connections and electrical connections were inverted)

From these studies it is clear that shape-selected particles are quite promising as fuel cell catalysts. Further, the fuel cell performance can be enhanced by carefully removing the capping group from the catalyst surface. Optimizing the experimental conditions can further help to control the shape and size of the particles and thereby can reduce the Pt loss.

8 Summary and Outlook

8.1 Summary

In this thesis spatially resolved *in-situ* as well as *ex-situ* studies were carried out on DMFC electrodes. The *ex-situ* analysis was carried out on aged DMFC stack electrodes operated for more than 5000 hrs. The aged catalyst morphologies of both anode and cathode were characterized by different techniques like TEM, XRD, SEM-EDX, and XAS. The results obtained were compared with the morphology of a pristine MEA as well as commercial catalysts to evaluate the extent of degradation. It was found that particle growth and Ru dissolution play a significant role in the degradation of DMFC electrodes. The MEA fabrication technique itself has a profound effect on the particle growth, as the cathode catalyst showed a dramatic increase in particle growth during the MEA fabrication. The heat treatment and ultrasound dispersion steps used during the fabrication process are decisive factors for the observed particle growth. As particle growth can bring down the ESA, a more mild MEA fabrication technique should be developed. Interestingly, ruthenium oxide present in the anode catalyst, stabilized the anode particles against particle growth during the MEA fabrication. However, the ruthenium oxide can undergo different structural changes during the fuel cell operation. It can either favorably affect the MOR activity of the anode catalyst or adversely affect the durability of the fuel cell as it can dissolve Ru and lead to Ru crossover.

In-situ XAS studies on the anode of the DMFC tracked the structural changes of the ruthenium oxide. It was found that a large fraction of the ruthenium oxide present in the anode catalyst became reduced during fuel cell operation and led to the formation of unalloyed Ru (Ru islands). These Ru islands play a major role in the mechanism of the MOR, as large sized islands help the CO removal from Pt by a direct ligand mechanism and small islands do the same at much lower anodic potentials through the BF mechanism. However, compared to Pt, Ru is less noble and can leach out quite easily after an event of cell reversal due to fuel starvation or short circuit. XAS and EDX mapping studies on the aged DMFC cathode stack revealed the presence of crossover Ru. Not only the Ru dissolution deteriorates the activity of the anode catalyst but also the cathode, as a large fraction of crossover Ru can block the active sites of the cathode catalyst and thereby reduce its ORR activity. Ru was also found in the

Nafion membrane as precipitates, predominantly at the methanol outlet regions or the oxygen inlet regions. The preferential formation of the Ru precipitates at the methanol outlet regions is due to the cell reversal occurring due to methanol starvation. This fact was again supported by EXAFS results of the samples from methanol outlet regions where it predominantly showed the presence of anhydrous RuO₂ which is known to exist at higher potential. The above results further confirm the existence of inhomogeneities (current and methanol) in the DMFC.

For the first time the in-homogeneities in DMFC were tracked by spatially resolved *in-situ* XAS studies. For this a new *in-situ* fuel cell was designed and optimized for XAS measurements. Using this cell, adsorbate coverage and structure from different regions of a DMFC like methanol inlet, outlet and middle regions and oxygen inlet, outlet and middle regions were compared. From the results a strong spatial dependence in adsorbate coverage, and therefore expected current density relative to the inlet and outlet of methanol and O₂ gases was found. Also, a very strong “cross-talk” between the anode and cathode is seen with the anode dictating at high O₂ flow rate the OH coverage on the cathode, resulting from the H⁺ cross over to the cathode, and the cathode at low O₂ flow rate dictating the CO oxidation on the anode via methanol and H⁺ cross over. The electrode with the slowest rate (MOR at the anode or oxygen reduction at the cathode) dictates the local adsorbate coverage. These are the first results to show the direct correlation in space and potential of OH adsorbates on the cathode with H⁺ production at the anode during the MOR reaction. It points directly to the importance of the reductive adsorption, the first step in the ORR. Finally, the adsorbates found in the O₂ starvation region consistently correlate with the previously reported spatially resolved current density measurements of Sauer, which show that a DMFC can go into bifunctional mode (electrolytic as well as the normal galvanic mode) [111]. In the O₂ starved electrolytic region at high cell potentials, large amounts of CO and H₂O were found on the cathode. From the above study it is clear that the in-homogeneity in methanol and oxygen flow affects the performance of the fuel cell and these in-homogeneities reduce the efficiency of the fuel cell, as the current distribution is not uniform. However, it is expected that in contrast to DMFC stack, methanol depletion in single cell has little impact on the catalyst degradation as in the former case the non-starved cells drive the starved cell leading to a cell reversal. But forced fuel starvation studies in single cells incurred irreversible damage to the cell. Although the degradation was found to be inhomogeneous, heavy oxidation of both Pt and Ru of the anode catalyst was confirmed by XAS studies.

Finally shape-selected Pt particles were synthesized using surfactants like PVP and TTAB. Synthesized particles were electrochemically tested and a strong dependency of the particle stability was observed with different facets. In the present study ESA from Pt (100) was found to degrade faster than (111). Thus controlling the shape of the particle can lead to better stable catalysts and thus durability of the fuel cell can be improved. The shape-selected particles were then supported onto carbon supports and their fuel cell performance was evaluated. It was found that these shape-selected particles show excellent fuel cell performance even though the Pt loading was extremely low. Thus tuning the shape of the nanoparticles can effectively improve the catalyst utilization and ultimately reduce the cost of the fuel cell.

8.2 Outlook

From the present studies it is clear that inhomogeneities associated with DMFC greatly enhance the degradation. Optimizing the fuel cell components such as GDL and flow field structure can solve the problem to a great extent. More detailed studies are required to understand the mechanism of Ru dissolution and crossover in DMFC. Morphology of the Pt/Ru catalyst as well as the operating conditions of the DMFC, need to be optimized, to reduce the Ru dissolution.

One of the drawbacks of the present XAS studies was poor resolution of the data, which was mainly due to QEXAFS mode of measurements and associated noise. Thus it is recommended to measure in conventional XAS mode whenever the problems with the bubbles are less. In future, development of new synchrotron facilities with high flux and beamlines capable of doing ultra fast XAS (PETRA) can solve this problem to a greater extent. Thus both time and spatially resolved measurements could be possible.

Spatially resolved XAS studies can be further extended to understand the degradation process in H₂-PEM fuel cells. Spatially resolved studies are quite important in H₂-PEM as non-uniform degradation is observed in H₂-PEM during a start-stop cycle. Further using a reformat gas as fuel can also lead to in-homogenous degradation as the CO concentration may decrease from inlet to outlet, and the highly poisoned area might degrade faster. Moreover the cathode flooding issues in H₂-PEM can be much worse than in the case of DMFC as the water produced in H₂-PEM is much higher. Therefore, H₂-PEM can experience localized degradation especially near oxygen outlet where the water tends to accumulate.

Finally using shape-selected particles as fuel cell catalyst can reduce the cost of the fuel cells as a lower amount of Pt is needed. This is quite good for DMFC as it has at least 4 times higher Pt loading than H₂-PEM. Present study is one of the first studies where shape-selected particles were actually used to run a fuel cell. However the shape-selected particles had to be synthesized in different batches to get optimum loading for fuel cell. In future, optimizing the synthesis condition can help in the large-scale production of catalyst and moreover, shape and size selectivity can be achieved.

Bibliography

- [1] S.M. Unni, V.M. Dhavale, V.K. Pillai, S. Kurungot, High Pt Utilization Electrodes for Polymer Electrolyte Membrane Fuel Cells by Dispersing Pt Particles Formed by a Preprecipitation Method on Carbon “Polished” with Polypyrrole, *The Journal of Physical Chemistry C*. 114 (2010) 14654-14661.
- [2] D.U. Sauer, T. Sanders, B. Fricke, T. Baumhöfer, K. Wippermann, A.A. Kulikovskiy, et al., Measurement of the current distribution in a direct methanol fuel cell--Confirmation of parallel galvanic and electrolytic operation within one cell, *Journal of Power Sources*. 176 (2008) 477-483.
- [3] S.-M. Park, S.-K. Kim, S. Lim, D.-H. Jung, D.-H. Peck, W.H. Hong, Experimental investigation of current distribution in a direct methanol fuel cell with serpentine flow-fields under various operating conditions, *Journal of Power Sources*. 194 (2009) 818-823.
- [4] J. Solla-Gullón, F.J. Vidal-Iglesias, A. López-Cudero, E. Garnier, J.M. Feliu, A. Aldaz, Shape-dependent electrocatalysis: methanol and formic acid electrooxidation on preferentially oriented Pt nanoparticles, *Phys. Chem. Chem. Phys.* 10 (2008) 3689.
- [5] H. Lee, S.E. Habas, S. KweSkin, D. Butcher, G.A. Somorjai, P. Yang, Morphological Control of Catalytically Active Platinum Nanocrystals, *Angewandte Chemie International Edition*. 45 (2006) 7824-7828.
- [6] J. Larminie, *Fuel Cell Systems Explained*, Second Edition, [Society of Automotive Engineers|SAE International], 2003.
- [7] S. Mukerjee, S. Srinivasan, M.P. Soriaga, J. McBreen, Effect of Preparation Conditions of Pt Alloys on Their Electronic, Structural, and Electrocatalytic Activities for Oxygen Reduction - XRD, XAS, and Electrochemical Studies, *The Journal of Physical Chemistry*. 99 (1995) 4577-4589.
- [8] S. Mukerjee, Particle size and structural effects in platinum electrocatalysis, *J Appl Electrochem*. 20 (1990) 537-548.
- [9] J.R.C. Salgado, E. Antolini, E.R. Gonzalez, Structure and Activity of Carbon-Supported Pt-Co Electrocatalysts for Oxygen Reduction, *The Journal of Physical Chemistry B*. 108 (2004) 17767-17774.
- [10] P. Yu, M. Pemberton, P. Plasse, PtCo/C cathode catalyst for improved durability in PEMFCs, *Journal of Power Sources*. 144 (2005) 11-20.

-
- [11] Z. Qi, A. Kaufman, Open circuit voltage and methanol crossover in DMFCs, *Journal of Power Sources*. 110 (2002) 177-185.
- [12] K. Wippermann, B. Richter, K. Klafki, J. Mergel, G. Zehl, I. Dorbandt, et al., Carbon supported Ru–Se as methanol tolerant catalysts for DMFC cathodes. Part II: preparation and characterization of MEAs, *J Appl Electrochem*. 37 (2007) 1399-1411.
- [13] W. Li, Y.-Z. Fu, A. Manthiram, M.D. Guiver, Blend Membranes Consisting of Sulfonated Poly(ether ether ketone) and Polysulfone Bearing 4-Nitrobenzimidazole for Direct Methanol Fuel Cells, *J. Electrochem. Soc.* 156 (2009) B258-B263.
- [14] J.G. Liu, T.S. Zhao, Z.X. Liang, R. Chen, Effect of membrane thickness on the performance and efficiency of passive direct methanol fuel cells, *Journal of Power Sources*. 153 (2006) 61-67.
- [15] A. Schröder, K. Wippermann, W. Lehnert, D. Stolten, T. Sanders, T. Baumhöfer, et al., The influence of gas diffusion layer wettability on direct methanol fuel cell performance: A combined local current distribution and high resolution neutron radiography study, *Journal of Power Sources*. 195 (2010) 4765-4771.
- [16] Q. Guo, Z. Qi, Effect of freeze-thaw cycles on the properties and performance of membrane-electrode assemblies, *Journal of Power Sources*. 160 (2006) 1269-1274.
- [17] S. Park, B.N. Popov, Effect of a GDL based on carbon paper or carbon cloth on PEM fuel cell performance, *Fuel*. 90 (2011) 436-440.
- [18] G.-B. Jung, C.-H. Tu, P.-H. Chi, A. Su, F.-B. Weng, Y.-T. Lin, et al., Investigations of flow field designs in direct methanol fuel cell, *Journal of Solid State Electrochemistry*. 13 (2008) 1455-1465.
- [19] X.-D. Wang, X.-X. Zhang, T. Liu, Y.-Y. Duan, W.-M. Yan, D.-J. Lee, Channel Geometry Effect for Proton Exchange Membrane Fuel Cell With Serpentine Flow Field Using a Three-Dimensional Two-Phase Model, *J. Fuel Cell Sci. Technol.* 7 (2010) 051019-9.
- [20] K. Kunimatsu, Infrared spectroscopic study of methanol and formic acid adsorbates on a platinum electrode: Part I. Comparison of the infrared absorption intensities of linear CO(a) derived from CO, CH₃OH and HCOOH, *Journal of Electroanalytical Chemistry and Interfacial Electrochemistry*. 213 (1986) 149-157.
- [21] A. Hamnett, Mechanism and electrocatalysis in the direct methanol fuel cell, *Catalysis Today*. 38 (1997) 445-457.
- [22] Hammer, Special Sites at Noble and Late Transition Metal Catalysts, *Topics in Catalysis*. 37 (n.d.) 3-16.

-
- [23] J.A. Rodriguez, D.W. Goodman, The Nature of the Metal-Metal Bond in Bimetallic Surfaces, *Science*. 257 (1992) 897 -903.
- [24] M. Watanabe, S. Motoo, Electrocatalysis by ad-atoms: Part I. Enhancement of the oxidation of methanol on platinum and palladium by gold ad-atoms, *Journal of Electroanalytical Chemistry and Interfacial Electrochemistry*. 60 (1975) 259-266.
- [25] M. Watanabe, S. Motoo, Electrocatalysis by ad-atoms: Part II. Enhancement of the oxidation of methanol on platinum by ruthenium ad-atoms, *Journal of Electroanalytical Chemistry and Interfacial Electrochemistry*. 60 (1975) 267-273.
- [26] M. Krausa, W. Vielstich, Study of the electrocatalytic influence of Pt/Ru and Ru on the oxidation of residues of small organic molecules, *Journal of Electroanalytical Chemistry*. 379 (1994) 307-314.
- [27] J.R. Kitchin, J.K. Nørskov, M.A. Barteau, J.G. Chen, Role of Strain and Ligand Effects in the Modification of the Electronic and Chemical Properties of Bimetallic Surfaces, *Phys. Rev. Lett.* 93 (2004) 156801.
- [28] N.M. Markovic, H.A. Gasteiger, P.N. Ross, X. Jiang, I. Villegas, M.J. Weaver, Electro-oxidation mechanisms of methanol and formic acid on Pt-Ru alloy surfaces, *Electrochimica Acta*. 40 (1995) 91-98.
- [29] P.K. Babu, H.S. Kim, E. Oldfield, A. Wieckowski, Electronic Alterations Caused by Ruthenium in Pt–Ru Alloy Nanoparticles as Revealed by Electrochemical NMR, *The Journal of Physical Chemistry B*. 107 (2003) 7595-7600.
- [30] D. Astruc, *Organometallic chemistry and catalysis*, Springer, 2007.
- [31] F. Illas, S. Zurita, J. Rubio, A.M. Márquez, Origin of the vibrational shift of CO chemisorbed on Pt(111), *Phys. Rev. B*. 52 (1995) 12372-12379.
- [32] R.C. Binning Jr., M. Liao, C.R. Cabrera, Y. Ishikawa, H. Iddir, R. Liu, et al., Density functional calculations on CO attached to PtnRu(10–n) (n = 6–10) clusters, *International Journal of Quantum Chemistry*. 77 (2000) 589-598.
- [33] B. Beden, F. Kadirgan, C. Lamy, J.M. Leger, Electrocatalytic oxidation of methanol on platinum-based binary electrodes, *Journal of Electroanalytical Chemistry and Interfacial Electrochemistry*. 127 (1981) 75-85.
- [34] A. Kabbabi, R. Faure, R. Durand, B. Beden, F. Hahn, J.-M. Leger, et al., In situ FTIRS study of the electrocatalytic oxidation of carbon monoxide and methanol at platinum–ruthenium bulk alloy electrodes, *Journal of Electroanalytical Chemistry*. 444 (1998) 41-53.

-
- [35] T. Yajima, H. Uchida, M. Watanabe, In-Situ ATR-FTIR Spectroscopic Study of Electro-oxidation of Methanol and Adsorbed CO at Pt–Ru Alloy, *The Journal of Physical Chemistry B*. 108 (2004) 2654-2659.
- [36] J. Munk, P.A. Christensen, A. Hamnett, E. Skou, The electrochemical oxidation of methanol on platinum and platinum + ruthenium particulate electrodes studied by in-situ FTIR spectroscopy and electrochemical mass spectrometry, *Journal of Electroanalytical Chemistry*. 401 (1996) 215-222.
- [37] M.A. Rigsby, W.-P. Zhou, A. Lewera, H.T. Duong, P.S. Bagus, W. Jaegermann, et al., Experiment and Theory of Fuel Cell Catalysis: Methanol and Formic Acid Decomposition on Nanoparticle Pt/Ru, *The Journal of Physical Chemistry C*. 112 (2008) 15595-15601.
- [38] J. McBreen, S. Mukerjee, In Situ X-Ray Absorption Studies of a Pt-Ru Electrocatalyst, *J. Electrochem. Soc.* 142 (1995) 3399-3404.
- [39] Y. Tong, H.S. Kim, P.K. Babu, P. Waszczuk, A. Wieckowski, E. Oldfield, An NMR Investigation of CO Tolerance in a Pt/Ru Fuel Cell Catalyst, *J. Am. Chem. Soc.* 124 (2001) 468-473.
- [40] Tong, H.S. Kim, P.K. Babu, P. Waszczuk, A. Wieckowski, E. Oldfield, An NMR Investigation of CO Tolerance in a Pt/Ru Fuel Cell Catalyst, *Journal of the American Chemical Society*. 124 (2002) 468-473.
- [41] F.J. Scott, C. Roth, D.E. Ramaker, Kinetics of CO Poisoning in Simulated Reformate and Effect of Ru Island Morphology on PtRu Fuel Cell Catalysts As Determined by Operando X-ray Absorption Near Edge Spectroscopy, *The Journal of Physical Chemistry C*. 111 (2007) 11403-11413.
- [42] D.R. Rolison, P.L. Hagans, K.E. Swider, J.W. Long, Role of Hydrous Ruthenium Oxide in Pt–Ru Direct Methanol Fuel Cell Anode Electrocatalysts: The Importance of Mixed Electron/Proton Conductivity, *Langmuir*. 15 (1999) 774-779.
- [43] J.W. Long, R.M. Stroud, K.E. Swider-Lyons, D.R. Rolison, How To Make Electrocatalysts More Active for Direct Methanol Oxidation Avoid PtRu Bimetallic Alloys!, *The Journal of Physical Chemistry B*. 104 (2000) 9772-9776.
- [44] J. Wu, X.Z. Yuan, J.J. Martin, H. Wang, J. Zhang, J. Shen, et al., A review of PEM fuel cell durability: Degradation mechanisms and mitigation strategies, *Journal of Power Sources*. 184 (2008) 104-119.
- [45] S. Zhang, X.-Z. Yuan, J.N.C. Hin, H. Wang, K.A. Friedrich, M. Schulze, A review of platinum-based catalyst layer degradation in proton exchange membrane fuel cells, *Journal of Power Sources*. 194 (2009) 588-600.

-
- [46] F. Ettingshausen, J. Kleemann, M. Michel, M. Quintus, H. Fuess, C. Roth, Spatially resolved degradation effects in membrane-electrode-assemblies of vehicle aged polymer electrolyte membrane fuel cell stacks, *Journal of Power Sources*. 194 (2009) 899-907.
- [47] F.A. de Bruijn, V.A.T. Dam, G.J.M. Janssen, Review: Durability and Degradation Issues of PEM Fuel Cell Components, *Fuel Cells*. 8 (2008) 3-22.
- [48] R. Borup, J. Meyers, B. Pivovar, Y.S. Kim, R. Mukundan, N. Garland, et al., Scientific Aspects of Polymer Electrolyte Fuel Cell Durability and Degradation, *Chemical Reviews*. 107 (2007) 3904-3951.
- [49] N. Wongyao, A. Therdthianwong, S. Therdthianwong, The fading behavior of direct methanol fuel cells under a start-run-stop operation, *Fuel*. 89 (2010) 971-977.
- [50] D.A. Stevens, M.T. Hicks, G.M. Haugen, J.R. Dahn, Ex Situ and In Situ Stability Studies of PEMFC Catalysts, *J. Electrochem. Soc.* 152 (2005) A2309-A2315.
- [51] S. Uhm, J. Lee, Accelerated durability test of DMFC electrodes by electrochemical potential cycling, *Journal of Industrial and Engineering Chemistry*. 15 (2009) 661-664.
- [52] J. Kang, D.W. Jung, S. Park, J.-H. Lee, J. Ko, J. Kim, Accelerated test analysis of reversal potential caused by fuel starvation during PEMFCs operation, *International Journal of Hydrogen Energy*. 35 (2010) 3727-3735.
- [53] J.-Y. Park, S.-J. Song, J.-H. Lee, J.-H. Kim, H. Cho, The possible failure mode and effect analysis of membrane electrode assemblies and their potential solutions in direct methanol fuel cell systems for portable applications, *International Journal of Hydrogen Energy*. 35 (2010) 7982-7990.
- [54] J.W. Schultze, A. J. Bard (Ed.): *Encyclopedia of Electrochemistry of the Elements*, Vol. 4, Marcel Decker Inc., New York and Basel 1975, 465 Seiten, Preis: 300,- DM., *Berichte Der Bunsengesellschaft Für Physikalische Chemie*. 80 (1976) 1249-1249.
- [55] P. Piela, C. Eickes, E. Brosha, F. Garzon, P. Zelenay, Ruthenium Crossover in Direct Methanol Fuel Cell with Pt-Ru Black Anode, *J. Electrochem. Soc.* 151 (2004) A2053.
- [56] C.-M. Lai, J.-C. Lin, K.-L. Hsueh, C.-P. Hwang, K.-C. Tsay, L.-D. Tsai, et al., On the Accelerating Degradation of DMFC at Highly Anodic Potential, *J. Electrochem. Soc.* 155 (2008) B843.
- [57] L. Gancs, B.N. Hult, N. Hakim, S. Mukerjee, The Impact of Ru Contamination of a Pt/C Electrocatalyst on Its Oxygen-Reducing Activity, *Electrochem. Solid-State Lett.* 10 (2007) B150-B154.
- [58] T.M. Arruda, B. Shyam, J.S. Lawton, N. Ramaswamy, D.E. Budil, D.E. Ramaker, et al., Fundamental Aspects of Spontaneous Cathodic Deposition of Ru onto Pt/C Electrocatalysts and Membranes under Direct Methanol Fuel Cell Operating Conditions:

-
- An in Situ X-ray Absorption Spectroscopy and Electron Spin Resonance Study, *The Journal of Physical Chemistry C*. 114 (2010) 1028-1040.
- [59] F. Hasché, M. Oezaslan, P. Strasser, Activity, stability and degradation of multi walled carbon nanotube (MWCNT) supported Pt fuel cell electrocatalysts, *Phys. Chem. Chem. Phys.* 12 (2010) 15251.
- [60] M.-xian Wang, F. Xu, H.-fang Sun, Q. Liu, K. Artyushkova, E.A. Stach, et al., Nanoscale graphite-supported Pt catalysts for oxygen reduction reactions in fuel cells, *Electrochimica Acta*. 56 (2011) 2566-2573.
- [61] D. Wang, C.V. Subban, H. Wang, E. Rus, F.J. DiSalvo, H.D. Abruña, Highly Stable and CO-Tolerant Pt/Ti_{0.7}W_{0.3}O₂ Electrocatalyst for Proton-Exchange Membrane Fuel Cells, *Journal of the American Chemical Society*. 132 (2010) 10218-10220.
- [62] T.B. Do, M. Cai, M.S. Ruthkosky, T.E. Moylan, Niobium-doped titanium oxide for fuel cell application, *Electrochimica Acta*. 55 (2010) 8013-8017.
- [63] H. Liang, X. Cao, F. Zhou, C. Cui, W. Zhang, S. Yu, A Free-Standing Pt-Nanowire Membrane as a Highly Stable Electrocatalyst for the Oxygen Reduction Reaction, *Advanced Materials*. 23 (2011) 1467-1471.
- [64] C. Susut, T.D. Nguyen, G.B. Chapman, Y. Tong, Shape and size stability of Pt nanoparticles for MeOH electro-oxidation, *Electrochimica Acta*. 53 (2008) 6135-6142.
- [65] Y. Dai, L. Ou, W. Liang, F. Yang, Y. Liu, S. Chen, Efficient and Superiorly Durable Pt-Lean Electrocatalysts of Pt–W Alloys for the Oxygen Reduction Reaction, *The Journal of Physical Chemistry C*. 115 (2011) 2162-2168.
- [66] Z.X. Liang, T.S. Zhao, J.B. Xu, Stabilization of the platinum–ruthenium electrocatalyst against the dissolution of ruthenium with the incorporation of gold, *Journal of Power Sources*. 185 (2008) 166-170.
- [67] C. Wang, H. Daimon, Y. Lee, J. Kim, S. Sun, Synthesis of Monodisperse Pt Nanocubes and Their Enhanced Catalysis for Oxygen Reduction, *Journal of the American Chemical Society*. 129 (2007) 6974-6975.
- [68] T. Tamaki, A. Yamauchi, T. Ito, H. Ohashi, T. Yamaguchi, The Effect of Methanol Crossover on the Cathode Overpotential of DMFCs, *Fuel Cells*. 11 (2011) 394-403.
- [69] C.Y. Chen, P. Yang, Y.S. Lee, K.F. Lin, Fabrication of electrocatalyst layers for direct methanol fuel cells, *Journal of Power Sources*. 141 (2005) 24-29.
- [70] T.V. Reshetenko, H.-T. Kim, H. Lee, M. Jang, H.-J. Kweon, Performance of a direct methanol fuel cell (DMFC) at low temperature: Cathode optimization, *Journal of Power Sources*. 160 (2006) 925-932.

-
- [71] G.-B. Jung, A. Su, C.-H. Tu, F.-B. Weng, Effect of Operating Parameters on the DMFC Performance, *J. Fuel Cell Sci. Technol.* 2 (2005) 81-85.
- [72] K. Bouzek, S. Moravcova, Z. Samec, J. Schauer, H⁺ and Na⁺ Ion Transport Properties of Sulfonated Poly(2,6-dimethyl-1,4-phenyleneoxide) Membranes, *J. Electrochem. Soc.* 150 (2003) E329-E336.
- [73] B. Kosmala, J. Schauer, Ion-exchange membranes prepared by blending sulfonated poly(2,6-dimethyl-1,4-phenylene oxide) with polybenzimidazole, *Journal of Applied Polymer Science.* 85 (2002) 1118-1127.
- [74] Y.-C. Chen, W.-L. Chen, M.-Y. Lo, Y.-Z. Chen, E.-K. Feng, Y.W. Chen, et al., Key Issues to the Preparation of Methanol-tolerant Cathode Catalyst for DMFC, in: *ECS Transactions*, Vienna, Austria, 2009: pp. 789-797.
- [75] D.C. Papageorgopoulos, F. Liu, O. Conrad, A study of Rh_xSy/C and RuSex/C as methanol-tolerant oxygen reduction catalysts for mixed-reactant fuel cell applications, *Electrochimica Acta.* 52 (2007) 4982-4986.
- [76] J.-W. Lee, B.N. Popov, Ruthenium-based electrocatalysts for oxygen reduction reaction—a review, *J Solid State Electrochem.* 11 (2007) 1355-1364.
- [77] G. Zehl, P. Bogdanoff, I. Dorbandt, S. Fiechter, K. Wippermann, C. Hartnig, Carbon supported Ru–Se as methanol tolerant catalysts for DMFC cathodes. Part I: preparation and characterization of catalysts, *J Appl Electrochem.* 37 (2007) 1475-1484.
- [78] A. Schröder, K. Wippermann, J. Mergel, W. Lehnert, D. Stolten, T. Sanders, et al., Combined local current distribution measurements and high resolution neutron radiography of operating Direct Methanol Fuel Cells, *Electrochemistry Communications.* 11 (2009) 1606-1609.
- [79] A.A. Kulikovskiy, H. Schmitz, K. Wippermann, J. Mergel, B. Fricke, T. Sanders, et al., Bifunctional activation of a direct methanol fuel cell, *Journal of Power Sources.* 173 (2007) 420-423.
- [80] D. Kim, J. Lee, T.-H. Lim, I.-H. Oh, H.Y. Ha, Operational characteristics of a 50 W DMFC stack, *Journal of Power Sources.* 155 (2006) 203-212.
- [81] G.Q. Lu, P.C. Lim, F.Q. Liu, C.Y. Wang, On mass transport in an air-breathing DMFC stack, *International Journal of Energy Research.* 29 (2005) 1041-1050.
- [82] S. Lee, D. Kim, J. Lee, S.T. Chung, H.Y. Ha, Comparative studies of a single cell and a stack of direct methanol fuel cells, *Korean J. Chem. Eng.* 22 (2005) 406-411.
- [83] S. Zils, M. Timpel, T. Arlt, A. Wolz, I. Manke, C. Roth, 3D Visualisation of PEMFC Electrode Structures Using FIB Nanotomography, *Fuel Cells.* 10 (2010) 966-972.

-
- [84] D. Seo, J. Lee, S. Park, J. Rhee, S.W. Choi, Y.-G. Shul, Investigation of MEA degradation in PEM fuel cell by on/off cyclic operation under different humid conditions, *International Journal of Hydrogen Energy*. 36 (2011) 1828-1836.
- [85] I. Manke, C. Hartnig, M. Grünerbel, W. Lehnert, N. Kardjilov, A. Haibel, et al., Investigation of water evolution and transport in fuel cells with high resolution synchrotron x-ray radiography, *Appl. Phys. Lett.* 90 (2007) 174105.
- [86] S. Morita, Y. Jojima, Y. Miyata, K. Kitagawa, Near-Infrared Imaging of Water in a Polymer Electrolyte Membrane during a Fuel Cell Operation, *Analytical Chemistry*. 82 (2010) 9221-9224.
- [87] S. Tsushima, K. Teranishi, S. Hirai, Water diffusion measurement in fuel-cell SPE membrane by NMR, *Energy*. 30 (February) 235-245.
- [88] V. Parry, G. Berthomé, J.-C. Joud, O. Lemaire, A.A. Franco, XPS investigations of the proton exchange membrane fuel cell active layers aging: Characterization of the mitigating role of an anodic CO contamination on cathode degradation, *Journal of Power Sources*. 196 (2011) 2530-2538.
- [89] M. Newville, IFEFFIT: interactive XAFS analysis and FEFF fitting, *Journal of Synchrotron Radiation*. 8 (2001) 322-324.
- [90] K. Asakura, T. Kubota, W.J. Chun, Y. Iwasawa, K. Ohtani, T. Fujikawa, Pt L3-edge XANES studies about the hydrogen adsorption on small Pt particles, *Journal of Synchrotron Radiation*. 6 (1999) 439-441.
- [91] G. Bunker, *Introduction to XAFS: A Practical Guide to X-ray Absorption Fine Structure Spectroscopy*, Cambridge University Press, 2010.
- [92] J. McBreen, S. Mukerjee, In Situ X-Ray Absorption Studies of a Pt-Ru Electrocatalyst, *J. Electrochem. Soc.* 142 (1995) 3399-3404.
- [93] B.J. Hwang, C.-H. Chen, L.S. Sarma, J.-M. Chen, G.-R. Wang, M.-T. Tang, et al., Probing the Formation Mechanism and Chemical States of Carbon-Supported Pt-Ru Nanoparticles by in Situ X-ray Absorption Spectroscopy, *The Journal of Physical Chemistry B*. 110 (2006) 6475-6482.
- [94] M.E. Herron, S.E. Doyle, S. Pizzini, K.J. Roberts, J. Robinson, G. Hards, et al., In situ studies of a dispersed platinum on carbon electrode using X-ray absorption spectroscopy, *Journal of Electroanalytical Chemistry*. 324 (1992) 243-258.
- [95] C. Roth, N. Benker, T. Buhrmester, M. Mazurek, M. Loster, H. Fuess, et al., Determination of O[H] and CO Coverage and Adsorption Sites on PtRu Electrodes in an Operating PEM Fuel Cell, *Journal of the American Chemical Society*. 127 (2005) 14607-14615.

-
- [96] A.E. Russell, S. Maniguet, R.J. Mathew, J. Yao, M.A. Roberts, D. Thompsett, In situ X-ray absorption spectroscopy and X-ray diffraction of fuel cell electrocatalysts, *Journal of Power Sources*. 96 (2001) 226-232.
- [97] E. Principi, A. Witkowska, S. Dsoke, R. Marassi, A. Di Cicco, An XAS experimental approach to study low Pt content electrocatalysts operating in PEM fuel cells, *Physical Chemistry Chemical Physics*. 11 (2009) 9987.
- [98] S.L. Burton, Time Resolved Characterisation of Fuel Cell Cathode Catalysts Using Operando XAS, *ECS Meeting Abstracts*. 902 (2009) 861.
- [99] J. Melke, A. Schoekel, D. Dixon, C. Cremers, D.E. Ramaker, C. Roth, Ethanol Oxidation on Carbon-Supported Pt, PtRu, and PtSn Catalysts Studied by Operando X-ray Absorption Spectroscopy, *The Journal of Physical Chemistry C*. 114 (2010) 5914-5925.
- [100] R.J.K. Wiltshire, C.R. King, A. Rose, P.P. Wells, M.P. Hogarth, D. Thompsett, et al., A PEM fuel cell for in situ XAS studies, *Electrochimica Acta*. 50 (2005) 5208-5217.
- [101] E. Principi, A. Di Cicco, A. Witkowska, R. Marassi, Performance of a fuel cell optimized for in situ X-ray absorption experiments, *Journal of Synchrotron Radiation*. 14 (2007) 276-281.
- [102] A.S. Arico, P. Creti, H. Kim, R. Mantegna, N. Giordano, V. Antonucci, Analysis of the Electrochemical Characteristics of a Direct Methanol Fuel Cell Based on a Pt-Ru/C Anode Catalyst, *J. Electrochem. Soc.* 143 (1996) 3950-3959.
- [103] H. Nitani, T. Nakagawa, H. Daimon, Y. Kurobe, T. Ono, Y. Honda, et al., Methanol oxidation catalysis and substructure of PtRu bimetallic nanoparticles, *Applied Catalysis A: General*. 326 (2007) 194-201.
- [104] S.Q. Song, Z.X. Liang, W.J. Zhou, G.Q. Sun, Q. Xin, V. Stergiopoulos, et al., Direct methanol fuel cells: The effect of electrode fabrication procedure on MEAs structural properties and cell performance, *Journal of Power Sources*. 145 (2005) 495-501.
- [105] A.I. Frenkel, C.W. Hills, R.G. Nuzzo, A View from the Inside: Complexity in the Atomic Scale Ordering of Supported Metal Nanoparticles, *The Journal of Physical Chemistry B*. 105 (2001) 12689-12703.
- [106] A.E. Russell, A. Rose, X-ray Absorption Spectroscopy of Low Temperature Fuel Cell Catalysts, *Chemical Reviews*. 104 (2004) 4613-4636.
- [107] A. Rose, E.M. Crabb, Y. Qian, M.K. Ravikumar, P.P. Wells, R.J.K. Wiltshire, et al., Potential dependence of segregation and surface alloy formation of a Ru modified carbon supported Pt catalyst, *Electrochimica Acta*. 52 (2007) 5556-5564.

-
- [108] D. Liang, Q. Shen, M. Hou, Z. Shao, B. Yi, Study of the cell reversal process of large area proton exchange membrane fuel cells under fuel starvation, *Journal of Power Sources*. 194 (2009) 847-853.
- [109] J.X. Wang, J. Zhang, R.R. Adzic, Double-Trap Kinetic Equation for the Oxygen Reduction Reaction on Pt(111) in Acidic Media†, *The Journal of Physical Chemistry A*. 111 (2007) 12702-12710.
- [110] D.S. Gatewood, T.L. Schull, O. Baturina, J.J. Pietron, Y. Garsany, K.E. Swider-Lyons, et al., Characterization of Ligand Effects on Water Activation in Triarylphosphine-Stabilized Pt Nanoparticle Catalysts by X-ray Absorption Spectroscopy, *The Journal of Physical Chemistry C*. 112 (2008) 4961-4970.
- [111] H. Dohle, J. Mergel, P.C. Ghosh, DMFC at low air flow operation: Study of parasitic hydrogen generation, *Electrochimica Acta*. 52 (2007) 6060-6067.
- [112] Z. Lin, H. Chu, Y. Shen, L. Wei, H. Liu, Y. Li, Rational preparation of faceted platinum nanocrystals supported on carbon nanotubes with remarkably enhanced catalytic performance, *Chem. Commun.* (2009) 7167.
- [113] M.S. Wilson, S. Gottesfeld, High Performance Catalyzed Membranes of Ultra-low Pt Loadings for Polymer Electrolyte Fuel Cells, *J. Electrochem. Soc.* 139 (1992) L28-L30.
- [114] K.M. Bratlie, H. Lee, K. Komvopoulos, P. Yang, G.A. Somorjai, Platinum Nanoparticle Shape Effects on Benzene Hydrogenation Selectivity, *Nano Letters*. 7 (2007) 3097-3101.
- [115] T.S. Ahmadi, Z.L. Wang, T.C. Green, A. Henglein, M.A. El-Sayed, Shape-Controlled Synthesis of Colloidal Platinum Nanoparticles, *Science*. 272 (1996) 1924 -1925.



List of Figures

Figure 1: Schematic representation of DMFC, the MEA region is enlarged below	4
Figure 2: Summary of different steps in MOR	7
Figure 3: Schematic representation of bonding of CO with Pt	8
Figure 4: Polarization curve for H ₂ -PEMFC and a DMFC (it is to be noted that Pt loading of the DMFC is twice that of H ₂ -PEMFC)	11
Figure 5: Schematic representation of catalyst and support degradation in fuel cells.	13
Figure 6: TEM micrograph of commercial carbon supported Pt catalyst	16
Figure 7: Scheme showing the splitting of DMFC into galvanic region and electrolytic region during bi-functional operation	19
Figure 8: XAS spectrum at Pt L ₃ edge describing various interactions of the photoelectron	25
Figure 9: Schematic representation of data processing procedure for XANES analysis	27
Figure 10: Various Pt, Pt/Ru clusters used for getting theoretical $\Delta\mu$ signature. The graph showing the theoretical $\Delta\mu$ signature of Atop adsorbed CO, and O on Pt/Ru cluster (calculated by FEFF 8)	28
Figure 11: Schematic representation of data processing procedure for EXAFS analysis	30
Figure 12: Schematic representation of in-situ cells, a) Kapton window cell, b) detailed sketch of the cell a, c) thinned down graphite cell, d) detailed sketch of cell c without X-ray window.	35
Figure 13: Polarization curves for differently fabricated fuel cells	36
Figure 14: XAS spectra Ru K edge QEXAFS and slow step EXAFS	37
Figure 15: In-situ DMFC XAS spectra at Pt L ₃ measured simultaneously in both transmission and fluorescent geometries	37
Figure 16: FT Pt L ₃ edge of samples measured in various geometries	38

Figure 17: Pt L ₃ edge XAS spectra for the two different cells	39
Figure 18: Sketch showing relevant investigated regions in an MEA	42
Figure 19: XRD patterns of the anode catalyst: as-received catalyst, pristine MEA, methanol inlet, anode middle, methanol outlet, No Ru reflection observed for different samples	44
Figure 20: XRD patterns of the cathode catalyst: as-received catalyst, pristine MEA, oxygen inlet, cathode middle, oxygen outlet. Particle size is doubled by the MEA fabrication process, but no differences depending on cathode area were observed after operation.	45
Figure 21: FT Ru K edge taken for the as-received Pt/Ru catalyst, pristine MEA, the catalyst after operation and a hydrous ruthenium oxide standard. Before operation, ruthenium appears to be largely oxidized.	48
Figure 22: FT Pt L ₃ edge taken for the as-received Pt/Ru catalyst, pristine MEA and the catalyst after operation	48
Figure 23: FT Ru K edge spectrum of the pristine MEA compared to the MEA during open circuit voltage (OCV) condition. At OCV, a significant fraction of the Ru oxides gets reduced.	49
Figure 24: Schematic representation of structural changes in DMFC conditions	50
Figure 25: FT Pt L ₃ edge of the anode side taken for the methanol inlet, middle and outlet regions.	51
Figure 26: FT Ru K edge of the anode side taken for methanol inlet, middle and outlet regions. While the Pt edge does not show pronounced differences, at the Ru edge the catalyst at the methanol outlet is affected.	51
Figure 27: FT Pt L ₃ edge of the cathode side- pristine MEA and as-received catalyst	52
Figure 28: FT Pt L ₃ edge of the cathode samples from different regions, i.e. oxygen inlet, middle and outlet. In good agreement with the XRD data, no site-dependent changes were observed.	53
Figure 29: Ru K edge XANES spectra of the cathode catalyst. Near edge characteristics similar to a RuO ₂ standard were found all over the cathode side of the MEA.	53
Figure 30: Particle size distribution from thin cut TEM analysis: (a) pristine MEA anode side, (b) pristine MEA cathode side, (c) aged MEA anode side, (d) aged MEA cathode side.	54

Figure 31: TEM thin cuts investigation of anode catalyst, a) & b) Pristine MEA low and high magnification, c) & d) aged anode low and high magnification. Chain like structure seen after ageing (c)	55
Figure 32: TEM thin cuts investigation of cathode catalyst, a) & b) Pristine MEA low and high magnification, c) & d) aged cathode low and high magnification.	56
Figure 34: SEM image of anode of the pristine MEA (left), and EDX mapping of the corresponding area	57
Figure 33: TEM images showing the amorphous precipitate in the Nafion membrane at the methanol outlet region.	57
Figure 35: SEM image of cathode of the pristine MEA (left), and EDX mapping of the corresponding area	58
Figure 36: SEM image of anode of the methanol outlet (left), and EDX mapping of the corresponding area	59
Figure 37: EDX spectra obtained for cathode of the fresh MEA and aged MEA	59
Figure 38: SEM image of cathode of the methanol inlet (left), and EDX mapping of the corresponding area	60
Figure 39: Spatially resolved <i>in-situ</i> DMFC XAS set up at beamline X1 HASYLAB	62
Figure 40: Estimated cathodic and anodic potential for a DMFC at high and low oxygen flow	64
Figure 41: $\Delta\mu$ signature obtained for the methanol inlet region (bottom). Theoretical (red and blue) and experimental $\Delta\mu$ signature from the literature (top)	65
Figure 42: $\Delta\mu$ signatures: different regions of anode and cathode under different cell voltages (not smoothed)	67
Figure 43: $\Delta\mu$ magnitude for both anode (left) and cathode (right) from different regions plotted against the cell voltage (the estimated cell potential indicated at the top).	68
Figure 44: $\Delta\mu$ signatures: different regions of anode and cathode under different cell voltages at low oxygen flow	71
Figure 45: $\Delta\mu$ magnitude obtained for different regions of anode (left) and cathode (right) under low oxygen flow.	72
Figure 46: Estimated anode and cathode potential under low oxygen flow	73

Figure 47: Polarization obtained during the fuel starvation studies	75
Figure 48: Ru K edge XANES spectra during fuel starvation studies	76
Figure 49: Pt L ₃ edge XANES spectra from the different regions of the fuel cell after fuel starvation	77
Figure 50: Ru K edge XANES spectra from different regions after fuel starvation	78
Figure 51: TEM images of shape-selected particles, a) & b) showing predominantly cubic particles (high pH), c) & d) showing particles with cuboctahedral shape, e) & f) showing porous particles (low H ₂ gas).	83
Figure 52: Particle size distribution from TEM	84
Figure 53: Cyclic-voltammogram, (top) shape-selected particle, (bottom) Pt/Vulcan	85
Figure 54: Cyclic-voltammogram of shape-selected particles at different cycles	86
Figure 55: TEM micrograph of the shape-selected particles after electrochemical cycling	87
Figure 56: TEM micrograph of Pt particles synthesized in the presence of TTAB and Vulcan carbon	88
Figure 57: TEM micrograph of Pt particles synthesized a), and b) in the presence of TTAB and CNT, c) and d) in the presence of PVP and CNT	89
Figure 58: TEM micrograph of the impregnated shape selected catalyst; high and low magnification image	90
Figure 59: TG curve obtained for the shape selected catalyst	91
Figure 60: (Top) polarization curve obtained for different samples, (bottom) power density curve	92
Figure 61: Polarization curves obtained for the shape selected catalyst when used as cathode (red) and anode (black). (Same MEA was used for both experiment, gas connections and electrical connections were inverted)	93

List of Tables

Table 1: Fuel cell components and functions	5
Table 2: Cause and effect of degradation of various components in a fuel cell	14
Table 3: In-homogeneities in direct methanol fuel cells	20
Table 4: Different analytical techniques for spatially resolved fuel cell studies	21
Table 5: Average particle sizes determined from XRD analysis using Scherrer's equation	46
Table 6: EXAFS analysis anode catalyst Ru K edge	47
Table 7: EXAFS analysis anode catalyst Pt L ₃ edge	47
Table 8: Pt L ₃ edge EXAFS analysis of cathode catalyst	52
Table 9: Pt L ₃ edge analysis of fuel starved anode samples	77
Table 10: EXAFS analysis Ru K edge, samples from different regions after fuel starvation and for comparison, EXAFS analysis of a sample during the starvation process is also shown.	79

Acknowledgement

This work was carried out at the Institute for Materials Science, Technische Universität Darmstadt. The financial support by the “Bundesministerium für Bildung und Forschung” (BMBF, RuNPEM,03SF0324E) is gratefully acknowledged.

I would like to thank my supervisor and referee Prof. Dr. Christina Roth for her enthusiastic guidance. Moreover, she was very generous in sending me for various relevant conferences and workshop which helped me a lot with my work.

I am grateful to Prof. Dr. Ralf Riedel for being my referee and also to Prof. Dr. Wolfgang Ensinger and Prof. Dr. Peter Claus for being my internal and external examiners.

I would like to thank Prof. Dr. David Ramaker from George Washington University for helping me with $\Delta\mu$ analysis and hosting me in his home for a research work.

I wish to thank Dr. Klaus Wippermann and Jürgen Mergel from Forschungszentrum Jülich GmbH for fruitful discussions and providing me with DMFC samples and cells.

I also like to thank Prof. Gregor Hoogers and Mr Volker Loose from Umwelt-Campus, Birkenfeld for helping me to design *in-situ* fuel cells.

I would also like to thank the beamline scientists, Dr. Adam Webb, Dr. Edmund Welter (Hasylab), Dr. Stefan Mangold (Anka) Dr. Olivier Mathon, Dr. Matthieu Chorro (ESRF) for their kind support during the beamtime.

Technical assistance from Ms. Ulrike Kunz (thin cut sample preparation and SEM-EDX mapping), Mr. Heinz Mohren (fuel cell sketch), Mr Jean-Christoph Jaud (XRD measurements), and Ms. Claudia Fasel (TG) are greatly acknowledged.

I would like to thank Ms. Susane Zils for helping me to handle CM20 TEM microscope.

I would like to thank Mr. Alexander Schökel, Mr. Sebastian Kaserer, Mr. Benedikt Peter, Dr. Julia Melke for their useful discussions and helping me with the beamtime. I like to thank Dr. Matthias Söhn for providing technical support for the fuel cell test bench. I express my sincere gratitude to all the present and former group members of the Renewable Energies group for creating a friendly atmosphere.

I would like to acknowledge Mr. Jitendra Rathore and Ms. Miriam Botros for carrying out experiments on shape selected particles. Ms. Anja Haberer (TUD) and Ms. Maryam Farmand (GWU) are greatly acknowledged for preliminary spatially resolved analysis.

All colleagues in working group Structural Research are gratefully acknowledged for their support and help during this work.

I wish to thank my fiancé Aiswarya and my brother Dawn for supporting and caring for me. I would also like to thank my friends Thomy, Lena, JB, Gisa, Joshni, Praseedha, Laetitia, Joachim, Ljuba, Sajan, Ani, Lincy, Angelina, Ilona, Niels, who have made my time in Germany as well as in India unforgettable. Special thanks to Werner, Karen, Gerhard and their family.

Finally I remember my parents Johnson Dickson and Metty Dickson whom I lost during my PhD times. I would also like to thank all my family members who helped me during the hard times.

Thanks to God almighty!

Curriculum Vitae

EDUCATION

- 03/2008 **Ph. D in Materials Science**, Technische Universität Darmstadt,
Germany
- 07/2004 – 07/2006 **M. Sc Chemistry**
Specialization in Inorganic Chemistry
School of Chemical Sciences, Mahatma Gandhi University, Kottayam,
Kerala, India
Masters thesis Indian Institute of Technology Madras, Chennai, India
- 2001 – 2004 **B. Sc Chemistry**
Specialization: Industrial Chemistry
Sacred Heart College, Thevara, affiliated to Mahatma Gandhi
University, Kottayam, Kerala, India
- 1999 – 2001 **Pre - Degree Course (12th level)**
St. Michael's College, Cherthala, affiliated to Kerala University,
Trivandrum, Kerala, India
- 1999 **10th level (ICSE- Council for the Indian School Certificate
Examination)**
Public School, Pattanakad, Cherthala, affiliated to Council for
Indian Secondary Education.

INDUSTRIAL EXPERIENCE

- 09/2006 – 03/2008 Research Associate, Unilever Research Center, Bangalore, Karnataka,
India

09/2003 – 10/2003

Industrial training

Investigation of extraction of rare earths and Thorium from Monazite sand. Indian Rare Earths Ltd., Cochin, Kerala, India

Publications and Patents

D. Dixon, M. A. Haberer, Farmand, S. Kaserer C. Roth, D. E. Ramaker, *Space-resolved, in Operando X-ray Absorption Spectroscopy: Investigations on both the Anode and Cathode in a DMFC*, J. Phys. Chem. C 116 (2012) 7587

D. Dixon, K. Wippermann, J. Mergel, A. Schoekel, S. Zils, C. Roth, “*Degradation effects at the methanol inlet, outlet and center region of a stack MEA operated in DMFC*”, Journal of Power Sources, 196 (2011) 5538.

D. Dixon, A. Schröder, A. Schökel, M. Söhn, I. Manke, N. Kardjilov, T. Sanders, V. Loos, G. Hoogers, K. Wippermann, D. Stolten, C. Roth, “*Design of in-situ experimentation for the study of fuel cells with X-rays and neutrons*”, MP Materials Testing 10 (2010) 725-735.

J. Melke, A. Schoekel, **D. Dixon**, C. Cremers, D. E. Ramaker, C. Roth, “*Ethanol oxidation on carbon-supported Pt, PtRu and PtSn catalysts studied by operando X-ray absorption spectroscopy*”, J. Phys. Chem. C 114 (2010) 5914-5925.

G. Sevjdasuren, S. Zils, S. Kaserer, A. Wolz, F. Ettingshausen, **D. Dixon**, A. Schoekel, C. Roth, P. Altantsog, D. Sangaa, C. Ganzorig, “*Effect of different support morphology and Pt particle sizes in electrocatalysts for fuel cell applications*”, Journal of Nanomaterials (2010) doi:10.1155/2010/852786.

S. K. Barne, **D. Dixon**, A. Perincheery, G. K. Velayudhan Nair, “*Process for treatment of a fabric*”, **WO/2009/077255**.

Conference contributions

“Spatially-resolved X-ray absorption spectroscopy studies in DMFC”, **D. Dixon**, A. Schökel, V. Loos, G. Hoogers, K. Wippermann C. Roth, (UECT 2010 Poster).

“Time and spatially resolved study of fuel cell reactions using *in-situ* X-ray absorption spectroscopy”,
D. Dixon, J. Melke, S. Kaserer, A. Schoekel, C. Cremers, D. Ramaker, and C. Roth, (ECS Montreal
2011 Oral talk)